UNIVERSITÉ DU QUÉBEC À MONTRÉAL

ÉTUDE DE L'EFFET D'INHIBITION DU GEL INDUIT PAR LES SULFATES DANS LES NUAGES ARCTIQUES À L'AIDE DES MESURES SATELLITAIRES DE CLOUDSAT ET CALIPSO

THÈSE
PRÉSENTÉE
COMME EXIGENCE PARTIELLE
DU DOCTORAT EN SCIENCES DE L'ENVIRONNEMENT

PAR
PATRICK GRENIER

MAI 2010

REMERCIEMENTS

Je tiens à remercier de prime abord mon directeur de thèse, Jean-Pierre Blanchet. Je me souviens encore de la passion pour la science dont il avait fait preuve lors de notre premier entretien, un jour de vacances du début de janvier 2004. Même si j'étais alors complètement ignorant en sciences de l'atmosphère, il avait tout de suite cru en ma capacité à réaliser un doctorat dans ce domaine. Sa passion pour la science ainsi que sa confiance en moi ne l'ont jamais quitté depuis, et ont grandement contribué à ce que je décide de poursuivre ma carrière post-doctorale de climatologue.

D'autres professeurs m'ont grandement aidé durant mon parcours, que ce soit en m'enseignant les bases des sciences de l'atmosphère et de l'environnement, en réglant des tracas administratifs ou en me conseillant dans mes recherches. Je remercie tous les professeurs concernés, et en particulier les membres de mon comité d'encadrement: Colin Jones, Éric Girard et Graeme Stephens.

Mes recherches n'auraient jamais mené au dépôt d'une thèse sans l'aide du personnel de soutien de l'Institut des Sciences de l'Environnement et du Département des Sciences de l'Environnement de l'UQAM. Je remercie encore une fois toutes les personnes concernées, et en particulier Nadjet Labassi, Eva Monteiro, Frédéric Toupin, Abderrahim Khaled, Delphine Person et Lucie Brodeur.

Malgré que le doctorat constitue un accomplissement essentiellement individuel, la présence et le soutien des autres étudiants joue un rôle déterminant sur le moral. J'ai donc une pensée pour toute la cohorte qui avait suivi avec moi les cours de la maîtrise en atmosphère, pour les étudiants du doctorat en environnement qui ont vécu les mêmes difficultés et savouré certains mêmes apprentissages que moi, ainsi que pour les étudiants du baccalauréat en maths-météo auxquels j'ai pu avoir le plaisir de relayer certaines de mes connaissances. Il est loin le jour où j'oublierai Phil, Mariane, Serge, et les autres. J'ai aussi particulièrement apprécié les nombreux conseils et avis de Rodrigo, ainsi que le soutien indéfectible de Louis-Philippe, qui a suivi toute la gamme des états d'âme qui m'ont animé durant ce doctorat.

Enfin, je remercie grandement le Consortium Ouranos et le Conseil de Recherches en Sciences Naturelles et Génie (CRSNG) du Canada, sans le financement desquels organismes mon doctorat se serait peut-être étiré quelques sessions de plus.

TABLE DES MATIÈRES

LISTE DES FIGURES

LISTE DES TABLEAUX

LISTE DES ABRÉVIATIONS, SIGLES ET ACRONYMES

Liste française:

CLAW	(hypothèse) Charlson-Lovelock-Andreae-Warren
HR	humidité relative
HR_i	humidité relative par rapport à la glace
HR_w	humidité relative par rapport à l'eau liquide
IGIS	inhibition du gel induit par les sulfates
NC	noyau de condensation
NG	noyau glaçogène
NSPM	nuage stratiforme en phase mixte
RDES	rétroaction déshydratation-effet de serre

Liste anglaise:

AGASP	Arctic Gas and Aerosol Sampling Program
agl	above ground level
AIRS	Atmospheric Infrared Sounder
AMAP	Arctic Monitoring and Assessment Programme
APE	available potential energy
ARC- / ANT-	Arctic / Antarctica (names for data sets or subsets)
asl	above sea level
ASTAR	Arctic Study of Aerosols, Clouds and Radiation
AWAC4	Arctic Winter Aerosol and Cloud Classification from CloudSat and CALIPSO
CALIOP	Cloud-Aerosol Lidar with Orthogonal Polarization
CCN	cloud condensation nuclei
CDNC	cloud droplet number concentration
CPR	Cloud-Profiling Radar
CWC	cloud water content
DGF	dehydration-greenhouse feedback
DJF	December-January-February
EBC	Eastern Russia-Beaufort Sea-Canadian Archipelago
ECMWF	European Centre for Medium-Range Weather Forecasts
EMEP	European Monitoring and Evaluation Programme
GEIA	Global Emissions Inventory Activity
GNK	Greenland-North Atlantic-Kara Sea
IFN	ice-forming nuclei
IR	infrared
IWC	ice water content
JGR	Journal of Geophysical Research
LCC	linear correlation coefficient (same as r_{Pea})
LITE	Lidar In-space Technology Experiment
MLS	Microwave Limb Sounder
MODIS	Moderate Resolution Imaging Spectroradiometer
MPL	mixed-phase layer (same as MPS)
MPS	mixed-phase stratiform (same as MPL)
NAO	North Atlantic Oscillation
NARCM	Northern Aerosol Regional Climate Model
NCEP / NCAR	National Centers for Environmental Prediction / National Center for Atmsopheric Research
Nd:YAG	neodymium-doped yttrium aluminium garnet (laser medium)
NILU	Norwegian Institute for Air Research (Norwegian acronym)

nss	non-sea salt
ONA	off-nadir angle
PSC	polar stratospheric cloud
RH	relative humidity
RH_i	relative humidity with respect to ice
RH_w	relative humidity with respect to liquid water
SHEBA	Surface Heat Budget of the Arctic Ocean
SIFI	sulphate-induced freezing inhibition
TIC	type of ice cloud (thin ice cloud in Chapter I)

LISTE DES SYMBOLES

Symboles mathématiques:

a	exposant de la fonction de puissance de la distribution probabiliste de L
a_0	paramètre de la fonction de δ_{min} (sans unités)
a_1	paramètre de la fonction de δ_{min} ($km^{-1} sr^{-1}$)
b_1	seuil utilisé dans la détection des NSPM ($km^{-1} sr^{-1}$)
b_2	seuil utilisé dans la détection des NSPM ($km^{-1} sr^{-1}$)
B	constante de calibration de F_r
C	nombre d'enregistrements par intervalle de L
C_{att}	correction à un signal de rétro-diffusion pour combler l'atténuation du faisceau lidar ($km^{-1} sr^{-1}$)
C_{Ray}	correction à un signal de rétro-diffusion pour enlever la contribution moléculaire ($km^{-1} sr^{-1}$)
F_r	facteur de réduction de concentration en NG
F_{2B}	fraction de TIC-2B dans une série de pixels de TIC-2A, TIC-2B et TIC-2D
L	extension horizontale d'une couche de NSPM (km)
L_{avg}	moyenne arithmétrique de L pour une population de couverts nuageux
L_{geo}	moyenne géométrique de L pour une population de couverts nuageux
L_0	extension latérale de référence
lat_{max} / lon_{max}	latitude / longitude maximale d'une aire géographique sélectionnée (degrés)
lat_{min} / lon_{min}	latitude / longitude minimale d'une aire géographique sélectionnée (degrés)
lat_{Zep} / lon_{Zep}	latitude / longitude de la station Zeppelin Mountain (degrés)
m	pente de la fonction triangulaire $g(\chi)$
n_{min}	nombre minimal de points moyennés pour considérer une valeur quotidienne de α dans une série temporelle
r_{ie}	rayon effectif moyen
r_{Pea}	coefficient de corrélation de Pearson
T	température (°C ou °K)
T_{homog}	température de gel homogène
w_β	poids de $f(\beta_{532})$ dans la fonction α
w_γ	poids de $g(\chi)$ dans la fonction α
α	indice d'aérosols, indice de sulfates ou proxy de $[SO_4]$ (sans unités)
α_{haze_min}	seuil minimal de α pour identification de brume arctique
β_{1064}	rétro-diffusion à 1064 nm ($km^{-1} sr^{-1}$)
β_{532}	rétro-diffusion à 532 nm ($km^{-1} sr^{-1}$)
$\beta_{532\ min}$	seuil minimal de β_{532} pour identification des TIC-1
β_{per}	composante perpendicalaire de la rétro-diffusion à 532 nm ($km^{-1} sr^{-1}$)
β_{ref}	valeur de β_{532} de référence dans la fonction $f(\beta_{532})$
β_{thres}	valeur de β_{532} à laquelle une valeur inférieure est ramenée
δ	ratio de dépolarisation
δ_{ice_min}	seuil minimal de ratio de dépolarisation pour dominance des cristaux dans une couche de NSPM
δ_{min}	seuil minimal de ratio de dépolarisation pour identification de TIC-1
$\Delta\beta_{top\ min}$	gradient minimal de rétro-diffusion au sommet d'une couche de NSPM
λ	longueur d'onde (nm)
σ	déviation standard (unités diverses)
χ	ratio de couleurs (ou ratio de longueurs d'onde)
χ_0	valeur centrale de la fonction triangulaire $g(\chi)$
χ_{min}	seuil minimal de ratio de couleurs (diverses applications)
$\chi_{molecular}$	ratio de couleurs des molécules gazeuses

Symboles chimiques:

CO	monoxyde de carbone
DMS	sulfure de diméthyle (véritable formule: $(CH_3)_2S$)
H_2S	sulfure d'hydrogène
H_2SO_4	acide sulfurique
$MgSO_4$	sulfate de magnésium

Na_2SO_4	sulfate de sodium
$(NH_4)_2SO_4$	sulfate d'ammonium
NH_4HSO_4	bisulfate d'ammonium
OH•	radical hydroxyle
S	soufre
SO_2	dioxyde de soufre
SO_4 / SO_4^{2-}	sulfate / ion sulfate

Symboles reliés à une quantité x:

n_x	nombre de pixels d'un type x de nuage
$[x]^{all}$	tous les points de la série sont considérés
$[x]^{sub}$	seul un sous-ensemble des points de la série est considéré
$[x]_{tot}$	toutes les contributions considérées
$[x]_{nss}$	contribution du sel de mer ignorée (*non-sea salt*)
$[SO_4\text{-}S]$	concentration en sulfates ignorant la masse des atomes d'oxygène
$\overline{x}$	moyenne arithmétique de la distribution de x
[x]	concentration en la substance x ($\mu g / m^3$)

RÉSUMÉ

Les sulfates issus de la pollution industrielle d'Eurasie et transportés à travers la basse troposphère arctique durant l'hiver sont soupçonnés d'altérer les propriétés des nuages au point d'affecter significativement le climat de cette région. Un de leurs effets potentiellement importants est l'inhibition du gel des gouttelettes en cristaux de glace (effet IGIS), qui favoriserait les nuages formés de cristaux à grande taille et déclencherait un mécanisme associé à une anomalie de refroidissement à la surface. Grâce à de récentes données satellitaires, issues des missions CloudSat et CALIPSO, les implications escomptées de l'effet IGIS peuvent être testées à l'échelle de l'Arctique. La superposition des observations quasi-simultanées du radar de CloudSat et du lidar de CALIPSO a permis de développer une nouvelle classification des nuages arctiques centrée sur le rayon effectif des cristaux de glace. Un proxy de la concentration en sulfates dans les parcelles d'air non-nuageuses a aussi été élaboré à partir des mesures du lidar, et validé à partir de mesures in situ. Différents tests de corrélation entre d'une part les propriétés des nuages glacés censés êtres les plus affectés par l'effet IGIS (nommés TIC-2B) et d'autre part le proxy de la concentration en sulfates ont été conduits afin d'approfondir notre compréhension de cet effet. Des limites méthodologiques, entre autres l'impossibilité d'estimer les concentrations en sulfates à l'intérieur des nuages, ont empêché l'atteinte de conclusions définitives. Cependant, les distributions géographiques des TIC-2B et du proxy sont cohérentes avec un effet IGIS ayant lieu durant le transport de la pollution eurasienne vers les mers de Chukchi et de Beaufort. Enfin, les propriétés macrophysiques des nuages stratiformes en phase mixte, potentiellement affectés eux aussi par l'effet IGIS, ont été caractérisées.

Mots-clés:
climat arctique, sulfates, nuages, effet indirect des aérosols, données satellitaires.

INTRODUCTION GÉNÉRALE

Contexte théorique

La présente thèse s'inscrit dans le cadre des travaux sur l'effet de « rétroaction déshydratation-effet de serre » (RDES), menés essentiellement par les professeurs Jean-Pierre Blanchet et Éric Girard, de l'Université du Québec à Montréal. L'effet RDES constitue un mécanisme complexe par lequel certains constituants de la pollution atmosphérique enclenchent un processus d'assèchement et de refroidissement des masses d'air qui les contiennent durant l'hiver et le printemps arctiques (Blanchet et Girard, 1994; Girard, Blanchet et Dubois, 2005).

Avant de décrire l'effet RDES, il convient de présenter un court historique des observations qui ont suggéré son importance à ses auteurs. Ces observations concernent la distribution et l'action dans l'atmosphère arctique des sulfates, composés qui, par définition, comprennent l'ion SO_4^{2-}. S'il est connu depuis au moins les années 1880 que des substances « sales » se déposent sur la neige arctique durant l'été, suites aux explorations de Fridtjof Nansen et Adolf Erik Nordenskiöld (Garrett et Verzella, 2008), et au moins depuis les années 1950 que des brumes « réductrices de visibilité » se propagent dans la basse troposphère au printemps, suites aux missions militaires de reconnaissance en haute latitude du début de la Guerre Froide (Mitchell, 1957), ce n'est que depuis les années 1970 que le phénomène de brume arctique occupe une place ferme dans la littérature scientifique. La brume arctique est apparentée au smog qui accable les grandes aires urbanisées. Il s'agit d'un mélange de sulfates, de nitrates, de suie et d'autres composés issus de l'activité industrielle aux latitudes moyennes, accompagné de poussières et de particules organiques partiellement naturelles (Law et Stohl, 2007).

Les aérosols (toutes les particules présentes dans l'air, à l'exception des hydrosols formant les nuages et les précipitations) sont dits primaires lorsqu'ils sont directement

injectés dans l'atmosphère, et secondaires lorsqu'ils sont issus de transformations chimiques dans l'air à partir de gaz précurseurs. À l'échelle globale, si on exclut la contribution du sel de mer, les émissions de sulfates sont de l'ordre de 100 téragrammes de soufre par an (Tg S / an) (IPCC, 2001, chap. 5). Environ 65 % de cette quantité résultent des activités humaines, alors que 25 % proviennent de processus biologiques naturels (principalement des rejets du phytoplancton), et 10 % des émissions volcaniques. Seulement 5 % des sulfates anthropogéniques sont de nature primaire. Le reste provient principalement de l'oxydation du DMS (un sous-produit de l'activité phytoplanctonique), du SO_2 (émis par les usines et les engins de transport humains, ainsi que par les volcans) et, dans une moindre mesure, du H_2S. Les chaînes de réaction menant à l'oxydation du soufre, soit à sa combinaison stable avec des atomes plus électronégatifs tels le chlore et l'oxygène, sont complexes (Seinfeld et Pandis, 1998). Il existe différents canaux d'oxydation du soufre dans l'atmosphère, en phase gazeuse (g) comme aqueuse (aq). Les canaux les plus souvent considérés dans les modèles comportant un module de traitement de aérosols peuvent être schématisés ainsi ($précurseur \xrightarrow{réact./catal.} produit$):

$$DMS \xrightarrow{NO_3} SO_2 \text{ (g)} \qquad \text{(I-1)}$$

$$DMS \xrightarrow{OH} SO_2 \text{ (g)} \qquad \text{(I-2)}$$

$$H_2S \xrightarrow{OH} SO_2 \text{ (g)} \qquad \text{(I-3)}$$

$$SO_2 \xrightarrow{OH} SO_3 \xrightarrow{H_2O} H_2SO_4 \text{ (g)} \qquad \text{(I-4)}$$

$$SO_2 \xrightarrow{water} SO_2 \cdot H_2O / HSO_3^- / SO_3^{2-} \xrightarrow{O_3 / H_2O_2} SO_4^{2-} \text{ (aq)} \qquad \text{(I-5)}$$

La conversion des gaz précurseurs en sulfates dépend, entre autres, de la température (qui affecte la solubilité et les temps de réaction), et indirectement de la radiation solaire, nécessaire pour libérer des radicaux OH•. Les produits finaux de l'oxydation sont principalement H_2SO_4 (acide sulfurique), $(NH_4)_2SO_4$ (sulfate d'ammonium) et NH_4HSO_4 (bisulfate d'ammonium). Le sel de mer arraché à la surface océanique par l'action du vent pourrait ajouter de l'ordre de 40 à 320 Tg S / an de sulfates primaires aux émissions

globales (Berresheim, Wine et Davis, 1995), principalement sous forme de Na_2SO_4 et de $MgSO_4$. Les mélanges de sels marins forment des particules relativement grosses qui sédimentent par gravité après avoir parcouru de plus petites distances dans l'air que ne le font les sulfates anthropogéniques. Sirois et Barrie (1999) évaluent que seulement 1 à 8 % des sulfates présents dans le Haut Arctique proviennent du sel de mer, en été comme en hiver.

Les régions d'où origine la brume arctique sont principalement l'Europe et la Russie, toutes deux fortement industrialisées. La Figure I-1 montre la carte des émissions annuelles de SO_2 au nord de 30°N. Les valeurs, établies par Benkovitz et al. (1996), concernent l'année 1985, mais le portrait global n'a pas vraiment changé depuis 25 ans, le Nord-Est de l'Amérique du Nord, l'Europe du Nord et de l'Est, la Russie ainsi que le Sud-Est de l'Asie constituant encore de nos jours les pôles majeurs d'émissions. L'intensité des émissions a cependant évolué, avec des diminutions dues d'une part au combat contre les pluies acides en Occident et d'autre part à l'effondrement économique et industriel de l'ex-empire soviétique, à partir de 1990 environ (Sirois et Barrie, 1999). Dans le Sud-Est asiatique, la forte croissance économique s'est accompagnée d'une intensification des émissions de soufre jusqu'en 1996, suivie d'une légère décroissance jusqu'en 2000 (Stern, 2005). Toutes ces régions contribuent à la brume arctique, mais dans des proportions différentes, suivant certaines considérations géographiques et atmosphériques. L'Europe et l'URSS ont été désignées comme contributeurs principaux entre autres par Rahn (1981) et Carlson (1981), le premier se basant sur une analyse chimique des métaux présents en trace dans la brume arctique, et le second sur l'extension verticale de celle-ci. Christensen (1997) a pour sa part estimé à l'aide d'un modèle numérique du transport atmosphérique du soufre que l'Asie (excluant l'ex-URSS) et l'Amérique du Nord ne contribuaient qu'à hauteur de 3 % du soufre déposé dans l'Arctique en hiver (période 1990-1994), alors que ces pourcentages étaient de 28 % pour l'Europe, 17 % pour la Péninsule de Kola, 17 % pour Norilsk (deux pôles industriels russes) et 28 % pour le reste de l'ex-URSS. Ces proportions s'expliquent tout d'abord par la proximité, puis par l'extension moyenne du front polaire (AMAP, 1998), illustré sur la Figure I-2 pour l'hiver et l'été. Ce front constitue une zone de fort gradient horizontal de température, en entrant dans laquelle les masses d'air arrivant du sud s'élèvent et se refroidissent, ce qui résulte en la formation de nuages précipitants qui lessivent la pollution. Les polluants injectés dans l'atmosphère ont donc une plus grande probabilité

de rejoindre le Haut Arctique si l'opération a lieu à l'intérieur de la masse d'air arctique délimitée par le front polaire plutôt qu'à l'extérieur. Cela explique partiellement que les concentrations hivernales en sulfates soient plus élevées que durant l'été. Les canaux d'oxydation comptent aussi pour beaucoup dans le cycle du soufre, les concentrations étant en fait maximales en avril (Sirois et Barrie, 1999), lorsque le retour de la lumière permet aux radicaux OH• d'oxyder le SO_2 en SO_4 (équation I-4). Les mécanismes de retrait des sulfates sont le lessivage (déposition humide) et la sédimentation gravitationnelle (déposition sèche), la déposition humide étant légèrement plus importante (Dastoor et Pudykiewicz, 1996).

Une autre spécificité de l'atmosphère arctique, permettant aux sulfates de se retrouver à des milliers de kilomètres de leurs régions sources, réside dans la structure verticale de l'air arctique. La surface n'étant pas ou que peu ensoleillée durant la saison froide, l'atmosphère se stratifie en couches dont la température potentielle augmente avec l'altitude, contraignant ainsi le mélange vertical. Ces inversions de températures se produisent de l'ordre de 80 % du temps durant l'hiver arctique (Jaffe, 1991), ce pourcentage approchant les 100 % dans le Haut Arctique (Curry et al., 1996). En présence d'inversions de températures, les parcelles d'air s'écoulent suivant les isentropes (lignes de température potentielle constante), qui s'élèvent doucement vers le centre de l'Arctique (Raatz, 1991). Cet écoulement laminaire peut être compromis en présence de vents trop forts ou de réchauffement en surface dû à l'effet de serre des nuages.

La phase sous laquelle apparaissent les sulfates est importante pour pouvoir déterminer leurs effets climatiques. Les principaux sulfates sont des composés hydrophiles possédant une volatilité quasi nulle, ce qui fait qu'une molécule nouvellement formée demeure très peu longtemps dans la phase gazeuse et s'agglutine rapidement avec des semblables et/ou des molécules d'eau. La substance H_2SO_4 est dite hygroscopique, c'est-à-dire qu'elle croît par absorption d'eau (provenant de la phase vapeur) à n'importe quelle valeur d'humidité relative (Andreae, Hegg et Baltensperger, 2008), alors que le $(NH_4)_2SO_4$ et le Na_2SO_4 sont déliquescents, absorbant de l'eau à des humidités relatives par rapport à l'eau (HR_w) respectives d'environ 80 % et 84 % (c'est leur point de déliquescence). Par un effet d'hystérésis, ces substances ne s'assèchent qu'à des HR_w respectives d'environ 37 % et 58 % (points d'efflorescence). Malgré des variations dans les points de déliquescence et d'efflorescence en fonction de la taille de la

particule et la température (Onasch et al., 1999), les valeurs relativement élevées d'HR du côté arctique eurasien durant l'hiver (Peixoto et Oort, 1996) font en sorte que la phase cristalline des sulfates n'y existe à toute fin pratique pas. En fait, lorsqu'il est question de sulfates, il conviendrait de parler de solutions sulfatées et d'imaginer une multitude de petites gouttelettes sphériques en suspension dans l'air. Les sulfates sont considérés comme de petites particules, avec, par exemple, un pic du spectre de masse pour un diamètre de l'ordre de 0.26-0.45 μm (dans le mode d'accumulation) dans l'Arctique canadien en février (Hoff et al., 1983). En comparaison, les particules de sel de mer (solutions salées) ou de poussière de désert (insolubles), arrachées mécaniquement des surfaces océanique ou terrestre par le vent, ont un rayon effectif (rayon qu'aurait une sphère de même volume) de l'ordre de 1-10 μm (mode géant). Dans un même volume d'air, les sulfates peuvent co-habiter avec d'autres aérosols, soit en demeurant physiquement séparés (mélange externe), soit en fusionnant en des entités plus volumineuses (mélange interne). Généralement, le degré de mélange interne des sulfates s'accroît avec le temps après qu'une masse d'air se soit chargée de ceux-ci ou de ses précurseurs (Hara et al., 2003). Bigg (1980) a détecté de l'acide sulfurique sur 80 % des aérosols à Barrow (Alaska) durant les périodes de décembre 1976 à mars 1977 et de mars à mai 1978.

La présence de sulfates dans l'atmosphère arctique affecte le climat d'au moins deux façons: en agissant directement sur le transfert radiatif (propagation du rayonnement), puis en modifiant les propriétés microphysiques des nuages, ces derniers influençant eux aussi le transfert radiatif. La grande variété dans la taille, la forme et la nature des composés solubles et insolubles, ainsi que le degré variable des mélanges internes/externes, rendent tout modèle des propriétés optiques de la brume arctique fortement simplifié. Blanchet et List (1983) ont proposé un modèle de la brume arctique à deux composantes, l'une constituée d'aérosols insolubles recouverts d'une solution sulfatée, et l'autre de gouttelettes sulfatées comprenant les autres aérosols solubles. Le calcul des propriétés optiques démontre que l'effet des sulfates consiste à augmenter à la fois la rétro-diffusion et l'absorption du rayonnement, et ce d'autant plus que l'HR est élevée. La suie, un composé anthropogénique accompagnant souvent les sulfates, favorise surtout l'augmentation de l'absorption par la brume arctique. Durant l'hiver, lorsqu'il n'y a pas ou que peu de lumière visible, l'effet de rétro-diffusion est faible, puisque le coefficient volumique de diffusion est de l'ordre de 100 à 1000 fois moins élevé pour le

rayonnement thermique (~ 10^{-4}-10^{-3} km^{-1}) que pour le rayonnement visible (~ 10^{-1} km^{-1}) (Blanchet et List, 1983). Cette différence n'est pas aussi marquée dans le cas de l'absorption, mais les valeurs du coefficient volumique d'absorption demeurent relativement basses (~ 10^{-3}-10^{-2} km^{-1}), surtout en l'absence de suie.

Ce sont les effets indirects des sulfates qui comptent le plus pour le climat durant l'hiver arctique. Ces effets sont complexes, mais les points de départ de l'action des sulfates peuvent être décrits en deux processus, une augmentation de la concentration en sulfates pouvant d'une part constituer une augmentation de la concentration en noyaux de condensation (NC) (Lohmann et Roeckner, 1996), et d'autre part impliquer la désactivation d'une fraction des noyaux glaçogènes (NG) (Pruppacher et Klett, 1997). Le premier effet vient de ce que les sulfates, tout comme les sels de mer et d'autres substances solubles, comptent parmi les bons NC, puisqu'ils attirent et concentrent l'eau pour former un embryon qui peut s'activer en gouttelette lorsque l'HR_w atteint 100 % (environ, à cause de des effets de courbure et de solution qui altèrent l'HR_w requise pour l'activation). Cet effet est relativement bien connu, ainsi que ses conséquences immédiates, telles l'accroissement de l'albédo (Twomey, 1977) et de la durée de vie (Albrecht, 1989) des nuages. Dans l'Arctique, l'accroissement de la concentration en NC par les sulfates a plausiblement conduit à un réchauffement en surface depuis le début de l'ère industrielle (Garrett et Zhao, 2006; Lubin et Vogelmann, 2006).

L'effet de désactivation des NG par les sulfates est peu discuté dans la littérature (relativement à comment le sont les effets Twomey et Albrecht), et ce même si des observations de concentration en NG en amont et en aval du vent autour de centres urbains suggèrent depuis longtemps son importance, et que des processus explicatifs ont été suggérés (Pruppacher et Klett, 1997). Les observations de Borys (1989) ont démontré que la désactivation des NG pouvait aussi avoir lieu dans les masses d'air chargées en brume arctique, avec une diminution de la concentration en NG par un facteur de l'ordre de 10^1 à 10^3. Les bons NG incluent des particules argileuses telles la kaolinite et la montmorillonite (Zuberi et al., 2002), issues des sols naturels, ainsi que, dans une moindre mesure, la suie (DeMott et al., 1999). Ces particules contiennent à leur surface des sites actifs, souvent des incurvations ou des étendues dont la structure cristalline est compatible avec celle de la glace. Une gouttelette d'eau peut geler sans que la cristallisation prenne naissance sur le site actif d'un aérosol, mais afin que ce processus

dit de gel homogène se produise, la température doit descendre aussi bas que T_{homog} = -39°C, valeur qui diminue avec la présence de solutés tels l'acide sulfurique (Bertram, Patterson et Sloan, 1996). La présence simultanée de cristaux de glace et de gouttelettes liquides dans des nuages (alors dits en phase mixte) ayant une température supérieure à T_{homog} démontre qu'il existe d'autres modes de nucléation, dits hétérogènes. Ces modes impliquent tous l'action d'un NG, qui peut opérer a) en permettant la conversion de vapeur d'eau en glace à sa surface (NG ou mode de déposition), b) en provoquant le gel d'une gouttelette au contact de sa surface extérieure (contact), c) en pénétrant la gouttelette pour en initier la cristallisation depuis l'intérieur (immersion/gel), ou encore d) en initiant la cristallisation après avoir permis la condensation (condensation/gel). Le mode de déposition peut s'activer dès que l'HR atteint ou dépasse la valeur de saturation par rapport à la glace (HR_i = 100 %), alors que les trois autres modes nécessitent l'atteinte ou le dépassement d'une HR plus élevée, soit la valeur de saturation par rapport à l'eau. En général, l'habilité d'un aérosol à initier le gel croît avec sa taille (Welti et al., 2009; Marcolli et al., 2007). Une particule a le potentiel d'opérer dans aucun, un seul ou plusieurs modes de nucléation. Diverses variantes des quatre modes de nucléation traditionnellement discutés ont été proposées (Khvorostyanov et Curry, 2004; Durant et Shaw, 2005).

De récentes expériences en laboratoire démontrent que les sulfates peuvent altérer le pouvoir de nucléation des NG qu'ils recouvrent. Cette action se traduit par une augmentation de la valeur de HR_i qui doit être atteinte pour que le gel se produise, ce qui implique que pour un certain intervalle de température, le gel est inhibé. On parle alors d'effet d'inhibition du gel induit par les sulfates (IGIS). La liste des modes de nucléation impliqués n'a pas encore été établie avec certitude, mais le mode de nucléation l'est clairement. En effet, des expériences en laboratoire menées par Eastwood et al. (2009) ont démontré que des particules de kaolinite recouvertes de H_2SO_4 nécessitent environ 30 % plus de sursaturation par rapport à la glace pour initier le gel par déposition dans l'intervalle de températures 233-246°K, alors que des particules recouvertes de $(NH_4)_2SO_4$ subissent un effet similaire à 240°K et à 245°K (et un effet réduit à 236°K). Aucun rapport d'expérience similaire concernant les autres modes de nucléation n'a été trouvé dans la littérature. Cependant, il est raisonnable de supposer que l'effet IGIS s'applique au mode de contact, puisque le NG pourrait traverser la surface d'une gouttelette ou encore rebondir dessus sans lui toucher directement, mais qu'il s'applique

plus difficilement aux modes de condensation/gel et d'immersion/gel, puisque la solution sulfatée devient fortement diluée après l'activation de la gouttelette. Notons que de Boer, Hashino et Tripoli (2009) soutiennent que le mode d'immersion/gel pourrait être affecté dans le sens de l'effet IGIS.

L'effet IGIS, qui constitue une explication pertinente des observations de Borys (1989), pourrait avoir de profondes conséquences pour le climat arctique. Le mécanisme de rétroaction déshydratation-effet de serre (RDES), proposé par Blanchet et Girard (1994), en constitue une illustration. Ce mécanisme a été imaginé dans le cadre de recherches sur les nuages en phase mixte dans la basse troposphère arctique, et peut se décrire comme suit (par rapport à une situation d'absence de sulfates). Par l'effet IGIS, la distribution des températures du gel hétérogène est étirée vers les valeurs plus basses, ce qui fait qu'une masse d'air ayant dépassé la saturation par rapport à la glace voit un plus petit nombre de cristaux se développer. La compétition pour la vapeur d'eau étant alors plus faible, il devient plus probable pour les cristaux de croître jusqu'à la taille nécessaire pour précipiter. Or, comme l'effet de serre du contenu en eau totale diminue une fois la sédimentation initiée, il s'ensuit une accélération du refroidissement déjà en cours dans la masse d'air, puis l'activation d'une autre série de cristaux, donnant ainsi lieu à une rétroaction. Des descriptions similaires sont fournies par Girard, Blanchet et Dubois (2005) ainsi que Girard et Stefanof (2007). Ce mécanisme suppose que l'étirement de la distribution des températures de gel est suffisamment important pour que l'accélération du refroidissement ne permette pas de retomber en situation de nucléation simultanée d'un trop grand nombre de cristaux, dans lequel cas la compétition pour la vapeur d'eau demeurerait élevée. Le mécanisme théorique RDES exclut aussi de sa définition tout potentiel effet de rétroaction négative impliquant les variables du système plus vaste dans lequel il s'intègre. Une preuve complète de l'importance climatique du mécanisme RDES, dont l'effet IGIS constitue le déclencheur, doit passer dans un premier temps par la preuve que chaque maillon de la chaîne de causalité s'applique véritablement à l'atmosphère hivernal arctique, puis dans un second temps par la démonstration que le mécanisme RDES dans son ensemble est dominant, c'est-à-dire qu'il n'est pas amorti par une somme de rétroactions négatives et qu'il laisse une trace significative sur les différentes variables climatiques concernées (nébulosité, précipitations, températures de surface, etc.). La Figure I-3 illustre de façon schématique le mécanisme RDES.

L'effet RDES a jusqu'ici surtout été étudié et supporté théoriquement, par l'introduction de l'effet IGIS dans un modèle numérique du climat, tel qu'on peut penser qu'il agit à partir de ce qui a été observé en laboratoire et par Borys (1989). La plus récente étude publiée à ce sujet est celle de Girard et Stefanof (2007), qui ont utilisé le *Northern Aerosol Regional Climate Model* (NARCM) afin d'évaluer l'impact de l'effet RDES durant le mois de février 1990. Ce modèle calcule l'action de 5 familles d'aérosols (sels de mer, sulfates, suie, carbones organiques et poussières minérales), chacune divisée en 12 modes de taille. Les principaux processus liés aux aérosols (émissions, production chimique, croissance, coagulation, nucléation par contact et immersion/gel, condensation, déposition sèche, lessivage par les précipitations, etc.) sont incorporés dans NARCM, qui comporte aussi une microphysique détaillée. L'effet IGIS est introduit via un facteur (multiplicatif) de réduction (F_r) de la concentration en NG de contact et d'immersion/gel qui s'exprime comme suit:

$$F_r = 10^{-B[SO_4]} \tag{I-6}$$

où $[SO_4]$ représente la concentration en sulfates et où B est une constante de calibration choisie de telle sorte que l'ordre de grandeur des concentrations en sulfates maximalement atteintes dans l'Arctique (~ 10 µg / m^3) rendent F_r minimal en vertu des observations de Borys (1989). Les résultats de Girard et Stefanof (2007) comportent une anomalie de refroidissement en surface variant entre 0 et 2.5°C dans le Haut Arctique, par rapport au climat non-perturbé (ou de contrôle) du modèle. Les perturbations des contenus en eau et en glace des nuages, ainsi que de l'efficacité de déshydratation, du flux descendant de radiation infrarouge à la surface et du couvert nuageux suggèrent que le mécanisme RDES est à la fois cohérent et dominant. Cependant, en raison des conditions d'observation plutôt hostiles en Arctique durant l'hiver, ces résultats de modélisation manquent d'un support observationnel à l'échelle pan-arctique.

Durant le développement des missions satellitaires CloudSat et CALIPSO, deux plateformes transportant respectivement un radar et un lidar mises en orbite en avril 2006, il y avait lieu d'espérer qu'une confirmation de l'importance du mécanisme RDES puisse être trouvée. En effet, les deux satellites se suivent sur la même orbite en sondant à toute fin pratique les mêmes parcelles d'air, et leurs bases de données sont complémentaires,

puisque le radar détecte les nuages à gros cristaux ainsi que les précipitations, alors que le lidar peut détecter les aérosols et les cristaux de toutes tailles, sauf lorsque le faisceau devient atténué. C'est dans ce contexte que j'ai joint le groupe de recherche du professeur Jean-Pierre Blanchet, avec la mission de trouver une preuve observationnelle du mécanisme RDES dans la couche limite à l'aide des données de CloudSat et de CALIPSO.

Figures

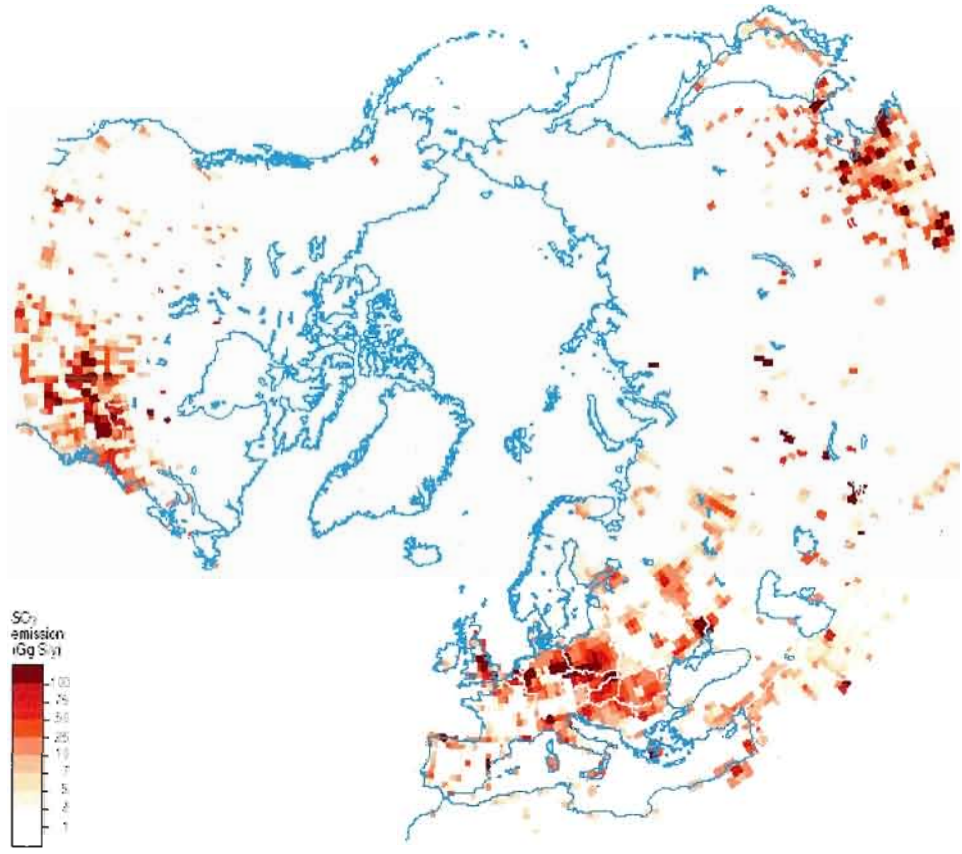

Figure I-1: Émissions annuelles de dioxyde de soufre au nord de 30°N, par point de grille (1° x 1°) et pour l'année 1985. Source: AMAP, 1998 (de la base de données GEIA).

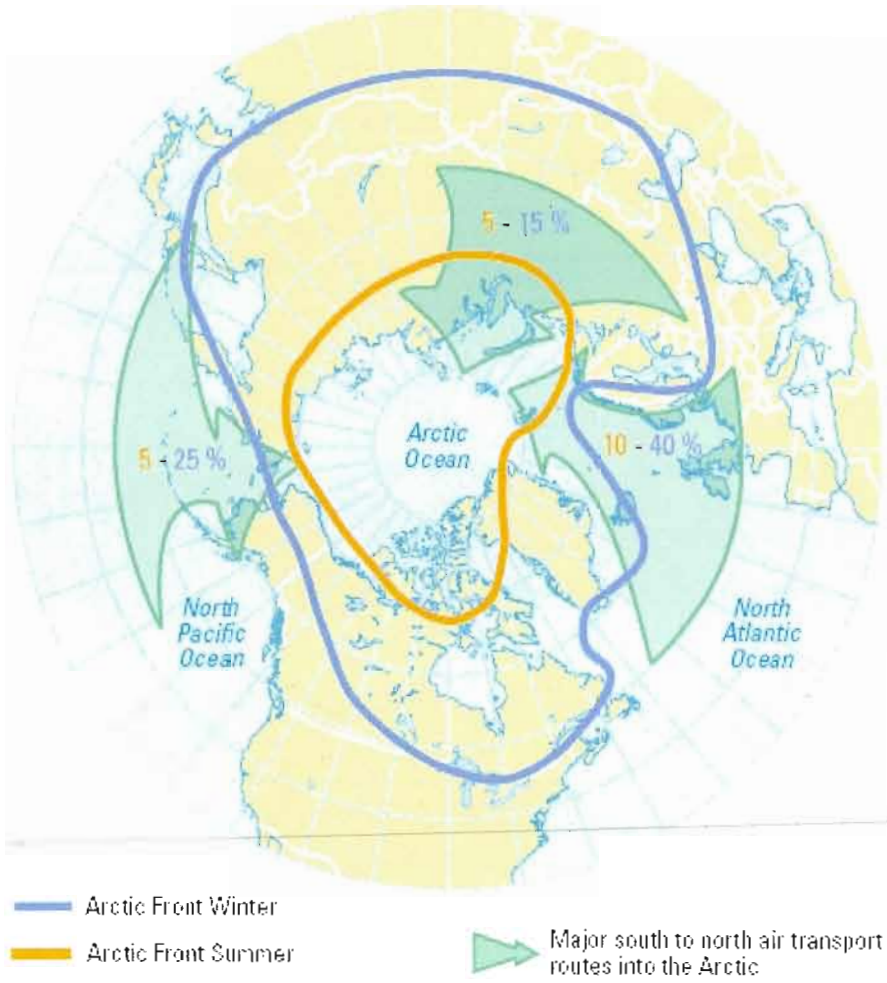

Figure I-2: Positions moyennes du front arctique en hiver et en été, avec les zones majeures d'entrée de l'air dans l'Arctique. Source: AMAP, 1998.

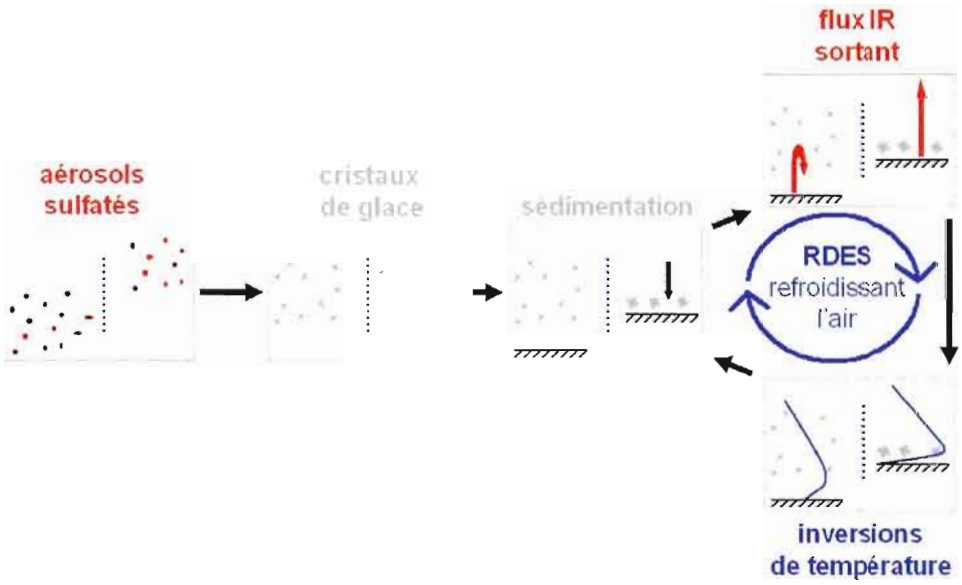

Figure I-3: Schéma du mécanisme RDES, avec dans chaque case le scénario de contrôle sur la gauche et le scénario perturbé sur la droite.

CHAPITRE I

STUDY OF POLAR THIN ICE CLOUDS AND AEROSOLS SEEN BY CLOUDSAT AND CALIPSO DURING MID-WINTER 2007

Patrick Grenier*, Jean-Pierre Blanchet and Rodrigo Muñoz-Alpizar

Institut des Sciences de l'Environnement, Université du Québec à Montréal

*corresponding author: grenier@sca.uqam.ca

Published in *Journal of Geophysical Research.*

Hereinafter: Grenier, Blanchet and Muñoz-Alpizar (2009), or GBM (2009)

Grenier P., Blanchet J.-P. and Muñoz-Alpizar R. (2009) Study of Polar Thin Ice Clouds and Aerosols Seen By CLOUDSAT and CALIPSO During Mid-Winter 2007, *J. Geophys. Res.*, 114, D09201, doi:10.1029/2008JD010927.

Abstract

Data sets from CloudSat radar reflectivity and CALIPSO lidar backscattering measurements provide a new regard on Arctic and Antarctic winter cloud systems, as well as on the way aerosols determine their formation and evolution. Especially, links between the cloud ice crystal size and the surrounding aerosol field may be further investigated. In this study, the satellite observations are used to heuristically separate polar thin ice clouds into two crystal size categories, and an aerosol index based on the attenuated backscattering and color ratio of the sampled volumes is used for identifying haze in cloud-free regions. Statistics from 386 Arctic satellite overpasses during January 2007 and from 379 overpasses over Antarctica during July 2007 reveal that sectors with the highest proportion of thin ice clouds having large ice crystals at their top are the same for which the aerosol index is highest. Moreover, a weak but significant correlation between the cloud top ice effective radius and the above-cloud aerosol index suggests that more polluted clouds tend to have higher ice effective radius, in 10 of the 11 sectors investigated. These results are interpreted in terms of a sulphate-induced freezing inhibition effect.

1.1. Introduction

Due to the paucity of scientific observations, clouds in the polar regions are poorly known relative to those at lower latitudes, and this contributes to the large range of uncertainties in present-day and future simulations of the polar climates (IPCC, 2007, chap. 11). The lack of knowledge about clouds is particularly acute during dark months, in part because visual observations are difficult, but also because satellite infrared passive measurements cannot easily discriminate between cloud top and surface emissions, mainly due to the frequent low-level temperature inversions (Serreze and Barry, 2005). Therefore, cloud climatology varies largely among sources. Curry et al. (1996) have reviewed several of them to conclude that the mean cloud fraction ranges broadly between 40 and 68 % during the Arctic winter, increasing to 80 % if the generally unreported clear-sky ice crystal precipitation (diamond dust) is taken into account. They also mention regional disparities, the lowest wintertime cloud cover being over the Canadian Arctic and the highest over West Eurasia. Over Antarctica, cloud climatology is also highly variable among authors, for similar reasons. For the latitude bands between $65°S$ and $80°S$ during the period 1982-91, Hahn, Warren and London (1995) have computed a mean wintertime cloud cover ranging from 78 to 85 % over the ocean (from ship observations) and from 47 to 69 % over land stations, with values increasing equatorward. Again, these values could be higher if diamond dust was included. Walden, Warren and Tuttle (2003) reported a 91 % frequency of occurrence of these slowly precipitating crystals during 6 winters at the South Pole. Other properties, like regional distribution, base and top heights, particulate phase and concentration, ice effective radius and droplet size, also need more study for evaluation of the role of polar clouds in the atmospheric energy balance.

Limited knowledge of the processes determining microphysical properties of clouds also hinders their proper simulation by numerical models. In particular, the interaction of the atmospheric water content with the aerosol field consists of a myriad of mechanisms, and it is not clear which of them dominate in cloud systems. During the Arctic polar night, sulphates represent an important aerosol species in terms of their impact on clouds, due notably to their high mass fraction in the total aerosol, their hydrophilic property and their ability to inhibit ice nucleation. Christensen (1997) estimated that European and Russian sources account for about 90 % of anthropogenic

sulphates injected into the Arctic air mass north of $75°N$, but the proportion coming from Southeastern Asia has probably increased since the publication of his study, due to an enhanced industrial activity. Also, contributions from the European and North American sources may vary with the prevalent circulation associated with the NAO phases (Eckhardt et al., 2003). In terms of concentrations, a decrease has been observed at the surface from the early 1990s until at least 2003 (Sirois and Barrie, 1999; Quinn et al., 2007), due to SO_2 emission control in Europe and to the collapse of the Russian economy at the beginning of this period. So, at first approximation, it is most possible that radiative indirect effects induced by sulphates have decreased in strength during the last 20 years over the Arctic as a whole. However, in terms of sulphate-to-aerosol mass ratio, the decrease within the Arctic haze could be less pronounced, because of a decline in the concentration of some other pollutants, like black carbon (Sharma et al., 2004). Therefore, it is also possible that some indirect effects linked to the aerosol acidity (instead of the sulphate absolute concentration) have kept sustained strength during this period, and even increased over some sectors. Over Antarctica, the aerosol is also very acidic during winter, due to the presence of sulphates which originate mostly from biological processes in the surrounding oceans (Shaw, 1988). However, sulphate absolute concentrations are much lower than in the Arctic, and haze episodes are rare. Trends in the polar aerosol composition influence the cloud cover, which in turn influences the radiative budget and surface temperatures (Liu, Key and Wang, 2008).

One particular property of the aerosol field which impacts on cloud properties is the concentration of ice forming nuclei (IFN). Observations by Borys (1989) indicate that the IFN concentration may be reduced by 1 to 3 orders of magnitude during Arctic haze events. These field measurements are consistent with the sulphate aerosol acting as an ice nucleation inhibitor, and we refer to this interaction as the sulphate-induced freezing inhibition (SIFI) effect. Unfortunately, laboratory results do not currently allow for a full understanding of this phenomenon, because of the great variety in the aerosol composition and size, as well as in the thermodynamic state. For example, Knopf and Koop (2006) have conducted experiments which show that the (heterogeneous) ice nucleation on some mineral dust particles is not significantly affected by H_2SO_4 (sulphuric acid) coating, in a temperature range relevant for the Arctic troposphere. However, other results by Archuleta, DeMott and Kreidenweis (2005) show that for a lower temperature interval and different mineral dust compounds, sulphuric acid may

considerably shift the supersaturation (and hence the temperature) required for ice nucleation to occur, towards lower or higher values. $(NH_4)_2SO_4$ (ammonium sulphate) coating may also affect the ability to nucleate ice (Eastwood et al., 2009). So, recent laboratory results as a whole neither directly support nor invalidate the SIFI hypothesis, and more data are needed for connecting field observations by Borys (1989) to laboratory experiments.

Recently, Prenni et al. (2007) have demonstrated the important role of IFN concentrations in Arctic mixed-phase cloud model representations, and emphasized that their parameterization for the Arctic environment should differ from that for mid-latitudes. Consistently, Blanchet and Girard (1994) and Blanchet (1995) have argued that the SIFI effect favours large ice crystal populations in the boundary layer, like diamond dust, at the expense of non-precipitating ice clouds or ice fog. Numerical simulations by Girard, Blanchet and Dubois (2005) have demonstrated that the SIFI effect triggers an important indirect climate effect in which clouds, precipitation and longwave radiation interact. Their simulations show that this process, called dehydration-greenhouse feedback (DGF), causes a strengthening of the surface temperature inversions by several degrees during Arctic haze events, because larger ice crystals in air masses entering the Arctic are associated with a higher dehydration efficiency and with a lower water vapour greenhouse effect, whereas subsequent cooling feeds back into further dehydration. The DGF is most effective in the Arctic during winter, due to a particular temperature regime. As temperatures decrease below about $-30°C$, the Planck function shifts towards the water vapour rotation band in the far infrared, while the transmittance increases rapidly above 17 μm (in the so-called "dirty window") with lowering water vapour concentrations. Because sulphuric acid coating of natural IFN is likely limiting freezing in the same temperature range, the DGF may represent an efficient climate-altering process. Possibly, the DGF is the strongest indirect effect of aerosols on climate, at least on a regional and seasonal basis. So far, this process was thought to be significant mostly in the boundary layer, but recently, with CloudSat and CALIPSO measurements, we found that a similar mechanism could take place higher in the Arctic troposphere.

In this study, satellite measurements are used to investigate where the SIFI effect could be most significant during the polar dark months, and to what extent it may affect the size of ice crystals in light precipitation. We analyse and compare clouds and aerosol

distributions for winter conditions in 11 sectors of the Arctic and Antarctic regions. The paper starts with a brief description of the CALIPSO and CloudSat data sets used, and the classification algorithm is described subsequently. Next, statistical and correlational calculation results are presented, and implications for the SIFI effect and the DGF mechanism are discussed. A new cloud classification of thin ice clouds (TIC) relevant to polar climate studies is proposed.

1.2. Observational data sets

1.2.1. CALIPSO data set

CALIPSO was launched on April 28th, 2006 and joined the A-Train constellation on a heliosynchrone orbit at an altitude of 705 km. The CALIOP instrument (Cloud-Aerosol Lidar with Orthogonal Polarization) aboard the platform is probing the atmosphere with a Nd:YAG laser, which produces pulses of 110 mJ at 532 nm and 1064 nm. Pulses have a length of 20 nsec (~ 6.7 meters). The satellite tangential speed of about 7.5 km•sec^{-1} and the lidar pulse repetition rate of 20.16 Hz allow for a sampling profile at every ~ 333 meters on the ground, whereas the footprint is ~ 70 meters, due to a beam divergence of 100 μrad. Data above 8.2 km are averaged with the 2 neighbouring profiles for a resolution of 1 km, whereas above 20.2 km the resolution decreases to 1.667 m. In the vertical dimension, the 532 nm signal resolution is 30 meters between -0.5 and 8.2 km, 60 meters between 8.2 and 20.2 km and lower above 20.2 km. Further technical details about the mission may be found in a document by Hostetler et al. (2006), and an early assessment of the initial performance of CALIOP has been documented by Winker, Hunt and McGill (2007).

For this study, we used the total (β_{532}) and perpendicular (β_{per}) attenuated backscattering fields at 532 nm. The beam is sent polarized, and a depolarization beam splitter in the receiver allows for a measurement of the perpendicularly polarized component in the return signal. The polarization lidar technique (Sassen, 1991) has been applied for the detection of ice crystal layers, as explained later. We also used the total attenuated backscattering field at 1064 nm (β_{1064}), for characterizing haze layers. Each measurement value (583 levels per profile) is geo-referenced (latitude, longitude, altitude,

along with time). In this study, we used the first version (V1) of the CALIPSO primary signals (data available in October 2007). Our conclusions may be modulated by newer data versions, but will not likely be fundamentally changed.

Figures 1.1a and 1.2a show 4000 km-wide night-time β_{532} transects over the Arctic (January 19th, 2007) and Antarctic (July 20th, 2007) regions respectively. Horizontal resolution has been degraded to about 1100 m by averaging along-track and to 240 m in the vertical, for matching with the CloudSat products. It is intuitively expected that clouds, haze layers and clear air backscatter and absorb the lidar beam energy in decreasing orders of intensity. However, because this is plausibly only true in average, and because the beam gets strongly attenuated as it penetrates optically dense features, complementary information is needed before assigning a feature tag (cloud, haze, or clear-air) to each volume bin. Nevertheless, let us mention two interesting features that will be discussed later. The first is the boundary layer aerosol mass in the Arctic scene, between the tick marks at $98.0°E$ and $111.7°E$. Inspection of ECMWF reanalysis (not shown) suggests that this haze event detected by CALIPSO between the Taimyr Peninsula and the Bolchevik Island is occurring because a relatively high southward pressure gradient maintained along the Eurasian northern coasts during the previous days has transported pollution from Norilsk and/or the Kola Peninsula, but a numerical trajectory analysis is necessary to determine with more precision the origin of this polluted air mass. The transport of aerosol from Eurasia into the Arctic during January 2007 is discussed by Muñoz-Alpizar et al. (in preparation). The second feature consists of the polar stratospheric clouds (PSCs) over Antarctica, above the altitude of 12 km and approximately between the tick marks at $64.9°E$ and $108.9°E$. In the CALIPSO data set, this type of cloud is dominant in winter over the Antarctic continent, and seldom found at its antipode, at least below 15 km and during the winter month investigated for this study.

1.2.2. CloudSat data set

CloudSat joined the A-Train orbit at the same time as CALIPSO, the latter lagging by about 15 seconds. Hence, measurements from both platforms are nearly coincident in space and time. The Cloudsat payload instrument is the Cloud-Profiling

Radar (CPR), with a frequency of 94 GHz (3 mm wavelength). A profile sampling is performed at every ~ 1100 meters on the ground, with a 1.4 x 2.5 km footprint (cross-track x along-track), whereas the vertical sampling is 240 meters, performed at 125 levels. More technical details about the CloudSat mission are documented by Stephens et al. (2002).

The CloudSat primary (or level 1B) product is the radar reflectivity, in dBZ_e. Retrieved microphysical properties include the ice effective radius (r_{ie}) from the R04 2B-CWC product (level 2). We used this field in our cloud classification algorithm in place of level 1B, mostly because it is geo-referenced. The level 2 retrieval algorithm (first version) has been formulated by Austin and Stephens (2001). Because Kahn et al. (2007) have found that the radar sensitivity is greatly reduced in the first 3-4 levels above the surface, we excluded data in the first kilometre above the surface (about 4 levels) from the analysis. This surface contamination effect in boundary layer data results from the radar pulse length of 1000 meters (Schutgens and Donovan, 2004). The R04 ECMWF-AUX temperature field, which consists of the ECMWF analysis interpolated at the CloudSat sampling positions, is also used.

Figures 1.1b and 1.2b show the r_{ie} fields corresponding to the CALIPSO β_{532} scenes presented previously. It cannot be deduced from this image that the radar does not see the wide low-level aerosol layer in the Arctic scene, since data for the first kilometre above the surface are removed, but inspection of the corresponding primary field (radar reflectivity, not shown) reveals no salient feature in this region. Also, a 1-2 km-thick band of intense backscattering at the top of the 2 cloud systems in the first 1000 profiles (on the right) is not seen by the radar (in the primary field). In the Antarctic scene, about half of the cloud volume transected by the lidar beam is missed by the radar, and the PSCs are not captured at all (also in the level 1 signal). Our classification of ice clouds is based on these differences, as explained below.

1.2.3. Investigation zones and periods

Although sulphate concentrations and acidity in the Arctic culminate in April (Sirois and Barrie, 1999), we believe that the SIFI effect could be most important in

January, when temperatures are much colder. For this reason, we selected January and July (coldest month in Antarctica) of 2007 for starting our investigation, but other cold months also deserve study in regard of the SIFI effect. CloudSat and CALIPSO cross the Arctic 14 or 15 times a day, but there are a few orbits whose data were not available at the moment of doing the analysis. For January 2007, data from 386 night-time orbits have been used, for a total of 1 417 289 profiles. For July 2007 over Antarctica, 1 673 900 profiles from 379 overpasses have been investigated. These data sets are hereinafter respectively referred to as ARC-386 and ANT-379. For some of the results presented later, subsets of 30 (Arctic) or 31 (Antarctica) granules (overpasses) have been used, and these are named ARC-030 and ANT-031.

The regions beyond the polar circles are vast ($\approx$ 21 millions km^2) and heterogeneous in terms of many parameters that can potentially affect cloud populations, so that we have partitioned the polar areas in our analysis. For example, the Greenland plateau consists of a singular orographic environment, whereas the North Atlantic open waters allow for a higher surface flux of water vapour, sensible heat and sea salt than usually found at their latitudes. Due to the main circulation, meridional aerosol injection into the Arctic is also asymmetric, with higher values on the Eurasian side. Figure 1.3 shows our partitioning of the polar regions, with the exact delimitations and number of investigated profiles presented in Table 1.1. The last two columns of Table 1.1 are discussed later. Unless otherwise specified, all heights are given relative to the sea level.

1.3. Methodology

1.3.1. Feature classification algorithm

The superposition of quasi-synchronous and collocated CALIPSO and CloudSat fields reveals that the instruments have different perspectives on the atmosphere. Indeed, instruments are not sensitive to the same atmospheric constituents, and their respective beams may penetrate at different depths within dense features. The lidar, with a short wavelength, may reveal the presence of very tiny particles on its beam path, including the smallest ice crystals and most aerosol layers. The drawback to this sensitivity is the beam often losing most of its energy before reaching the surface. This frequent situation, that we term "saturation", occurs when the lidar is probing optically thick layers. However,

this is not a serious limitation here since our study focuses on thin clouds detected by the lidar and corresponding to optical depths less than about 3. The radar, by pulsing at a wavelength of 3 mm, cannot detect tiny particles constituting aerosol layers, as well as clouds that are made of crystals smaller than about 28-30 μm (R. Austin, personal communication ; this limit is not fixed and depends on the particle number concentration). For a more precise view of the hydrometeor detection capabilities of the radar, we refer to Mace (2007).

The fact that the radar misses the fraction of ice clouds made of small particles offers a basis for separating clouds into two broad categories: those seen only by the lidar, made of small particles only, and those seen by both instruments, having large ice crystals. The former are termed thin ice clouds of type 1 (TIC-1), whereas the latter are designated as TIC-2, the type referring to the number of active instruments detecting the cloud. The TIC locations and frequencies of occurrence, along with the correlations of their optical properties with those of the surrounding aerosols, may provide evidence for the SIFI effect and clues on cloud processes in polar regions. Although the distinction between TIC-1 and TIC-2 is arbitrarily determined by the radar sensitivity, it conveniently separates suspended from precipitating clouds. Indeed, ice crystal populations having particles larger than 30 μm have a higher probability of being precipitating than those for which the size distribution hardly reaches this threshold. However, this criterion is not perfect, and it is possible that some TIC-2 bins are not significantly precipitating. We are also interested in separating cases with slow ice crystal growth rate from those growing very fast to precipitation size, as such an "explosive mode" could be a signature of the SIFI effect in the atmosphere. For this purpose, TIC-2 are further divided into TIC-2A, TIC-2B and TIC-2C. TIC-2A consist of the vertical extension of slowly growing TIC-1 layers for which it is reasonable to think there is a sustained production of ice supersaturation. Within TIC-1/2A systems, a gradual transition between activation and precipitation sizes takes place. In contrast, TIC-2B are not overlaid by TIC-1, and this is consistent with explosive growth occuring in the formation zone at the cloud top. A third category of TIC-2 is often encountered in polar regions. It occurs at warmer temperatures ($T > -39°C$), in association with mixed-phase clouds. In the lower troposphere, below about 4 km altitude, liquid water clouds frequently form in air largely supersaturated with respect to ice (30 to 40 %). Upon

freezing, droplets also produce explosive growth of a few ice crystals that rapidly sediment below the liquid layer, resulting in crystals seen by both instruments. These features, labelled TIC-2C, are similar to TIC-2B but initiated from liquid phase, due to warmer temperatures.

The algorithm that we have designed for identifying TIC types in the CALIPSO/CloudSat data sets takes into account the numerical values of the β_{532} field, as well as the depolarization and color ratios. The algorithm also considers the ice water content (IWC) field retrieved from the radar reflectivity signal, but only to separate zero from non-zero IWC bins. The ice effective radius (r_{ie}) value is used for statistical calculations, but not for classifying features. Our classification is heuristic in the sense that it allows for a tracking of a cloud type which, we have reasons to think, is particularly affected by the aerosol field (TIC-2B), without the need of developing a complex retrieval algorithm from the lidar fields. The next paragraphs provide a description of the classification algorithm.

First, a smoothing filter is applied to CALIPSO backscattering fields, below 8.2 km, to get 60 m (vertical) and 1 km (horizontal) resolutions. The arithmetic averaging operation allows for a vertical continuity in the β_{532} field, which is necessary for using the same backscattering threshold when discriminating clouds from background aerosols below and above this height. However, a slight discontinuity at 8.2 km remains in the β_{per} and β_{1064} fields, which echoes in the depolarization and color ratios. Next, each CALIPSO profile is associated to the closest CloudSat profile, and the average of the 3 or 4 profiles associated to a same CloudSat profile is performed. The same operation is repeated for the vertical levels (with a resolution of 240 meters for radar data), so that 12 or 16 lidar backscattering values are averaged and associated to 1 radar reflectivity value in the operation of mapping CALIPSO fields on the CloudSat grid. This procedure insures data compatibility, while strengthening the signal-to-noise ratio. Only levels below 15 kilometres are kept for subsequent analysis. Data in the first 1000 meters have been excluded from the TIC statistical calculations, because of the surface contamination problem in the radar, as mentioned before. Next, an analysis is performed to assign a tag to each bin (pixel). Tags may correspond to the following features: cloud-free (molecular and aerosol), TIC-1, TIC-2A, TIC-2B, TIC-2C, mixed-phase, and saturated signal, the

latter being attributed to below-cloud regions in order to exclude from the subsequent aerosol field analysis bins whose backscattering fields could be biased by strong attenuation.

One recurrent feature in the CALIPSO data set is a low-level, thin and highly reflecting layer with a well-defined top, easily confused with the surface. One can see an example of such a cover extending over about 400 km in Figure 1.1a, around the tick mark at $-160.2°E$. Based on the characteristically low depolarization ratio of this kind of cloud cover, we believe that liquid droplets are present most of the time. Our algorithm detects it by using the sharp β_{532} vertical gradients at its top and base, and classifies it as a mixed-phase layer before finding the TICs. Mixed-phase layers are typically overlaid by a $\beta_{532} \le b_1 = 0.0015 \quad km^{-1}sr^{-1}$ cloud-free region and reach a peak value of $\beta_{532} \ge b_2 = 0.0090 \quad km^{-1}sr^{-1}$ within about 1000-1250 meters (4-5 CloudSat vertical bins) below the top.

Next, a pixel is classified as a TIC-2 feature simply if the ice water content in the level 2 CloudSat product is non-zero, unless it has previously been identified as part of a mixed-phase layer. TIC-2 are further separated into TIC-2A if they are found below a sufficiently thick TIC-1 layer, into TIC-2C if they are located under a mixed-phase layer, and into TIC-2B otherwise. When performing the distinction between TIC-2A and TIC-2B, the algorithm seeks for a TIC-1 presence above in the current profile, but also in the neighbouring profiles, for minimizing the effect of holes in the TIC-1 cover. A minimum number of 12 TIC-1 pixels is required, corresponding to a 960 meter-thick layer if they are equally partaken between the 3 profiles, and PSCs are masked during this procedure by requiring a minimal temperature of $-78°C$ for TIC-1 pixels to count. Nevertheless, the distinction may sometimes be erroneous, due to the large diversity of cloud configurations.

The most difficult step in classifying features is no doubt the separation between TIC-1 and aerosol layers, the latter being included in the cloud-free category. This difficulty was also encountered by Vaughan, Winker and Powell (2005) when formulating a CALIPSO feature detection algorithm. The primary distinction between

both features should be a lower average β_{532} value for aerosols, but we found that any fixed threshold leads to a high proportion of misclassifications that are obvious in regard of the visual structure of the field, especially at the edge of clouds. We then choose a relatively low threshold at $\beta_{532\_min} = 0.0009 \ km^{-1}sr^{-1}$, which favours TIC-1 at the expense of aerosols, and relabelled the bins as cloud-free if they did satisfy at least one of three other criteria. The first of these subsequent criteria is based on the depolarization ratio, defined as $\delta \equiv \beta_{per} / (\beta_{532} - \beta_{per})$. A compilation of cloud δ values by Sassen (1991) has led to the conclusion that ice clouds generally have $\delta \geq 0.5$, contrasting with liquid cloud values of $\delta \cong 0$. Small δ values should also characterize aerosols. For example, Ishii et al. (1999) report an average value $\delta \approx$ 1.34 % for Arctic haze during a 4-winter observational campaign at Eureka, Canada. However, as Sassen (1991) mentioned, the off-nadir angle should be at least $\approx 2.5°$ for uniformly oriented ice plates, potentially frequent in the Arctic, to reveal their depolarization property. So, because of the very small off-nadir angle of the CALIPSO laser beam ($\approx 0.27°$) during the months of January and July 2007, some ice crystal pixels could display low depolarization ratios. We then allowed pixels with small δ values to register as clouds if they present relatively high backscattering values, by designing the following relation between the minimal depolarization (δ_{min}) and the backscattering values:

$$\delta_{min} = a_0 + a_1 / \beta_{532} \tag{1.1}$$

A variety of coefficients have been tested, and it appears that $a_0 = 10^{-2}$ and $a_1 = 3 \cdot 10^{-5}$ $km^{-1}sr^{-1}$ are suitable values. Physically, a_0 represents the minimal depolarization value that a pixel must display in order to be registered as a cloud, whereas a_1 determines the slope of the segregating curve in the δ_{min} vs. β_{532}^{-1} plot. The color ratio, defined as $\chi \equiv \beta_{1064} / \beta_{532}$, has also been used, since from visual inspection of many Arctic scenes it seems that clouds present a ratio of $\chi \approx 1$, whereas $\chi \leq 0.5$ characterizes aerosol layers. Based on theoretical calculations from Liu et al. (2002), who have worked on the development of another CALIPSO scene classification algorithm, we adopted the threshold $\chi_{min} = 0.54$ for TIC-1 not satisfying $\beta_{532} \geq 0.0030 \ km^{-1}sr^{-1}$, this last

threshold reflecting our observation that practically no pixel above this backscattering value seems to be part of an aerosol layer. Finally, we used a clustering criterion, so that individual TIC-1 bins, resulting most often from noise, were reclassified as cloud-free.

The temperature field, taken from the ECMWF reanalysis interpolated on the CloudSat grid (CloudSat ECMWF-AUX product), provides an ultimate criterion for determining the cloud phase. TIC pixels for which $T \geq 0°C$ are relabelled as mixed-phase layers (in principle it should be a liquid layer), whereas we considered that below $-39°C$, the homogeneous freezing point, only ice clouds exist.

Figures 1.1c and 1.2c illustrate how our algorithm classifies features seen by CALIPSO and CloudSat (same scenes as before). The first kilometre must be considered with caution since there is no radar data there. A mixed-phase layer is identified over the Beaufort Sea, but some parts of it are misclassified as TIC-1, due to the absence of the steep β_{532} gradient at the base. The major part of the cloud system between tick marks $-176.3°E$ and $111.7°E$ (north of Laptev Sea) is classified as TIC-2B, with the exception of isolated profiles where there are enough TIC-1 pixels at the top for the algorithm to identify a TIC-2A feature. Extended on 1000 km over the Taimyr Peninsula, we see an important TIC-1 layer above a TIC-2A layer, divided in two systems. Some profiles are misclassified as TIC-2B often due to holes in the TIC-1 cover, but most TIC-2B are correctly identified at the edge of one system. All pixels below significant cloud cover are considered lidar-saturated, and the rest is labelled as cloud-free. In the Antarctic scene, the major part of the system over the continent consists of a TIC-1/2A cover, and we see a small TIC-2B cloud formation and an extended mixed-phase cover over the Weddell Sea. PSCs are almost exclusively classified as cloud-free in this scene, but this is not always the case, these features being often partaken between TIC-1 and cloud-free, depending on their β_{532}, δ and χ values. These results are fairly representative of the successes and limitations of the algorithm when applied to other winter polar scenes of January and July 2007 (tests were performed on the 61 scenes of the ARC-030 and ANT-031 subsets to verify the feature classification results).

As introduced before, we believe that TIC-2 populations differ in regard of their main growing processes. The microphysical distinction largely stems from synoptic scale

conditions. Indeed, synoptic systems possessing enough energy to raise air parcels as high as 9-10 km will also reach high ice supersaturation production rates and very likely activate a high proportion of the available ice-forming nuclei (IFN), either by deposition or contact mode. When supersaturation with respect to water is also reached, the condensation-freezing mode allows for even more IFN to be nucleated (Meyers, DeMott and Cotton, 1992). The small ice crystal populations thus formed (TIC-1) stay aloft longer, but precipitation will eventually be formed (TIC-2A). In contrast, when air parcels are slowly lifted, as is often occurring in the cold core of low pressure systems in their cyclolysis phase, equilibrium between deposition and production of ice supersaturation may be reached, for which only large IFN whose acid coating is diluted enough nucleate into ice crystals, thus leading to less competition for water vapour. Ice crystal precipitation is then formed earlier (TIC-2B). TIC-2B may also be found at the edge of more active TIC-1/2A systems, where vertical motion and supersaturation production rate are weaker. The strength of the cooling rate, either from IR emission or adiabatic ascent, may be a key factor discriminating TIC types, since it reflects the production rate of ice supersaturation (but this is not used in this study).

1.3.2. Mean cloud-free backscattering and aerosol index

An important property of the CALIPSO β_{532} field is its mean cloud-free value, since this quantity can be an indicator of the concentration of aerosols in a sector. In fact, aerosols (as well as molecules) contained within cloudy bins also contribute to the measured backscattering. However, because it is extremely difficult, if not impossible, to properly separate their contribution from that of optically dominant liquid and ice particles, interstitial aerosols are not considered in our calculation of the mean cloud-free backscattering profiles presented in Figure 1.4 for the ARC-030 and ANT-031 subsets. One mean profile is presented for each polar region, along with the associated standard deviations (σ). The granules contained in the subsets have been quasi-randomly selected, the only criteria being that each day be represented by at least one overpass (except when no data were available) and that transect orientations vary greatly, so that all sectors be represented many times. The high σ values at several levels, which are associated to cases where aerosols are difficult to distinguish from TIC-1, illustrate another limitation one faces when using an aerosol indicator based on the β_{532}

information alone. In an attempt to minimize the impact of tenuous and misclassified TIC-1 layers on the aerosol signal, an aerosol index (α) which also considers the color ratio χ ($\equiv \beta_{1064}/\beta_{532}$) has been created and computed for each cloud-free pixel. It is defined as:

$$\alpha \equiv \frac{w_\beta \cdot \min(\beta_{532}/2\beta_{ref},1) + w_\chi \cdot \max(0,1-\chi)}{w_\beta + w_\chi} \tag{1.2}$$

and varies from 0 to 1, with high values expected to reveal high pollution concentrations. Indeed, Liu et al. (2002) have computed from scattering models that mixtures of anthropogenic aerosols, typical of Arctic haze events, have lower color ratios than other natural aerosols like sea salt and dust particles, also found in the Arctic. This is related to size distributions, because smaller particles show lower χ values, thus contributing to raise the aerosol index. Weights for the backscattering and color ratio terms were chosen so that $w_\chi = w_\beta$, whereas the backscattering reference value (β_{ref}) varies with height and corresponds to the Arctic mean cloud-free backscattering profile presented in Figure 1.4. Aerosol indices for Antarctic pixels are also computed using the Arctic β_{ref} profile, for comparison against the same reference profile.

The aerosol index fields obtained for the Arctic and Antarctic selected scenes are presented in Figures 1.1d and 1.2d. The part of the TIC-1 layer which is misclassified as cloud-free (Arctic scene, at $\approx$ 9 km, between tick marks $98.0°E$ and $89.1°E$) shows a moderate index. If other parts of this TIC-1 cover are also misclassified as cloud-free, they show a low aerosol index due to a high χ value. The low-level aerosol layer appears with a moderate or high aerosol index. In the Antarctic scene, the highly backscattering PSCs appear only with a moderate index, due to their relatively high color ratio. Some zones around the continental TIC-1 system also exhibit a moderate aerosol index.

1.4. Results

1.4.1. Statistics on clouds

Figures 1.5 and 1.6 show the vertical distribution of the cloud type fractions for Arctic and Antarctic sectors, respectively. The fraction of a cloud type at a given level is calculated by dividing the number of bins for this type by the total number of profiles in the investigated zone (at this level). Results are presented between altitudes of 1 km and 15 km (68 levels). Vertical distributions contain no information on the overlap of cloudy bins, and hence on the "true" cloud fraction, defined as the percentage of sky that is covered with clouds at a single instant (Intrieri et al., 2002), without regard of the height of the cloudy parcels.

In the Arctic, TIC-1 (small crystal mode) are encountered preferentially over Greenland, North Atlantic and Kara Sea (hereinafter GNK) sectors, where they reach a maximum fraction near 0.23 at an altitude of ~ 8-9 km. The Eastern Russia, Beaufort Sea and Canadian Archipelago (hereinafter EBC) sectors are characterized by much lower TIC-1 peak fractions (0.06 to 0.14), also occurring at a lower altitude of ~ 7-8 km. Note, however, that the Eastern Russia sector contains more TIC-1 between 3 km and 6 km than any other sector. Consistently, TIC-2A fractions are higher in the GNK sectors, peaking at ~ 0.13-0.14 between altitudes of 4 and 6 km (indirectly shown in Figure 1.5a). The sum of the TIC-1 and TIC-2A curves suggests that the cyclone frequency is higher in these zones and/or that the convective activity is deeper. This is qualitatively consistent with the winter cyclone frequency climatology calculated by Serreze and Barry (2005) for the period 1970-99, except for Greenland, where orographic lifting presumably contributes to cloud formation with little need from vorticity. Mixed-phase and underlying TIC-2C are also found preferentially in the GNK sectors, with values between 1 and 2 km 3 to 4 times higher over North Atlantic than over EBC sectors (see Figure 1.5b). Figure 1.5c shows that the TIC-2B fractions are highest over Greenland and North Atlantic above 5 km, whereas Beaufort Sea and mostly Eastern Russia sectors have the highest fractions in the lower troposphere. When cloudy bins are summed up indistinctly of their type, vertical distributions (not shown) suggest that the clearest skies have occurred over the Beaufort Sea and Canadian Archipelago during January 2007, a condition which favours efficient longwave radiative cooling from the surface and lower

levels. The Eastern Russian sector presents above-average overall cloudiness in the lower troposphere, because of the TIC-2B contribution. In terms of proportions, TIC-2B are most important for the Beaufort Sea, where they compose more than 50 % of the cloud fraction below 5 km (Figure 1.5d). This proportion is also important for the Eastern Russia and Canadian Archipelago sectors, with more than 40 % in the lower troposphere. GNK sectors present remarkably low TIC-2B proportions in the lower levels.

As shown in Figure 1.6a, Antarctica is relatively similar to the GNK sectors in terms of small ice crystal and underlying TIC-2A vertical distributions. Especially, West Antarctica (Peninsula) has a TIC-1 + TIC-2A distribution very similar to that of Greenland. No Antarctic sector is as poor in TIC-1 + TIC-2A as the EBC sectors. Above an altitude of about 12 km, the contribution of PSCs to the TIC-1 distributions becomes clear, especially for the African portion of East Antarctica. West Antarctica appears markedly less covered by PSCs between 12 and 15 km than the other sectors, and as shown later this is not due to PSCs being flagged as aerosol. Figure 1.6b suggests that mixed-phase and underlying TIC-2C are as frequent over Antarctica as over the Arctic, but because of the height of the plateau, only the Ross Sea and Weddell Sea areas are well represented by the associated curves at low levels, whereas curves for the continental sectors correspond almost exclusively to their margins and the surrounding oceans. This representativeness issue is apparent from the discontinuities in the slope of East Antarctica sector curves 1 km above the average height of the plateau. Concerning TIC-2B, results indicate that they occur in similar fractions over all Antarctic sectors, but are 25 to 30 % less frequent in the lower troposphere over the whole Antarctica than over the whole Arctic, owing to the strong contributions from EBC sectors. Above 6 km, results become similar. The sector-to-sector TIC-2B variability is also lower for Antarctica. In terms of proportions, TIC-2B account for roughly 20 to 35 % of all clouds below 6 km, just like GNK sectors, and contrasting against EBC sectors.

1.4.2. Cloud fraction

From the scene classification, we can calculate the standard cloud fraction, defined as the fraction of profiles containing one or more cloudy bins, regardless of their height. Results are gathered in Table 1.1, in the form of intervals whose limits have been obtained by two different sets of thresholds. For the highest limit, we have used the

results from the baseline algorithm, requiring for a profile that only one pixel be cloudy and using the threshold $\beta_{532\_min} = 0.0009 \ km^{-1}sr^{-1}$, whereas for the lower one, two cloudy bins were required, with a threshold increased to $\beta_{532\_min} = 0.0012 \ km^{-1}sr^{-1}$. For the investigated months, cloud cover estimates over the Arctic (63-76 %) and Antarctica (62-74 %) are similar. There is however variability within these broad regions. The Beaufort Sea (48-65 %) and Canadian Archipelago (49-66 %) sectors present the lowest estimates in the Arctic, whereas North Atlantic (77-86 %) is the cloudiest of the 11 sectors. Over the southern continent, the Ross and Weddell Seas show the highest cloud fraction estimates, followed by West Antarctica, whereas the Australian Side of East Antarctica (47-60 %) presents the lowest cloudiness of the 11 sectors. Unfortunately, these results say nothing about the latitudinal distribution of the cloud cover. Boundary layer (first kilometre above the surface) clouds have not been included, and PSCs above 15 km could increase values for Antarctic sectors, but only slightly since these usually form above other cloud systems. Visual inspection of the ANT-031 scenes below 15 km have clearly revealed PSCs in 29 of them, but no single scene contains PSCs in the ARC-030 subset.

1.4.3. Statistics on aerosol properties

The aerosol index (α) has been designed for emphasizing cloud-free volume bins which exhibit a high β_{532} and/or a low χ value (eq. 1.2), characteristic of small sulphate particles in the nucleation mode, but maybe of other aerosol compounds as well. Mean profiles of α calculated for January 2007 (Figure 1.7a) show that Eastern Russia and the Beaufort Sea have markedly higher aerosol concentrations than the Arctic average in the lower troposphere, whereas North Atlantic and Kara Sea have concentrations lower than the average. In January 2007, the Canadian Archipelago and Greenland are the sectors most representative of the Arctic-wide average in terms of the aerosol index, excepted for Greenland in the lower levels, where only the margins contribute to the statistics.

Using the Northern Aerosol Regional Climate Model (NARCM) (Gong et al., 2003), which explicitly simulates the fields of 5 aerosol species (sea salt, sulphates, black carbon, organic carbon and dust) segregated in 12 size bins, Muñoz-Alpizar et al. (in

preparation) have shown that Eastern Russia and Beaufort Sea were the Arctic sectors in which the sulphate concentrations and the sulphate mass fraction in the total aerosol have been highest during January 2007. This suggests that high values of the aerosol index most likely occurred during sulphate-enriched haze events. Figure 1.7b shows that the threshold $\alpha = 0.6$ in non-cloudy bins is crossed most often over Eastern Russia and the Beaufort Sea. If we use this threshold for isolating haze from clean air, we obtain that for all Arctic sectors haze occurs most frequently between altitudes of 1000 and 1500 meters, and for roughly about 8 to 15 % of all non-cloudy bins. Above 5-6 km, the relative contribution from noisy pixels having a very low color ratio becomes high. The jump at 8.2 km in the curves of Figure 1.7 is an artefact coming from the two-step averaging procedure of the β_{per} and β_{1064} fields, as discussed previously, and bears no physical meaning.

Over Antarctica, the mean aerosol index and haze frequency of occurrence in non-cloudy bins are much lower, and the variability among sectors is small (Figure 1.7c and 7d). Maximal haze occurrence occurs near 1000 meters for all sectors, but this cannot be true over the continental plateau (surface around 3000 m altitude). Peak values of α are 2-3 times lower than over the Arctic. If we rely on the aerosol index as an occurrence criterion for anthropogenic aerosols (small and highly backscattering atmospheric constituents), we may conclude that during July 2007 over Antarctica, air masses were much less polluted than during January 2007 over the Arctic. This difference is due to the intensity and proximity to the Arctic of the Northern Hemisphere anthropogenic sources. The presence of PSCs is also revealed by the α mean profiles, mostly over the African Side of East Antarctica and much less over West Antarctica (Peninsula). However, in most cases, $\alpha = 0.6$ is a threshold too high for capturing PSCs.

1.4.4. Color and depolarization ratios

In this section, we discuss differences between cloud types and haze using scatter plots in the (β_{532} , χ) and (β_{532} , δ) spaces. We used profile bins of the ARC-030 subset below 8.2 km, and cloud-free bins are partitioned into haze and molecular categories, with the requirement that haze satisfy $\alpha \geq 0.6$, corresponding to red zones in Figures 1.1d and 1.2d.

Figure 1.8a shows the distribution of all bins in the (β_{532} , χ) space. Scatter plots are also presented by feature categories. Molecular pixels (not shown individually) appear mostly below $\beta_{532} \approx 0.0020 \ km^{-1}sr^{-1}$, but a significant number of pixels are found above this value, along the $\chi \approx 1$ line, due to very low depolarization ratios which exclude them from the TIC-1 category, and to high color ratio values which subsequently exclude them from the haze category. A greater lidar off-nadir angle during measurements could have resulted in some of these pixels being classified as TIC-1, by avoiding low δ reflections. Haze occupies a small region in the (β_{532} , χ) scatter plot, corresponding to cloud-free pixels having at the same time a high $\beta_{532} / \beta_{ref}$ and a low χ values. High color ratio bins ($\chi > 2$) correspond to either low α cloud-free pixels (molecular) or lidar saturation layers. Bins for which the radar retrieval identifies ice clouds in the low β_{532} / high χ region of the scatter plots correspond to the bottom parts of cloud systems, where the β_{532} field shows important attenuation. The fact that the maxima of occurrence of TIC-2A and TIC-2B bins (above $\beta_{532} \approx 0.0010 \ km^{-1}sr^{-1}$) are found slightly below the $\chi \approx 1$ line is consistent with the high χ values associated to saturated signals, and means that the 1064 nm probing wave penetrates deeper in this kind of clouds. If a perfect retrieval of the volume backscattering fields was performed, these low β_{532} / high χ TIC-2 bins would most probably move towards the TIC-2 maxima of occurrence. A huge fraction of mixed-phase bins are found for $\beta_{532} > 0.0050 \ km^{-1}sr^{-1}$, coarsely in the range $\chi \in [0.6,1.6]$. However, mixed-phase clouds also present a distinct maximum of occurrence near the haze maximum. This suggests that some bins may have been misclassified and that the mixed-phase $b_1 = 0.0015 \ km^{-1}sr^{-1}$ parameter (cut-off) could be increased. This would reclassify pixels at the top of these layers as haze, and those at the base as haze or saturated. This difficulty in clearly establishing the position of the layer top suggests a high sensitivity to the b_1 parameter when calculating any correlation between mixed-phase layer properties and overlying aerosol indicators. In fact, all thresholds used for isolating features, most apparent in TIC-1, haze and mixed-

phase (β_{532}, χ) scatter plots, potentially have a significant effect on statistics and correlations presented in this study. This point is further discussed later.

Figure 1.9 shows the (β_{532}, δ) scatter plots for all bins and for individual feature categories. The high region of occurrence in Figure 1.9a, extending roughly from (0.0001, 0) to (0.0010, 0), includes mainly cloud-free and saturated bins, although some radar-seen bins, which correspond to the saturated zones in the bottom of TIC-2, are also located there. The fact that the perpendicular fraction of the β_{532} returned signal increases as β_{532} shows more and more saturation may possibly indicate that crystals are less horizontally oriented in the bottom layers of TIC-2A. TIC-2A show a broad maximum around (0.0045, 0.25), but TIC-2B extend their maximal zone of occurrence to very low δ values around $\beta_{532} \approx 0.0010 \ km^{-1}sr^{-1}$, coinciding with the haze maximum. Possible explanations are that the radar sees some wet giant particles like sea salt aggregates, or that some radar sampled volumes contain distinct ice crystal and aerosol regions. Departures from lidar and radar measurement collocation and synchronicity may also result in one instrument seeing clouds and the other seeing nearby haze, especially at TIC-2B tops. The fact that TIC-2A (β_{532}, δ) scatter plots do not present the same maximum extension towards small δ values is consistent with higher convective energy, which prevents crystals from horizontally orientating and promotes clustering of ice crystal aggregates. Unlike in the (β_{532}, χ) scatter plots, TIC-2 patterns in (β_{532}, δ) scatter plots show no threshold effect, since the mask for ice water content has been applied on the level 1B radar reflectivity field and not in our algorithm. This cut-off is variable, around -28 or -30 dBZ_e (Mace, 2007). TIC-1 and haze bins show maxima of occurrence very close to each other, at about $\beta_{532} \approx 0.0010 \ km^{-1}sr^{-1}$, and this proximity is due to the small lidar off-nadir angle. Nevertheless, the exclusion of bins identified by the algorithm as molecular and saturated (Figure 1.9b) allows for a resolution of these maxima. High δ bins in the haze distribution present low χ and high α values. Finally, mixed-phase clouds, whose identification is based on β_{532} vertical gradient considerations, preferentially show low δ values. Important departures from zero may be due to ice crystal contributions, and/or multiple scattering effects (Hu, 2007).

1.4.5. Ice effective radius-aerosol index correlation

Calculations of the linear correlation coefficients (LCC) between retrieved r_{ie} values (CloudSat level 2 product) at the top of TIC-2B (3 upper bins) and the aerosol index of layers above (6 bins, TIC-1 excluded) have been performed. Results for the different sectors vary between 0.08 and 0.15, except for East Antarctica sectors which have lower values (see Table 1.1). All r_{ie}-α LCC results have their 95 % confidence interval within ± 0.01, as obtained through Fischer's z-transformation test. Hence, results are significant for all sectors, except over the African side of Antarctica. However, results could be dependant on algorithm parameters. The physical interpretation is discussed below.

1.5. Discussion

1.5.1. Implications for the SIFI effect

Analysis of CALIPSO and CloudSat data sets shows marked and very significant regional differences in the proportion of TIC-2B in the Arctic lower troposphere cloud cover during January 2007 (from ~ 30 % over Kara Sea to ~ 55 % over Beaufort Sea at 4500 m), but much less in the Antarctic cloud cover during July 2007 (between 25 and 35 % at 4500 m). Regional variability is also observed in the lower troposphere frequency of haze occurrence over the Arctic (between 5 and 8 % at 4500 m), but much less over Antarctica (between 3 and 4 % at 4500 m). Moreover, Arctic sectors presenting lower troposphere TIC-2B proportions much higher than the average are the same for which haze occurrence is clearly above average, i.e. Eastern Russia and Beaufort Sea. The Canadian Archipelago also presents a high TIC-2B proportion, but a frequency of haze occurrence close to the Arctic average value. Other Arctic sectors and all Antarctic sectors present much lower (background) aerosol index values in the lower troposphere. An important question raised by the finding that TIC-2B proportions and outside-cloud pollution levels are high in the same sectors is whether haze aerosols are also found in great amount within TIC-2B systems. Short of in situ measurements for aerosol composition in TIC-2B, we performed numerical simulations with NARCM (Gong et al., 2003) for assessing the concentration, size distribution and acid fraction of the Arctic aerosol during January 2007 (Muñoz-Alpizar et al., in preparation). Results confirm the

vertical mixing of aerosols within TIC-2B systems for the particular event shown in Figure 1.1, and also on average during the month. The model further provides an assessment of the sulphate ratio to around 65 % for aerosols inside the TIC-2B system in Figure 1.1, and sulphate domination in the aerosol during most of the month over the High Arctic.

The co-occurrence of two phenomena does not a priori imply a causal relationship between them. In the present case, the location of the SO_2 sources combined with the polar circulation can explain high sulphate concentrations in the Eastern Russia sector and eastward. Also, the absence of orographic obstacles and the presence of an ice cover (insulating from oceanic sensible and latent heat sources) limits the vertical extent of clouds in the same sectors. Nevertheless, we believe that all conditions are present for a physico-chemical action of the anthropogenic aerosol, which tends to increase the ice effective radius in TIC-2B systems. We already argued that when weak cold low pressure systems drift over the cold Arctic, thus slowly raising moisture and pollution from the boundary layer well into the mid-troposphere, the SIFI may have an impact because ice supersaturation production rates remain low, so that nucleation takes place only on larger IFN. In this context, sulphuric acid (and to a lower extent ammonium sulphate) could act as a second obstacle to the onset of freezing, further limiting the competition for water vapour and allowing for the formation of larger ice particles, as in TIC-2B type. The SIFI may also be effective when active cyclones characterized by a strong vertical velocity lift air parcels at higher altitudes, but to a lower extent. Indeed, the SIFI effect in TIC-1 fails most of the time in producing explosive growth of crystals and light precipitation, as suggested by the recurrent inability of the radar to see the small ice crystals in the upper part of the troposphere.

The size discrimination for aerosol water uptake is always expected through Kelvin effect in the Köhler equation, but it is much enhanced when particles are coated with frost-inhibiting material like sulphuric acid. Eventually, acidic haze droplets can freeze, but only when sulphuric acid shell on IFN is diluted enough to allow for it. Most likely, under these conditions, the largest and most diluted haze droplets can freeze, while small droplets (at the same supersaturation) remain too acidic for freezing, thus limiting the ice crystal number concentration. If this SIFI is effective as we think, high concentrations of sulphuric acid (pollution) at the top of TIC-2B should come with large

sizes of the ice crystals. This is in our opinion what the significant positive linear correlation coefficients (LCCs) between r_{ie} and α reveal. However, α used in the calculation does not characterize top-cloud bins, but rather bins sampled within 1.5 km above cloud tops. This methodological limitation (we do not have access to the interstitial aerosol) introduces many pairs of (r_{ie}, α) values in the calculation which reduce the LCC values. Indeed, due to the very frequent Arctic temperature inversions (Serreze, Kahl and Schnell, 1992), extended aerosol layers often follow isentropic surfaces and exhibit a flat top characterized by a high vertical gradient in their concentration. Generally, cloud tops form close to aerosol layer tops, when cooling either due to adiabatic vertical motion or imbalance in the radiative budget occurs. It may happen that most IFN are not activated (if ice supersaturation remains low), in which cases we have a discernable aerosol layer exceeding the cloud top (edges), so that the index (α) may correlate positively with nearby cloud top r_{ie}. However, in many cases, when a cloud cover forms by encompassing the whole (denser) aerosol layer, aerosol concentrations just above the cloud top may not be representative of the interstitial aerosol concentrations. So, the LCC values presented in this study should be interpreted as lower limits for the "true" LCCs that exist between r_{ie} and the pollution concentrations at the top of TIC-2B covers. Extensive aircraft campaigns dedicated to the measurement of interstitial aerosol properties and ice crystal sizes would be needed for assessing the true LCCs.

In sum, when comparing EBC sectors to the other Arctic sectors and to the remote Antarctic plateau, the results appear to us as a reasonable indication that high pollution concentrations favour big ice crystal populations in shallow convective systems (TIC-2B, topping in the lower troposphere) during polar nights. Subsequent effects on climate could be highest in Eastern Russia and Beaufort Sea sectors, and to a lesser extent over the Canadian Archipelago, because TIC-2B systems account for the highest proportions in the total cloud cover, and haze events are also most frequent there. Explicit numerical simulations of aerosols and clouds in some of the Arctic TIC-2B systems observed by CloudSat and CALIPSO would be useful to better understand this link. In particular, it would be interesting to evaluate if the SIFI effect can not only favour larger crystal sizes in TIC-2B systems, but even favour their formation, at the expense of TIC-1/2A covers. This is probably the case, since the distinction between them comes only from an arbitrary threshold fixed by the radar sensitivity (corresponding to 28-30 μm), and there is indeed a continuum of cases between pure TIC-2B and pure TIC-1/2A

systems. The proportion of TIC-2B systems which would have developed into TIC-1/2A without the SIFI effect could in principle be estimated from the (r_{ie}, α) series used for LCC calculations and an adequate relationship linking $\Delta\alpha$ (initial change in α) to Δr_{ie} (consequent change in r_{ie}).

1.5.2. Implications for the DGF mechanism

The consequences of the SIFI effect, which is in this paper not directly demonstrated but rather presented as consistent with our results, are potentially important. One direct impact could be the alteration of the radiative properties of TICs, by increasing the size of ice crystals and spreading their vertical distribution over a deep height interval, as seen in TIC-2B cases. The resulting effect would increase the atmospheric infrared cooling rate over most of the layer. On the opposite, an elevated TIC-1 warms the lower atmosphere and the surface by enhancing downward atmospheric radiation. Since TICs have a long atmospheric residence time, corresponding to the low pressure systems lifetime (5-10 days), and act on very large horizontal scales (thousands of kilometres, see Figures 1.1 and 1.2), their direct effect on the radiation balance is likely to be very significant on the net heat balance of the Arctic during winter.

Another important effect of TIC-2B and 2C types arises from the alteration of the water vapour balance associated with light precipitation, which leads to the DGF process. This effect becomes increasingly important at temperatures below $-30°C$, for which the peak of the Planck function shifts towards the far IR and the water vapour transmittance above 17 μm increases, opening the "dirty window" in the H_2O rotation band. Under these conditions, the atmospheric dehydration in TIC-2B systems may enhance the radiative cooling in the lower atmosphere, feeding back into dehydration to accelerate the air mass transformation. Girard, Blanchet and Dubois (2005) have already investigated the DGF effect in the boundary layer, and hypothesized that this could cause a surface cooling anomaly through a feedback between the diamond dust formation (TIC-2C), the water vapour greenhouse effect and cooling propagating from the surface. It is not clear at the moment if the SIFI effect can trigger such a feedback in the free lower troposphere, but new findings in this study point at a possible extension of the DGF well into the mid-troposphere, with dehydration associated to TIC-2B and to acid coating on aerosols. The

cooling of elevated layers greatly favours the generation of available potential energy (APE) and feeds directly in the formation of intense winter storms. It is another path for altering the atmospheric circulation at large scales.

1.5.3. Algorithm limitations and uncertainties

Classifying remotely sensed atmospheric features is not a straightforward task, since no comprehensive method totally supported by theoretical considerations exists. From the active remote sensing to the establishment of cloud types and aerosol vertical distributions, manipulation of the information is necessary at many steps. Therefore, one must assess at which extent the final products describe the true state of the polar atmospheric systems during the months investigated. Distortion of the information potentially occurs via a) uncertainties in the lidar fields used, b) assumptions in the radar ice water content retrieval, c) attenuation of the lidar beam, d) spatial and temporal mismatch in satellites orbits, e) averaging processes, f) feature classification algorithm assumptions and thresholds, and g) statistical representativeness of the sampling. In this section, we discuss the nature of these uncertainty sources, and how we can cope with them.

Uncertainties in the input data, due to systems technical limitations and which also encompass the retrieval algorithm assumptions in the case of the radar, could possibly modulate our main conclusions. Using noise scale factor considerations (Liu et al., 2006), we estimated a geometric average random error on β_{532} increasing from about 19 % near the surface to 29 % at 8000 meters for the Arctic selected scene (after degradation at the CloudSat resolution). Excluding bins with values lower than $\beta_{532\_min} = 0.0009 \quad km^{-1}sr^{-1}$ reduces the error between about 6 and 9 %. The uncertainty on the r_{ie} retrieval is estimated at about 20 % in the CloudSat product. A good way to assess the impact of input field uncertainties would be to make a random change of all values within their uncertainty range before performing the analysis. By repeating this operation many times, we could conclude about the robustness of our findings to input uncertainties.

For our baseline algorithm, we treated attenuated input fields, and we defend the choice of not having performed a retrieval of the volume (intrinsic) backscattering by the fact that this operation requires the introduction of information which is not supported by measurements. The high variability of aerosol and water content mixtures filling sampled volumes renders arbitrary any choice for a set of optical coefficients (extinction-to-backscatter ratio, asymmetry factor, etc.) used when retrieving a volume backscattering profile from an attenuated profile. Also, there is no guarantee that performing a retrieval of the volume backscattering prior to classifying bins would lead to more realistic results, since the choice of the multiple feature segregation thresholds would be done by considering slightly modified input scenes, so that values would be different, but still partly tuned following visual appreciation of the results produced by the algorithm. The final edges of cloud and aerosol features would possibly stay at the same place or vary only a little most of the time. A comparison of the two methods should be performed before concluding if a significant difference would be found in main conclusions, and if it were the case, only vast in situ measurement campaigns could tell if the retrieval leads to classification results closer to the reality or not.

For the previously selected Arctic and Antarctic scenes, the average distance between each lidar and the closest radar sampling locations were respectively 305 and 301 meters. Measurements also suffered a time lag of 10-15 seconds. During that period, 50 m/s winds would displace an air parcel by 500-750 meters, and a 10 m/s vertical movement of water particles would translate them by 100-150 meters. Considering the radar 1.4 x 2.5 km footprint and the vertical resolution of 240 meters, we think the lidar is sampling a volume comprised in the radar sampled one most of the time. Also, because of the large extension of the TIC-1 and haze layers (high profile-to-profile autocorrelation), we believe orbital mismatches do not significantly affect our conclusions.

Averaging of neighbouring profiles for avoiding too small signal-to-noise ratios or for comparing to the lower resolution radar field mixes information from different volumes, and this operation may lead to feature misclassification, especially at the edge of cloud systems and near the surface. However, we see no a priori reason to think that cloud type proportions could be systematically biased.

All results presented in this paper have been obtained from the same baseline algorithm, but variation of some parameters could possibly significantly alter them. In particular, the sensitivity to the shape and parameters of the δ_{min} function, as well as to the χ_{min} and β_{532_min} values, which together determine the segregation between TIC-1 and cloud-free bins, should be further investigated. Variations to the shape of the aerosol index function, based on β_{532} and χ values, should also be performed. In addition, haze occurrence based on our cut-off at $\alpha = 0.6$ should be compared to Arctic haze detection results based on the more conventional aerosol optical depth (Yamanouchi et al., 2005). We recognize also that several assumptions present some degree of arbitrariness, for example the method for isolating TIC-2B systems, especially when there is a gap between the radar-seen and the TIC-1 layers. Corrections could be performed for certain cloud configurations, but there will always be special cases that such an algorithm will misclassify.

Due to the great number of profiles used for this study, all differences we have emphasized are statistically significant. However, 95 % confidence intervals have not been shown in figures, for clarity purpose. Figure 1.10 presents the vertical distribution of TIC-2B proportions (1.10a) and haze fraction of cloud-free bins (1.10b), with the standard deviations and 95 % confidence intervals. For these graphs, we considered the average value for each overpass as one sampling, so that the confidence interval calculation assumes that series have 386 (Arctic) and 379 (Antarctica) values, which are weighted by the number of profiles in the scene for the averages and standard deviations calculations.

Despite limitations mentioned above, we believe our baseline algorithm allows for a reasonable characterization of the polar thin ice cloud and aerosol fields, as well as for meaningful conclusions. At the same time, these limitations imply that findings remain hypothetical, and that more research is needed to support them.

1.5.4. Further investigation

Further work includes improvement of our algorithm. This could be done by considering other TIC-1/cloud-free segregation criteria, like the layer stability and

relative humidity over ice, as used notably by Ishii et al. (1999). The algorithm could possibly take advantage of the characteristically low depolarization ratio of water droplets when identifying mixed-phase clouds, especially when treating next version of CALIPSO data taken with a larger off-nadir angle. For example, Intrieri et al. (2002) used a cut-off of $\delta = 0.11$ for discriminating ice from liquid water content. Hu (2007) also developed a methodology for the identification of mixed-phase layers. Moreover, two-dimensional structure recognition of features could be further exploited, particularly for separating TIC-2A and TIC-2B. As mentioned previously, results sensitivity to algorithm key parameters must also be assessed.

Next, our study should be extended to other winter months, for an understanding of the seasonal and inter-annual variation of the TIC-2B proportions and r_{ie}-α correlations. The relationships between TIC types and synoptic conditions should also be further investigated.

Finally, our main atmospheric inferences, especially the correlation we emphasized between the sulphate concentrations and the effective radius of ice crystals, need more support from numerical simulations of the aerosol field and its interactions with the hydrological cycle.

1.6. Conclusion

CALIPSO lidar and CloudSat radar data sets allow for a characterization of polar winter thin ice clouds and aerosols, aiming to find a relationship between high levels of pollution and the effective radius of ice particles at the top of a certain type of clouds (TIC-2B). Sampled volume bins from 386 Arctic (January 2007) and 379 Antarctic (July 2007) overpasses have been classified using an algorithm based on the CloudSat retrieved ice effective radius (r_{ie}) and the CALIPSO backscattering at 532 nm (total and perpendicular polarization) and 1064 nm (total). Thin ice clouds of type 1 (TIC-1), seen by the lidar only because of the too small size of the ice crystals (< 28-30 μm), occur preferentially in the upper troposphere, and at a much higher frequency over Antarctica and Greenland-North Atlantic-Kara Sea (GNK) sectors than over Eastern Russia-Beaufort Sea-Canadian Archipelago (EBC) sectors. This difference is partly due to the absence of a high plateau (orographic lifting) and/or open-water surfaces (sensible and latent energy

fluxes) over EBC sectors. TIC-2B, a radar-seen (big crystal mode) cloud type, accounts for more than 40 % of the lower tropospheric clouds only over EBC sectors. The Eastern Russia and Beaufort Sea sectors also present the highest aerosol index and the highest frequency of haze occurrence. We argued that in slowly lifting TIC-2B systems, where only coarse IFN may be activated, sulphuric acid brought into the Arctic through haze events may coat and further deactivate a considerable proportion of them, favouring cloud populations made of fewer but larger ice crystals. The small but statistically significant positive linear correlation coefficients between TIC-2B top r_{ie} and the above-cloud aerosol index found in 10 of the 11 sectors support this hypothesis.

Further work includes a study of the sensitivity of results to algorithm parameters and assumptions, the extension of the statistical calculations to other winter months, and the improvement of the baseline classification algorithm.

Acknowledgement

PG acknowledges the Ouranos Consortium and the National Sciences and Engineering Research Council of Canada (NSERC) for financial support, as well as his Ph.D. supervision committee: Jean-Pierre Blanchet, Colin Jones, Éric Girard and Graeme Stephens. The funding for this research was also supported by the NSERC through its International Polar Year 2007-2008 program. We also acknowledge the NASA Langley Research Center / Atmospheric Science Data Center from which CALIPSO data were obtained, and the NASA CloudSat project. Thanks finally to the 3 anonymous reviewers for their valuable remarks.

Figures

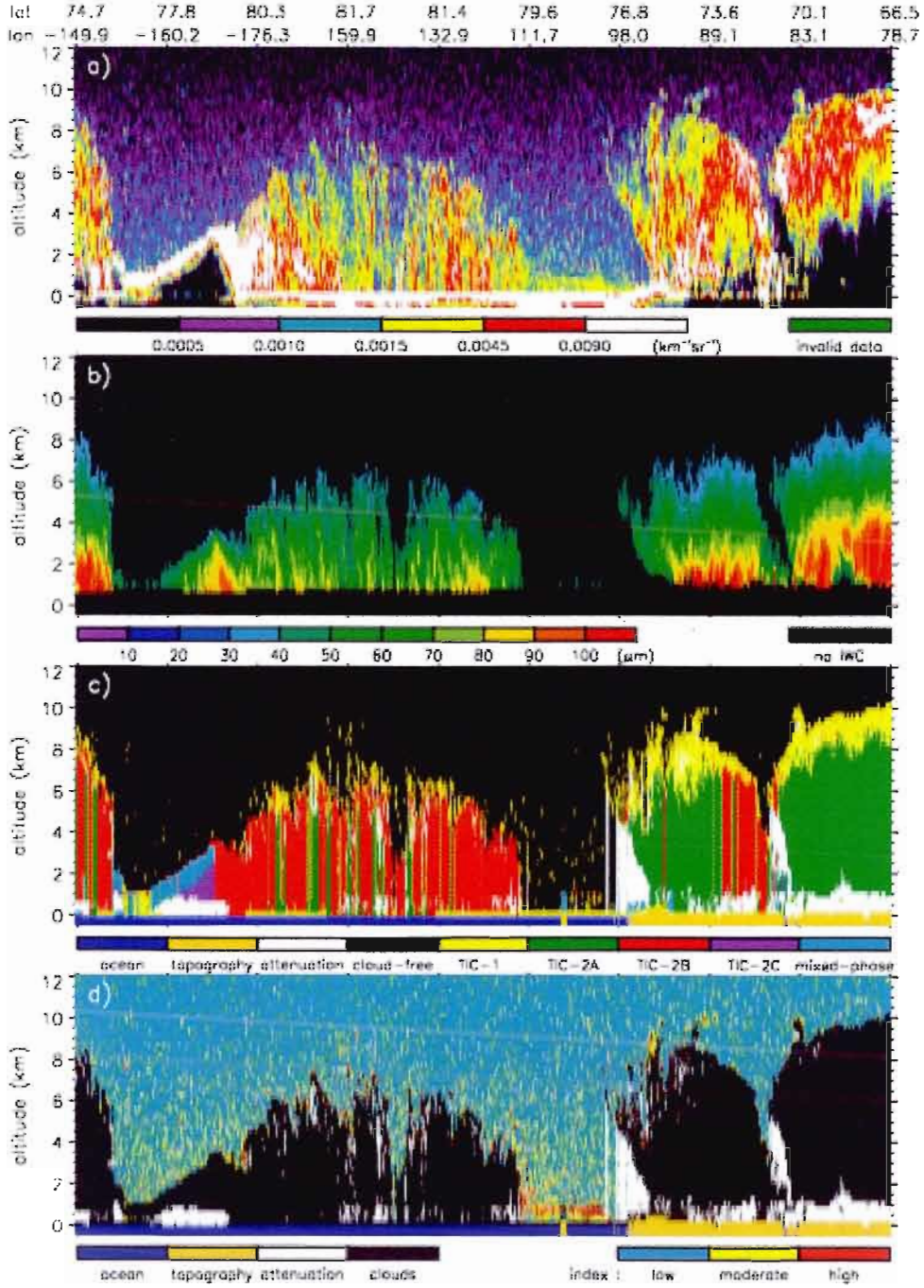

Figure 1.1: Fields from the selected Arctic scene. a) measured β_{532} (CAL-LID-L1-Prov-V1-11.2007-01-19T21-36-47ZN), b) retrieved r_{ie} (2007019202553-03881-CS-2B-CWC-RO-GRANULE-P-R04-E02 ; black means r_{ie} is undefined), c) cloud classification (data in first kilometre above the surface are invalid, but some bin flags have been filled by extrapolating the above feature, for presentation purpose only), d) aerosol index (low: $\alpha \in [0,0.4[$, moderate: $\alpha \in [0.4,0.6[$, high: $\alpha \in [0.6,1]$).

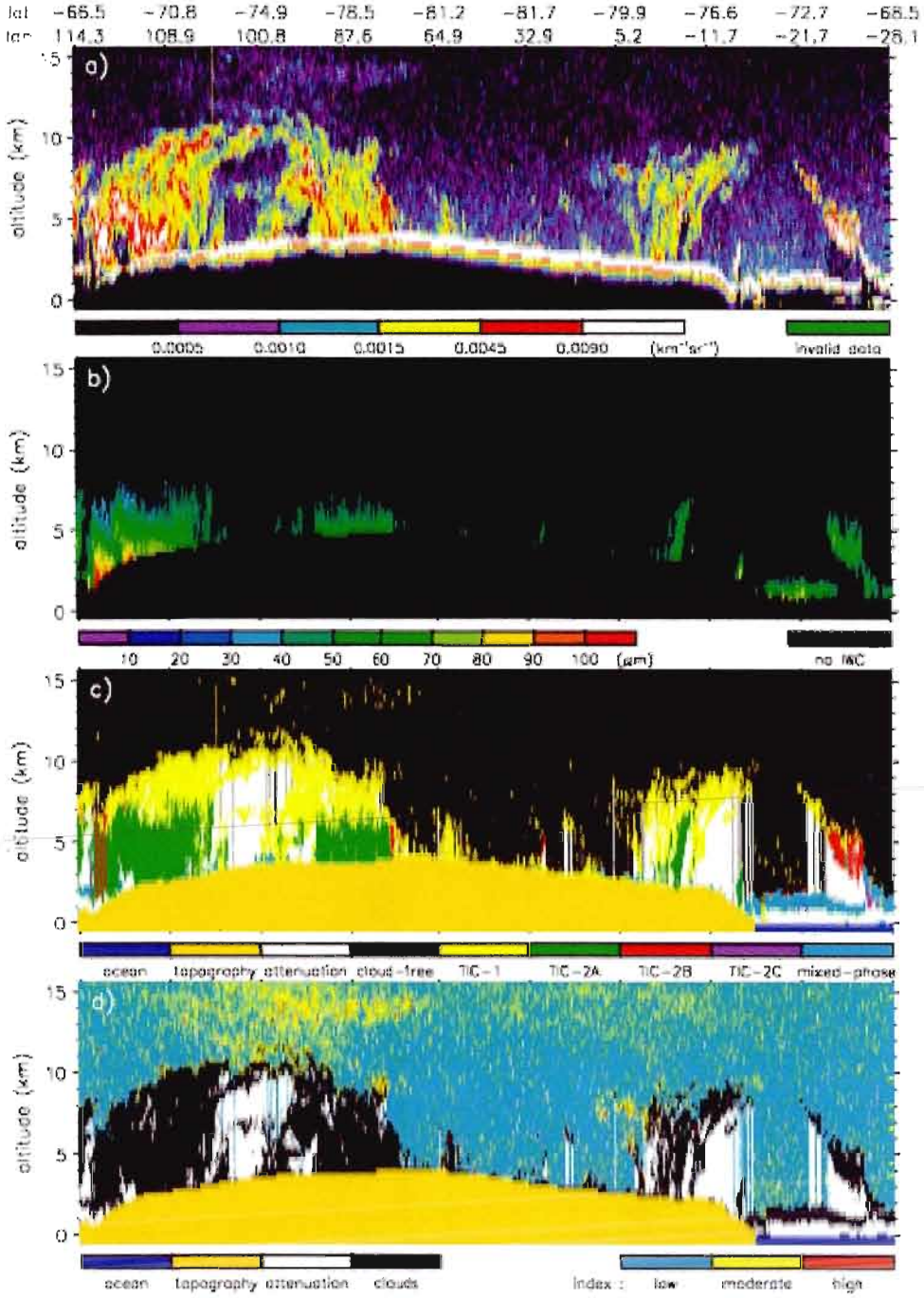

Figure 1.2: Fields from the selected Antarctic scene. a) measured β_{532} (CAL-LID-L1-Prov-V1-20.2007-07-20T16-15-02ZN), b) retrieved r_{ic} (2007201163104-06529-CS-2B-CWC-RO-GRANULE-P-R04-E02 ; black means r_{ie} is undefined), c) cloud classification (data in first kilometre above the surface are invalid, but some bin flags have been filled by extrapolating the above feature, for presentation purpose only), d) aerosol index (low: $\alpha \in [0,0.4[$, moderate: $\alpha \in [0.4,0.6[$, high: $\alpha \in [0.6,1]$).

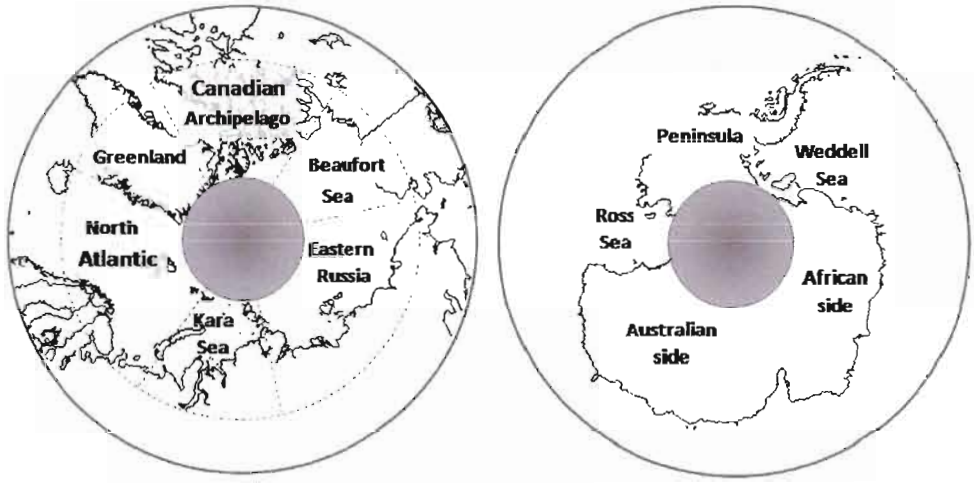

Figure 1.3: Sectors under investigation for January 2007 (Arctic) and July 2007 (Antarctica).

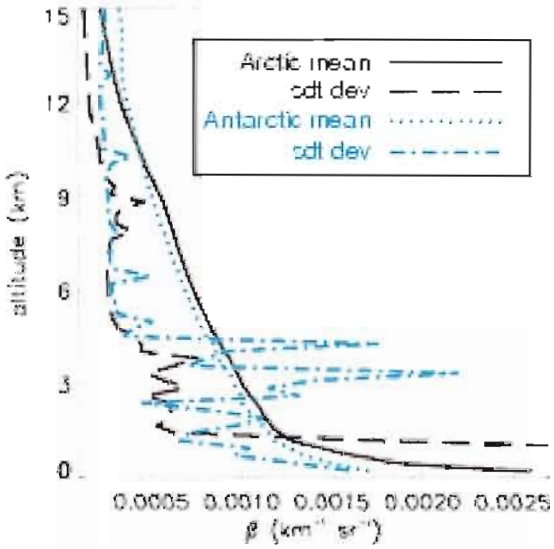

Figure 1.4: Mean cloud-free β_{532} profiles for the ARC-030 and ANT-031 subsets, with standard deviations.

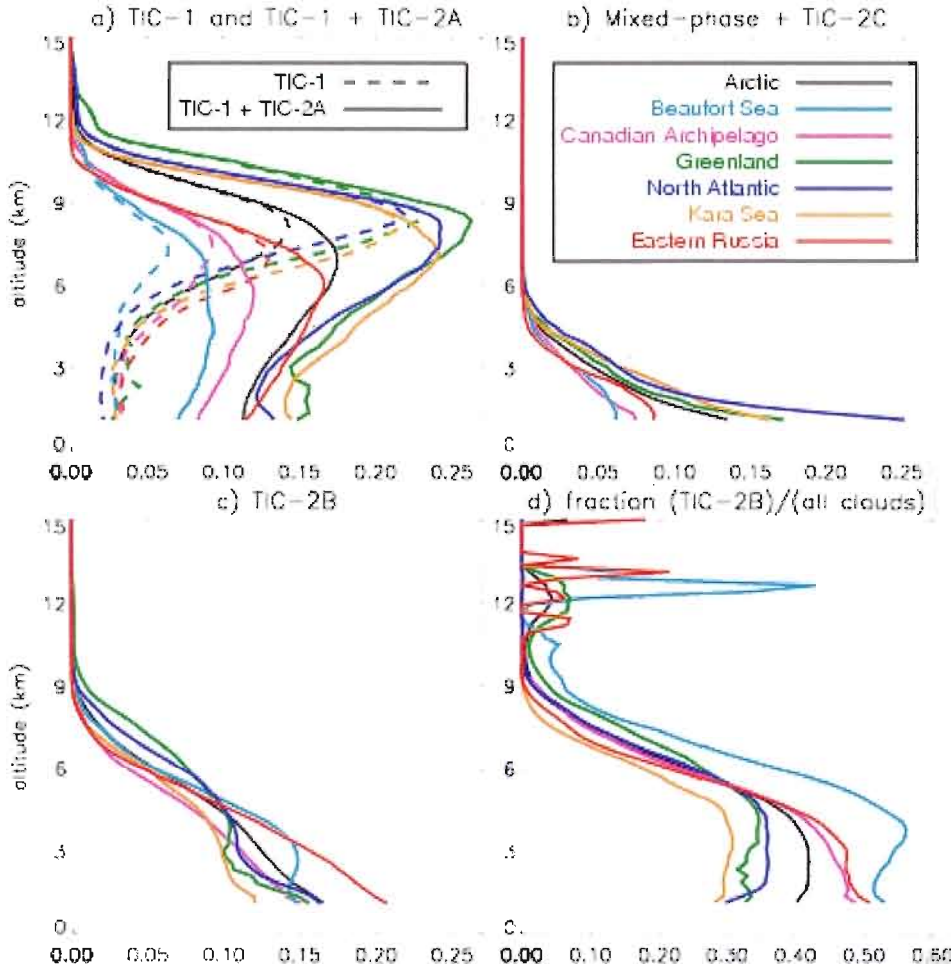

Figure 1.5: Vertical distribution of cloud fractions for Arctic sectors (see geographical delimitations in Table 1.1). Curves in a), c) and d) follow the same color code as in b).

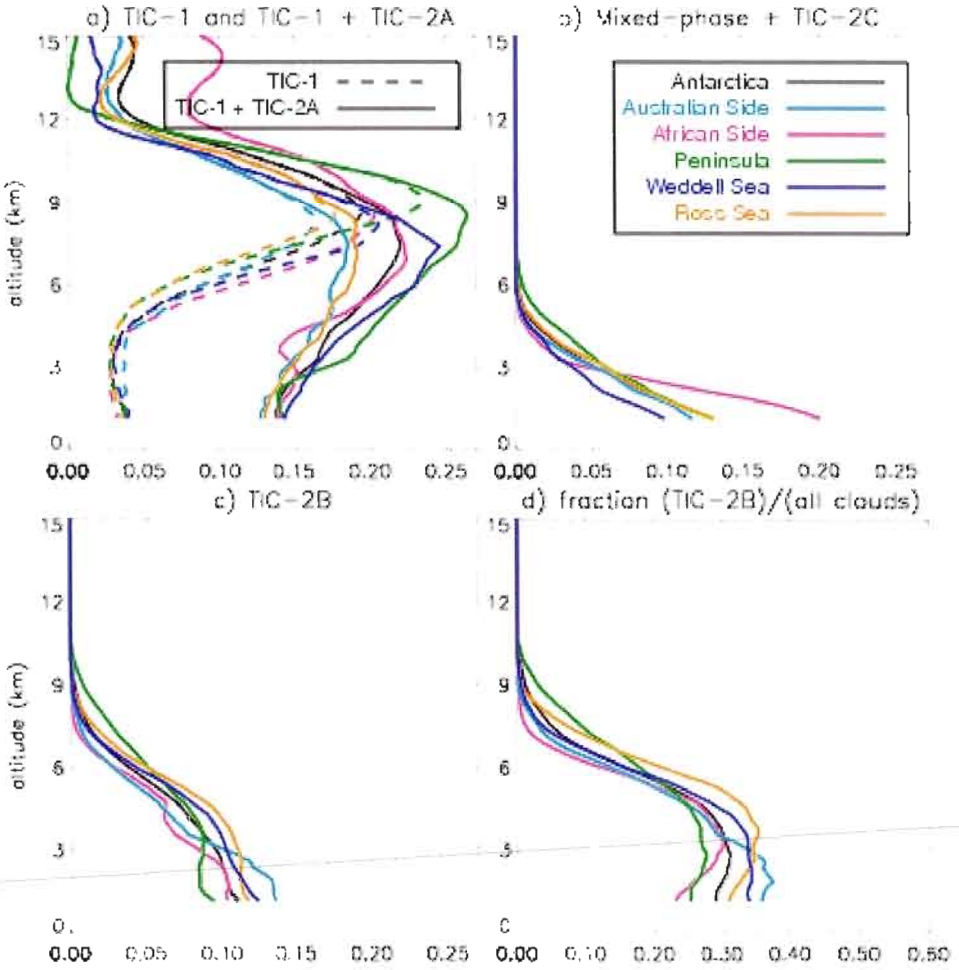

Figure 1.6: Vertical distribution of cloud fractions for Antarctic sectors (see geographical delimitations in Table 1.1). Curves in a), c) and d) follow the same color code as in b).

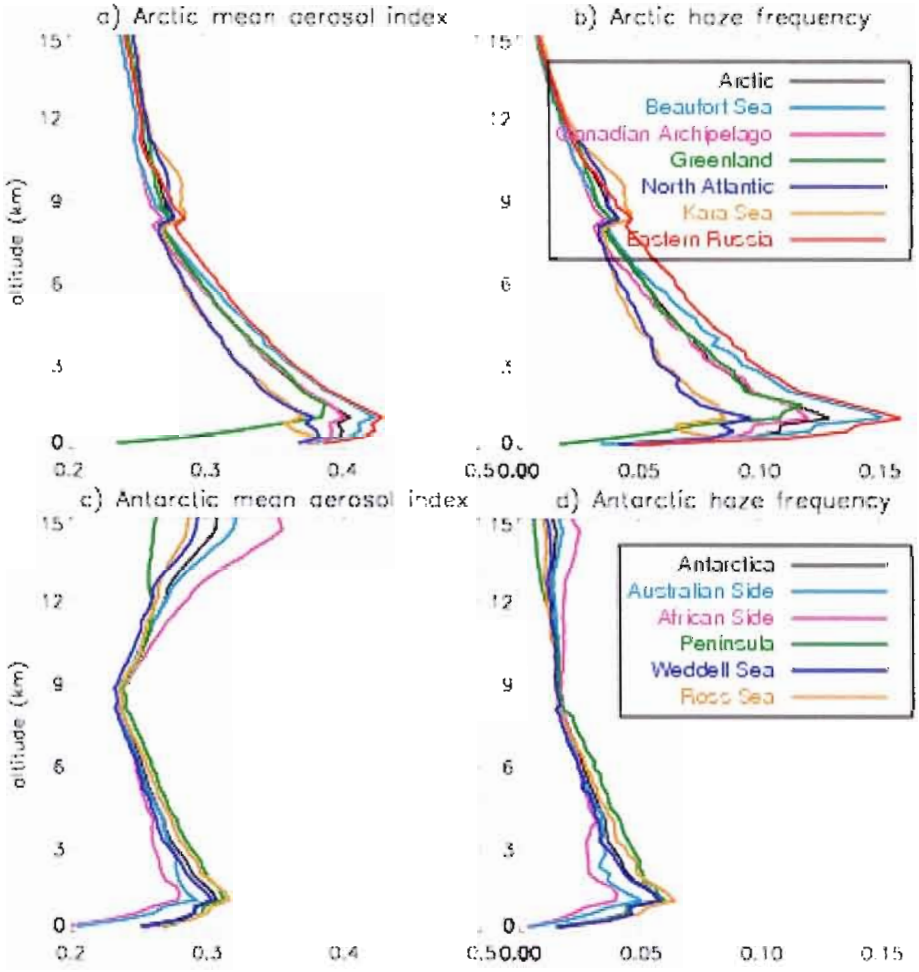

Figure 1.7: Vertical distribution of the Arctic a) aerosol index fraction and b) haze occurrence in cloud-free bins. Equivalent curves for the Antarctic c) aerosol index fraction and d) haze occurrence. Curves in a) follow the same color code as in b), whereas curves in c) follow the same color code as in d).

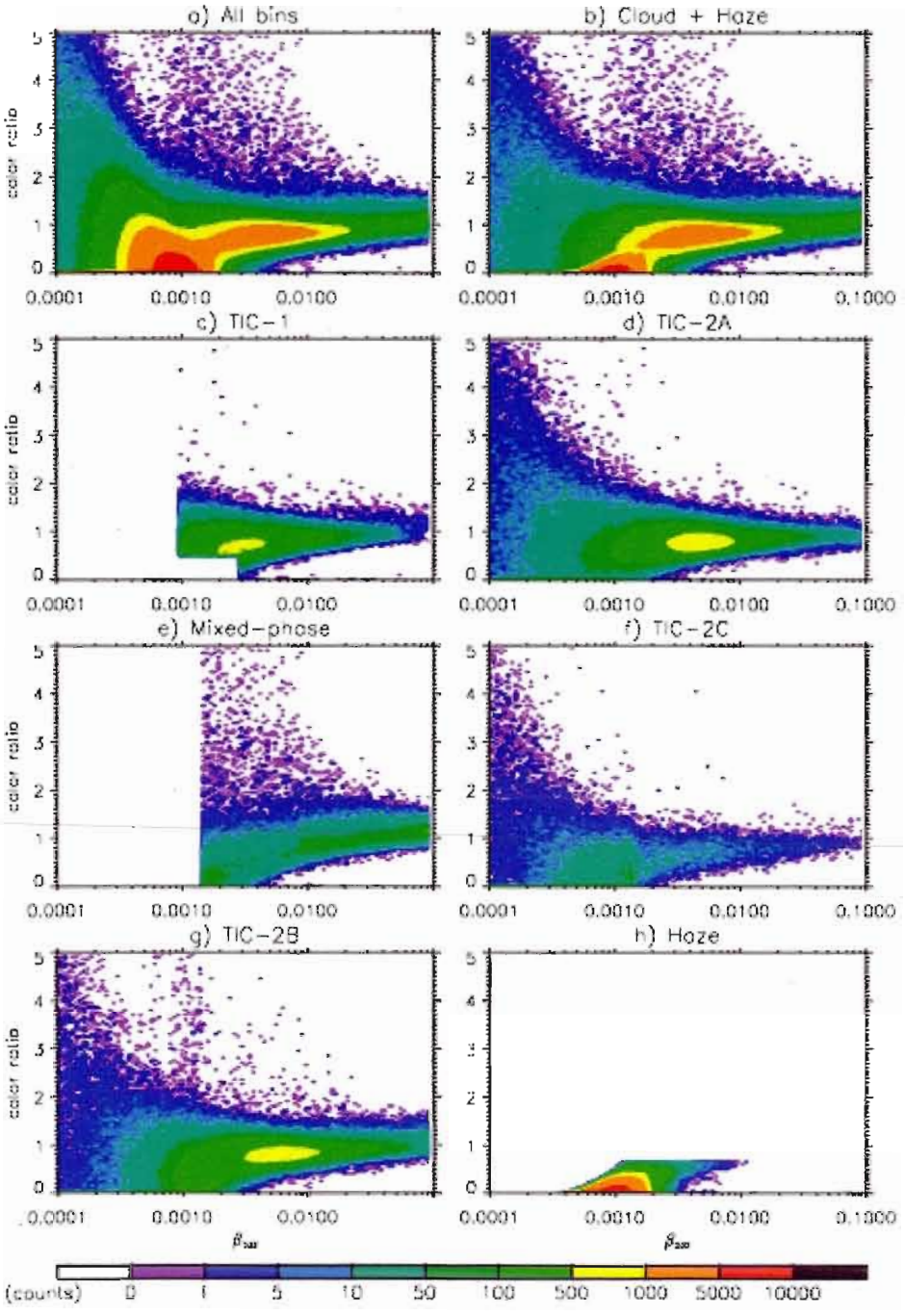

Figure 1.8: Scatter plots in the (β_{532} , χ) space, for a) all bins below 8.2 km of the ARC-030 subset, b) cloud and haze, c) TIC-1, d) TIC-2A, e) mixed-phase, f) TIC-2C, g) TIC-2B and h) haze bins.

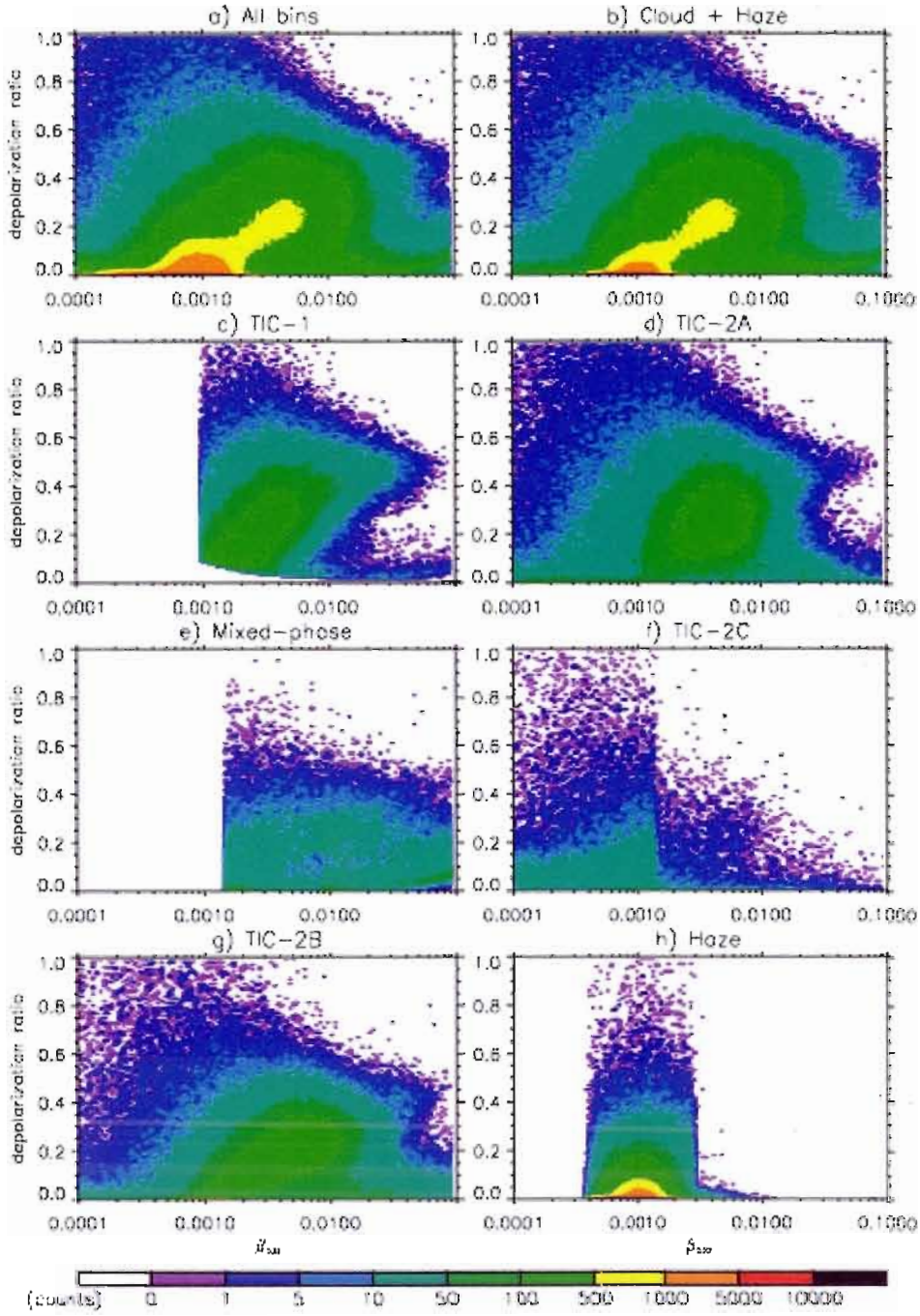

Figure 1.9: Scatter plots in the (β_{532} , δ) space, for a) all bins below 8.2 km of the ARC-030 subset, b) cloud and haze, c) TIC-1, d) TIC-2A, e) mixed-phase, f) TIC-2C, g) TIC-2B and h) haze bins.

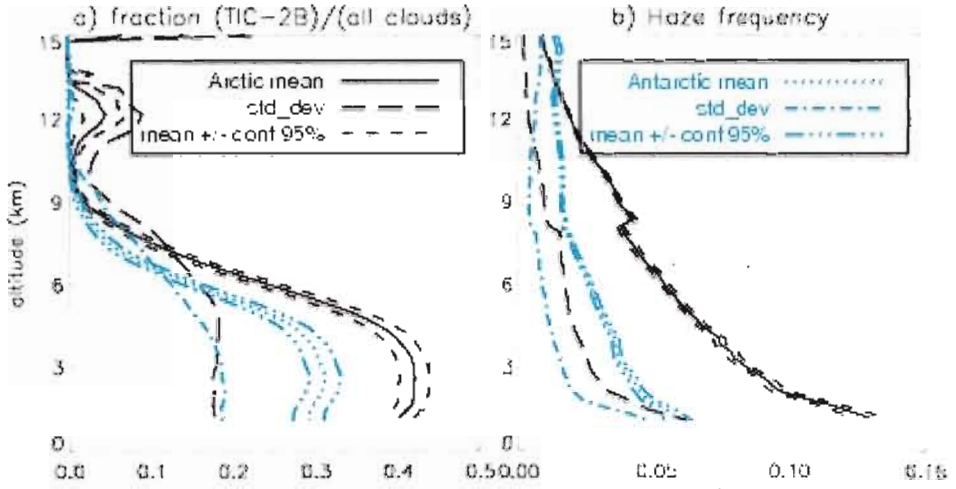

Figure 1.10: Standard deviations and 95 % confidence intervals around the mean for the Arctic and Antarctic a) fraction of TIC-2B in the cloud populations and b) haze frequency.

Tables

Table 1.1: Geographical delimitations of investigated sectors, with the number of profiles used for the study, an estimation of the average cloud fractions (free atmosphere below 15 km) and the linear correlation coefficient (LCC) between TIC-2B cloud top r_{ie} and the above aerosol index (α). The margin of confidence (95%) in the last column (r_{ie}- α) is within ± 0.01.

Sector	Delimitations	Profiles	Cloud fraction (%)	r_{ie}- α LCC
Arctic (January 2007)	66.5°N – 82°N	1 417 289	63-76	0.11
Beaufort Sea	170°W – 125°W	175 572	48-65	0.13
Canadian Archipelago	125°W – 60°W	249 528	49-66	0.15
Greenland	60°W – 20°W	157 371	67-76	0.09
North Atlantic	20°W – 55°E	297 906	77-86	0.12
Kara Sea	55°E – 100°E	179 804	68-81	0.09
Eastern Russia	100°E – 170°W	357 108	64-77	0.10
Antarctica (July 2007)	66.5°S – 82°S	1 673 900	62-74	0.07
Peninsula	150°W – 60°W	409 203	68-81	0.08
Weddell Sea	60°W – 20°W	186 865	68-83	0.14
African side	20°W – 75°E	453 417	62-74	0.00
Australian side	75°E – 165°E	418 462	47-60	0.03
Ross Sea	165°E – 150°W	205 953	70-84	0.14

CHAPITRE II

INVESTIGATION OF THE SULPHATE-INDUCED FREEZING INHIBITION (SIFI) EFFECT FROM CLOUDSAT AND CALIPSO MEASUREMENTS

Patrick Grenier* and Jean-Pierre Blanchet

Institut des Sciences de l'Environnement, Université du Québec à Montréal

*corresponding author: grenier@sca.uqam.ca

Revised for publication in *Journal of Geophysical Review*.
Hereinafter: Grenier and Blanchet (2010a).

Abstract

The hypothesis according to which higher sulphate concentrations favour ice clouds made of larger ice crystals is tested using data sets from the CloudSat and CALIPSO satellites. This is a potential consequence from the sulphate-induced freezing inhibition (SIFI) effect, namely the hypothesis that sulphates contribute to inhibit the onset of ice crystal formation by deactivating ice forming nuclei during Arctic winter. A simple index based on the backscattering at 532 nm and the color ratio from the CALIPSO lidar measurements is compared against in situ sulphate concentration time series and used as a proxy for this variable. An algorithm using the lidar data and the CloudSat radar microphysical retrievals is also developed for identifying cloud types, focusing on those supposedly favoured by the SIFI effect. The analysis includes the effect of the lidar off-nadir angle on the sulphate index and the cloud classification, the validation of the index, as well as the production of circum-Arctic maps of the sulphate index and of the SIFI-favoured clouds fraction. The increase of the lidar off-nadir angle is shown to cause an increase in the measured depolarization ratio, and hence in the ability to detect ice crystals. The index correlates positively with both sulphates and sea salt concentrations, with a Pearson correlation coefficient ($\sqrt{R^2}$) varying from 0.10 to 0.42 for the different comparisons performed. Ultimate findings are the results of two correlation tests of the SIFI effect, which allow for a new outlook on its possible role in the Arctic troposphere during winter.

2.1. Introduction

Haze in the Arctic occurs frequently and since a long time, with summer events reported by early explorers like Fridtjof Nansen in 1882 and Adolf Erik Nordenskiöld in 1883 (Garrett and Verzella, 2008). The nature and origins of these events are however confidently known only since the 1970s. Arctic haze, mainly a winter and early spring phenomenon, varies in composition, and consists of a mixture of sulphates (compounds comprising the SO_4^{2-} ion) and particulate organic matter, accompanied by smaller mass amounts of ammonium, nitrate, black carbon, dust and other trace constituents (Law and Stohl, 2007). Black carbon may also be a dominant species during certain events (Hara et al., 2003), and the degree of its internal mixing with sulphates increases as the haze ages, as for other compounds. Arctic haze is generally considered to be pollution, since it originates mainly from lower latitude human activities. Other sources may be volcanoes (releasing sulphate precursor SO_2) and oceanic biota (producing sulphate precursor DMS). Due to geographic considerations and the winter atmospheric circulation, as well as to their high level of industrialization, Europe and Russia represent the major contributors to the Arctic haze, as inferred from numerical simulations of air pollution transport (Christensen, 1997), chemical analysis of trace constituents (Rahn, 1981) and vertical extension of haze events (Carlson, 1981). Outside of the concentrated haze patches swept throughout the lower troposphere, a background anthropogenic aerosol exists which extends relatively high into the troposphere. It results from incomplete scavenging by the water content as cyclonic systems pump up aerosols and moisture from lower levels. Unevenly distributed pollution and natural aerosols (e.g. sea salt and mineral dust) constitute the substrate for water condensation and ice nucleation. Hence, they partially determine microphysical properties of the cloud field, in a manner far from being fully understood.

The role of sulphates for the Arctic microphysics may be considered crucial, for at least three reasons. First, sulphates represent the major Arctic aerosol species in terms of mass and relative abundance. For example, of the 18 aerosol constituents studied by Sirois and Barrie (1999) between 1980 and 1995, SO_4^{2-} ions alone represent about 50-55 % of the mass in January. Also, sulphuric acid covers about 80 % of the insoluble particles, as observed by Bigg (1980) at Barrow, Alaska, and this percentage could be a lower limit (Blanchet and List, 1983). During the ASTAR 2000 campaign over the

Svalbard area, Hara et al. (2003) also observed that sulphates were the dominant aerosol in terms of relative abundance in particles, under haze as well as background conditions. Our knowledge of the pan-Arctic instantaneous sulphate field (concentrations, proportion of total aerosol mass, internal/external mixing, etc.) is limited. The most reliable information is obtained by local in situ measurements, either during short duration field campaigns (e.g.: ASTAR, AGASP) or at a few permanent stations (e.g.: Zeppelin, Alert, Barrow). An alternative way to obtain information about the sulphate field is to numerically simulate transport of sulphur from its emission to its removal points (Christensen, 1997). However, many assumptions must then be introduced. Thus far, no retrieval technique has permitted to isolate sulphate particles from other aerosols and to give their concentration from satellite measurements.

Secondly, the hydrophilic character of the major sulphate compounds renders them especially effective as cloud condensation nucleus/nuclei (CCN). Indeed, H_2SO_4 particles (sulphuric acid) are hygroscopic, i.e. they grow by absorbing water vapour at any relative humidity with respect to water (RH_w) (Andreae, Hegg and Baltensperger, 2008), so that H_2SO_4 does not exist in the crystalline form in the atmosphere. Dry $(NH_4)_2SO_4$ particles (ammonium sulphate) absorb water at RH_w above 80 % (deliquescence point) and may return to a crystalline form only below 37 % RH_w once wet (efflorescence point), exhibiting a hysteresis behavior. Na_2SO_4 particles (sodium sulphate, the main sea salt sulphate species) have their deliquescence and efflorescence points at 84 % and 58 %, respectively (Tang and Munkelwitz, 1994). These values are particle size and temperature dependent (Onasch et al., 1999). Sulphate particles are thus often found within solution droplets in the atmosphere (when not frozen), on one hand causing much light scattering, and on the other hand contributing strongly to cloud initiation. In some numerical model parameterizations, the CCN concentration is determined solely by the sulphate mass concentration (Lohmann and Roeckner, 1996; Lowenthal et al., 2004). This property could have important consequences for the Arctic troposphere ice clouds. Indeed, more sulphates may imply more activated droplets and therefore potentially more ice crystals formed.

The third reason for emphasizing the particular role of sulphates in cloud formation comes from their potential for inhibiting ice nucleation. This effect, which we term sulphate-induced freezing inhibition (SIFI), could explain observations of reduced

ice forming nucleus/nuclei (IFN) concentrations during certain Arctic haze events (Borys, 1989), and may have profound consequences on the Arctic cloud cover. At the microphysical level, it is becoming clear that at least one heterogeneous nucleation mode is involved. Laboratory experiments on the deposition mode performed by Eastwood et al. (2009) show that kaolinite particles coated with H_2SO_4 require about 30 % more ice supersaturation for initiating ice nucleation in the 233-246°K temperature range, whereas $(NH_4)_2SO_4$-coated particles undergo a similar effect at 240°K and 245°K (but a much reduced effect at 236°K). When the supersaturation production rate is high enough for RH_w to reach 100 %, liquid droplets may be activated, and subsequent ice nucleation may follow either by immersion/freezing (an IFN acts after having been immersed), by condensation/freezing (the CCN later acts as an IFN during the condensation stage), or by contact (an external IFN touches the droplet surface). We are aware of no laboratory experiment assessing the role of coating in these modes, but we consider that it could be important for contact nucleation, since the involved IFN may cross the droplet surface or rebound without touching it directly, as well as for condensation/freezing at the beginning of the condensation process. It is on the other side probably less important for immersion nucleation and for condensation/freezing once the droplet has become large, since sulphates then get strongly diluted. As for homogeneous freezing, haze droplets require colder temperatures when sulphate concentrations are higher (Bertram, Patterson and Sloan, 1996). Laboratory research involving all nucleation modes and a great variety of IFN types is needed for a better understanding of the role of sulphates in ice cloud formation. Given the present state of knowledge however, it is reasonable to hypothesize that the SIFI is effective within the Arctic troposphere during winter.

The impact of the SIFI on Arctic climate cannot be fully assessed solely from modelling work based on the few laboratory measurements obtained thus far, because the real Arctic IFN mixture shows a large diversity in composition, size, shape and thermodynamic state. Inferences from in situ observations are also limited, due to the paucity and local character of the measurements. Moreover, the SIFI effect can also not be tested directly from the satellite measurements alone, because we can hardly design a credible proxy for in-cloud sulphate concentrations. Hence, in this paper, we test the SIFI potential consequence according to which higher sulphate concentrations favour cloud populations made of larger ice crystals, caused by a reduction in the competition for water vapor when fewer IFN may operate (Girard and Stefanof, 2007). To achieve this task we

have developed the Arctic Winter Aerosol and Cloud Classification from CloudSat and CALIPSO (AWAC4) algorithm. First, it identifies two types of ice clouds (TIC) which are relevant to the present study, one (termed TIC-2B) supposedly favoured by high sulphate concentrations at the expense of the other (TIC-2A). As explained in detail in the methodology section, the crucial difference between these cloud types stems from TIC-2A being topped by a cover of very small (radar-unseen) ice crystals (termed TIC-1), whereas TIC-2B are not. Next, the AWAC4 algorithm assesses the sulphate concentration in non-cloudy probed volumes (bins), via a proxy based on the lidar backscattering fields and validated using ground measurements from the Zeppelin station (in Svalbard Islands, Norway). Finally, the clouds and the sulphate concentration proxy may be spatially characterized, and different correlations relevant to the SIFI effect are calculated and interpreted. This work furthers the previous efforts in this direction made by Grenier, Blanchet and Muñoz-Alpizar (2009) (hereinafter: GBM, 2009).

2.2. Observational data sets

2.2.1. Satellite data sets

The CALIPSO and CloudSat satellites were launched on April 28th, 2006 and joined the A-Train constellation on a heliosynchronous orbit at an altitude of 705 km. Data sets derived from measurements of their instruments have been described many times in the literature, therefore we merely summarize the information here. Satellites cross the Arctic region 14-15 times per day, with a nadir latitude up to ~ 82°N.

CALIPSO carries the Cloud-Aerosol Lidar with Orthogonal Polarization (CALIOP) instrument, whose beam hits the ground with a footprint of ~ 70 meters. For this study, we use the total (β_{532}) and perpendicular (β_{per}) attenuated backscattering fields at 532 nm, as well as the total attenuated backscattering field at 1064 nm (β_{1064}). We focus on the lower troposphere, for which the second version (V2) fields are available with 30 meters vertical and 333 meters horizontal resolutions. Hunt et al. (2009) provide further technical details about the mission as well as a performance assessment. Figure 2.1a shows an Arctic example scene as probed by the lidar (β_{532}) on January 5th, 2009.

The 3878 juxtaposed profiles (after averaging for mapping on the CloudSat grid) extend from Greenland to the Chukotski Peninsula (trajectory shown in Figure 2.2).

CloudSat is lagging CALIPSO by about 15 seconds. Measurements from both platforms are thus nearly coincident in space and time. Cloudsat carries the Cloud-Profiling Radar (CPR), with a frequency of 94 GHz (3 mm wavelength). A profile sampling is performed at every ~ 1100 meters on the ground, with a 1.4 x 2.5 km footprint (cross-track x along-track), whereas the vertical sampling is 240 meters. Stephens et al. (2002) provide an overview of the CloudSat mission. Microphysical properties retrieved from the radar reflectivity (level 1B product) include ice water content (IWC) and ice effective radius (r_{ie}) from the R04 2B-CWC (level 2) product. We used this product for our cloud classification algorithm, and we refer to Austin, Heymsfield and Stephens (2009) for details about the retrieval. Since Kahn et al. (2007) have found that the radar sensitivity is greatly reduced in the first 3-4 levels just above the surface, we exclude data in the first kilometre above the surface (generally 4 levels, sometimes 5) from the cloud field analysis. This surface contamination effect in the boundary layer data results from the radar pulse length of 1000 meters (Schutgens and Donovan, 2004). The R04 ECMWF-AUX temperature field, which consists of the ECMWF analysis interpolated at the CloudSat sampling positions, is also used.

2.2.2. In situ sulphate concentration measurements

For this study, we use the winter 2007 (December 2006, January and February 2007) and winter 2008 (hereinafter winter-07 and winter-08) sulphate and sodium concentrations measured at the Zeppelin Mountain Station (Aas et al., 2008). These are provided by the European Monitoring and Evaluation Programme (EMEP) Chemical Coordinating Centre at the Norwegian Institute for Air Research (NILU; station code NO0042R). Sulphate concentrations have been measured at this station since 1990, with a 24-hour time resolution. Geographical coordinates are lat_{Zep} = 78.90°N and lon_{Zep} = 11.88°E. The station is located at 474 m above sea level (asl), which is very often above the temperature inversion. Therefore contamination from local sources is minimal, and average concentrations may be considered representative of what could be measured elsewhere in the region. Air inorganic components are sampled using a 3-stage filter

pack, where the front filter (Teflon Gelman Zefluor, with 2 μm pore size) collects particles with an undefined size cut-off. The water extract from the aerosol filter was analyzed using an ion chromatograph. For further technical details, see the EMEP Manual (EMEP, 1996). Total sulphate concentrations ($[SO_4 - S]_{tot}$) are provided in units of micrograms of sulphur (S) per cubic meter (μg S / m^3) and are multiplied by the sulphate-to-sulphur mass ratio (3.00) for this study, so that unless otherwise stated the discussed quantity is $[SO_4]_{tot}$. To assess the sea salt contribution in sulphates, we use sodium concentrations ($[Na]$), in μg Na / m^3. Detection lower limit is 0.01 $\mu g / m^3$ for both $[SO_4 - S]_{tot}$ and $[Na]$. For certain days, input concentrations are either invalid (as judged by the data provider) or below the detection limit. In the latter case, we use two-thirds of the detection limit. Data from March-April 2000, coinciding with the ASTAR 2000 campaign, are also used for assessing the Arctic haze threshold with the sulphate concentration proxy, as explained later.

2.2.3. Investigation period and domain

Although sulphate concentrations and acidity in the Arctic culminate in April (Sirois and Barrie, 1999), the SIFI effect could potentially be most important during winter, when temperatures are coldest. Indeed, supporting field observations by Borys (1989) have been performed at -25°C, and supporting laboratory measurements on ice nucleation were conducted at even colder temperatures. Furthermore, the AWAC4 algorithm performance for identifying small crystal size mode ice clouds (TIC-1) is poor in presence of daylight, because of the important solar contamination in the lidar wavelengths. For these reasons, we chose to exclusively investigate the December-January-February night-time orbital segments of the three winters (2007, 2008, 2009) since the launch of the CALIPSO and CloudSat satellites. For the nine winter months from December 2006 to February 2009, we gathered data from 3143 overpasses, comprising 10 990 147 CloudSat profiles (and ~ 3.26 times more CALIPSO profiles).

The investigated domain extends from 66.5°N to ~ 82°N, the northern limit of the A-Train orbit. The farther north an area, the better its satellite coverage, as shown in Figure 2.2, in which delimitation of the different sectors discussed in this study are also

presented. The TIC-2B cloud fraction as well as the sulphate concentration proxy, two variables defined in the next section, are presented and discussed for the full circum-Arctic investigated zone. However, the different correlations between these fields are computed and/or discussed only for the Eastern Russia-Beaufort Sea-Canadian Archipelago (EBC) sectors, due to the identification of these sectors by GBM (2009) as the most likely to be affected by the SIFI effect.

2.3. Methodology

2.3.1. Cloud identification from satellite data

Because the AWAC4 algorithm (v1) has already been detailed by GBM (2009), we only summarize its main steps and present the modifications introduced in the current version (v2). The cloud classification methodology is summarized in Table 2.1. Input data are submitted to the following treatment: a) mapping of the CALIPSO fields on the CloudSat grid, b) identification of liquid or mixed-phase layers (MPL) using the sharp β_{532} vertical gradient at their top and base, c) identification of large ice crystal clouds (TIC-2), for which IWC > 0 in the CloudSat field (not including clouds previously identified as MPL), d) identification of small ice crystal clouds (TIC-1), for which IWC = 0 but β_{532} and the depolarization ratio ($\delta \equiv \beta_{per} / (\beta_{tot} - \beta_{per})$) values are likely to correspond to ice clouds, and e) classification of TIC-2 into sub-types (A, B, C, D, E), depending on the presence or absence of MPL and TIC-1 above. TIC-2C correspond to ice crystals precipitating below mixed-phase clouds, and are well identified by the algorithm. The SIFI effect may potentially operate on MPL/TIC-2C systems (Girard, Blanchet and Dubois, 2005), but these are not investigated in this study. The central objective of the AWAC4 algorithm regarding clouds consists of separating as clearly as possible TIC-2A, covered by a TIC-1 layer, from the uncovered TIC-2B, for reasons soon explained. Owing to a great diversity within cloud configurations, this separation is sometimes difficult, so that at the expense of statistics on TIC-2A and TIC-2B systems, we have created two classes of ambiguous cases: TIC-2D, covered by a TIC-1 layer of intermediate thickness, and TIC-2E, for when there is a gap between the TIC-2 and TIC-1 layers. TIC-2B may maximally have 4 TIC-1 bins within the three-profile window above (which comprises the current plus the 2 neighbouring profiles). The latter bins may be

separated and/or far over the TIC-2B bins, or packed together and right above, in which case they form a layer with an average thickness of 320 meters. On average, this layer must extend over at least 800 meters (10 bins) to be considered as TIC-2A, in-between cases being identified as TIC-2D (ambiguous thickness case). Juxtaposition of the small and large size mode layers in TIC-1/2A systems is ensured by requiring that at least 70 % of the TIC-1 layer (7 bins) lay within the 1200 meters (15 bins) just above the TIC-2 layer, otherwise we have TIC-2E (ambiguous gap case).

As for why only some of the TIC-2 are topped by a TIC-1 cover, we consider that the answer first resides in the dependence of ice nucleation on IFN availability and size. When an air mass is cooling, ice particles may start to form when the relative humidity with respect to ice (RH_i) approaches 100 %, via the deposition mode. Larger solid aerosol particles, having statistically more active sites, are better IFN, and this size dependence for ice formation efficiency has recently been demonstrated for many dust types in the -20°C to -50°C temperature range (Welti et al., 2009). Hence, in conditions of stronger vertical motion (higher supersaturation production rate), smaller aerosol particles may also contribute to nucleate ice, increasing the supersaturation sink term and ultimately leading to a cloud made of more numerous and smaller ice crystals (TIC-1). If the vertical movement is sustained, some ice crystals will eventually grow to precipitation sizes and aggregate, forming precipitating TIC-2A below the TIC-1 layer. Conversely, in conditions of weaker vertical motion, only large IFN act to form the cloud, leading to a thinner or non-existent TIC-1 layer above the precipitating TIC-2B layer. This is also consistent with the maximal occurrence of TIC-1/2A systems being found several kilometres above that of TIC-2B, for both highly polluted (e.g. Eastern Russia) and less polluted areas (e.g. Antarctica) (GBM, 2009). When RH_w reaches 100 %, the size dependence for ice formation efficiency remains important at least for the immersion mode (Marcolli et al., 2007). However, Pruppacher and Klett (1997) report an absence of studies for size dependence effect of IFN acting in the contact mode and mention that the condensation/freezing mode tends to be less affected than the immersion mode (we have found no recent study concerning these modes in the literature). Despite some arbitrariness in having the criterion used for separating TIC-2A from TIC-2B based on the radar sensitivity, we found after inspection of all the 3143 investigated scenes that the algorithm gives appropriate results, since it is consistent with the previous explanation in three important ways. First, we observe a good profile-to-profile auto-correlation in TIC

types, consistent with minimal continuity which we expect in the synoptico-microphysical conditions giving birth to a cloud system. Secondly, we often find TIC-1/2A in the center of a cloud cover, with TIC-2B on the sides, but rarely the opposite situation. And finally, TIC-2B are much more likely to present a highly variable top altitude within one structure, suggesting that the majority of ice crystals in their top are precipitating rapidly.

We consider that the SIFI effect superimposes on the size dependence effect and acts to shift the TIC-2 distribution from TIC-2A (with a clear thick TIC-1 top) to TIC-2D (TIC-1 top of intermediary thickness) to TIC-2B (no or thin TIC-1 top). By counting the number (n) of TIC-2B, TIC-2D and TIC-2A bins, we may simply define the TIC-2B fraction among these various cloud cover types (F_{2B}) within specific altitude and time intervals over an area as:

$$F_{2B} = \frac{n_{2B}}{n_{2B} + n_{2D} + n_{2A}} \tag{2.1}$$

A strong SIFI effect should cause pan-Arctic F_{2B} patterns to present its higher values downwind of the areas showing higher sulphate concentrations (in terms of prevalent circulation during the time interval considered).

For identifying radar-unseen TIC-1 (after the MPL and TIC-2 identification and prior to the TIC-2 sub-classification), the algorithm considers first the backscattering at 532 nm, by requiring that $\beta_{532} \geq \beta_{532\_min} = 0.0009\ km^{-1}sr^{-1}$ for a bin to qualify. Next, there is a further requirement that the depolarization ratio (δ) present some minimal value and satisfy:

$$\delta \geq \delta_{min} = a_0 + a_1 / \beta_{532} \tag{2.2}$$

with $a_0 = 10^{-2}$ and $a_1 = 8 \cdot 10^{-5} km^{-1}sr^{-1}$. The choice for the shape of the δ_{min} function has been discussed by GBM (2009). Parameters have been fixed by trial and error (inspecting the results for many individual scenes similar to that in Figure 2.1), and by considering the β_{532} and δ distributions. Unfortunately, the haze and TIC-1

distributions overlap in the (β_{532} , δ) space. This is partly due to the presence of particles of one feature (aerosol or ice crystals) within probed volumes dominated by the other, and it limits the performance of the algorithm in correctly identifying TIC-1. Finally, TIC-1 bins not surrounded by at least one other of their kind among the eight neighbouring bins were declassified, to reduce noise in the TIC-1 signal. The color ratio χ ($\equiv \beta_{1064}/\beta_{532}$) is not used for identifying TIC-1 in the current version of the AWAC4 algorithm.

Figure 2.1c presents the cloud classification results for the example scene. On the left we may observe TIC-1 bins (yellow) covering TIC-2A bins (green) over Greenland and the Ellesmere Island, with some profiles classified as ambiguous (violet), as well as a TIC-2B (red) area on the western side of the system. On the right half of the scene we see mainly a TIC-2B system, combined with TIC-1/2A and TIC-2D profiles.

2.3.2. Sulphate concentration proxy

We term "cloud free" a bin not labelled as MPL, TIC-2 or TIC-1. Additionally, the bin must not be under any cloud layer, in which case the lidar beam is attenuated and the bin is classified as such. To detect the presence of sulphate particles within these bins, we use an index (α) based on the CALIPSO total attenuated backscattering at 532 nm (β_{532}) and the color ratio (χ) defined as:

$$\alpha \equiv \frac{w_\beta \cdot f(\beta_{532}) + w_\chi \cdot g(\chi)}{w_\beta + w_\chi} \tag{2.3}$$

with:

$$f(\beta_{532}) = \min(\max(0, \beta_{532} / \beta_{ref}), \beta_{ref}) \tag{2.4}$$

and:

$$g(\chi) = \max(0, 1 - m|\chi - \chi_0|) \tag{2.5}$$

This lidar-derived index is a new version of that used by GBM (2009), in which the constants w_β and w_χ represent weights for the backscattering (first) and color ratio (second) terms. The function $f(\beta_{532})$, corresponding to the β_{532}/β_{ref} ratio bounded between 0 and 1 (the maximum value is set if $\beta_{532} \geq \beta_{ref} = 0.0030 km^{-1} sr^{-1}$), reflects the expectation that the presence of sulphate particles among air molecules contributes to increase the backscattering. A caveat with this term stems from the existence of other aerosol compounds and especially of ice crystals in bins classified as cloud free, which may significantly contribute to raising of the index. By giving weight to $g(\chi)$, a triangular function with amplitude 1 at its center $\chi_0 = 0.35$ and non-zero values only between 0.15 and 0.55 ($m = 5$), we limit the effect of the ice crystals on the index, because $\chi \cong 1$ for clouds (Wandinger, 2005; Liu et al., 2002). This function also ensures that bins with small aerosol loadings score low in the α index, since $\chi_{molecular} \cong 1/16$ in virtue of the λ^{-4} dependence for Rayleigh scatterers (Wandinger, 2005). However, due to small β_{532} and β_{1064} signal-to-noise ratios in molecular bins, the color ratio field is too noisy in these circumstances for the second term of eq. 2.3 to be given full weight. The parameters of the triangular function have been chosen considering the theoretical work of Liu et al. (2002), which have inferred from LITE observations that the frequency of occurrence of integrated attenuated color ratio for aerosol layers is highest in the interval $0.15 < \chi \leq 0.55$ (approximately; their probability function is not triangular). Figure 2.1b shows the color ratio field for the example scene. Clouds, identified independently of the color ratio, appear with values ranging from a minimum of about $0.50 < \chi \leq 0.60$ to a maximum above 1.0. For cloud free and relatively clean air (at high altitudes), the signal is very noisy (the noise is reduced after the mapping on the CloudSat grid by setting β_{532} and β_{1064} minimal threshold values at $1 \cdot 10^{-5} km^{-1} sr^{-1}$ and $\chi_{molecular} \cdot 10^{-5} km^{-1} sr^{-1}$, respectively). Between longitudes -82.6°E and -111.2°E, we see a singular feature (pale blue) contrasting strongly with the adjacent cloud cover. These color ratio values ($0.30 < \chi \leq 0.40$) lead to high α values, as shown in Figure 2.1d.

It is generally considered that frozen water, humidity and sulphates account for nearly all the light scattering from Arctic haze (AMAP, 1998), but other major aerosol

types found in the Arctic also contribute to raise $f(\beta_{532})$ above the value for sulphates only. We do, however, expect this contribution to be limited. For instance, soot particles cannot contribute strongly to raise this term of eq. 2.3, even though they scatter light as small individual particles (Clarke, 1989). Indeed, they have a marginal effect on the backscattering when mixed internally within haze (Blanchet and List, 1983), where they generally represent about 5 % of the total aerosol mass (Shaw, Stamnes and Hu, 1993) and rather act as absorbers. Likewise, giant sea salt particles are expected to scatter light less efficiently than fine sulphate particles for a same mass concentration (Waggoner and Weiss, 1980). A high sea salt mass concentration, as observed during sodium storm events (sudden and short-duration $[Na]$ increase), can cause much scattering. However, because maritime mixtures under high relative humidity are most likely to present attenuated color ratio values around 0.7 (Liu et al., 2002), their score in $g(\chi)$ is a priori expected to be low. This is linked to the color ratio being considered a good proxy of the size of the probed particles (Omar and Babakaeva, 2004), with smaller color ratios associated with smaller aerosol particles. However, scattering from very large particles (comparatively to 1064 nm in our case) does not respect that dependence on wavelength, and clouds generally exhibit $\chi \cong 1$. Due to their large size, dust and marine aerosols can also exhibit χ values near or even above 1, whereas for aerosol mixtures containing much pollution (including submicron-size sulphate particles) the color ratio should be much smaller than 1 (Omar and Babakaeva, 2004). It must, however, be kept in mind that the aerosol fine (submicron) mode is not exclusively composed of sulphates. Using Terra MODIS collection 5 (collection 4) data over various oceanic regions, Yu et al. (2009) have retrieved fine mode fractions of 0.90 (0.92) for pollution, 0.37 (0.51) for mineral dust and 0.45 (0.32) for the natural marine aerosol. These numbers vary spatially and seasonally, but the values suggest that other aerosol compounds contribute to raise $g(\chi)$ less than Arctic haze compounds do.

From the previous considerations, we expect α to be a reasonable sulphate concentration proxy, with higher values potentially indicative of Arctic haze events. This proxy must, however, be validated. Unfortunately, only a few sulphate concentration time series are available for the Arctic, station locations are seldom comprised within the instruments footprint when satellites fly over the area, and cloud cover often hinders the calculation of α. We are then obligated to average α over a wide zone. Furthermore,

when the station is located at an altitude too low, the sulphate concentration must be compared with the proxy calculated and averaged for a higher altitude layer. At the moment of doing the analysis, in situ sulphate concentration data sets from three monitoring Arctic sites were available: Zeppelin (78.90°N, 11.88°E, 474 m asl, daily-averaged), Alert (82.47°N, 62.50°W, 100 m asl, weekly-averaged) and Barrow (71.30°N, 156.60°W, 8 m asl, daily-averaged). Each station presents advantages and drawbacks in regards to the validation/calibration of α. After analysis of the satellite overpasses around each site, it appeared to us that only data from Zeppelin could be used for the present study. The Barrow station has data usable only for precise wind conditions due to possible local contamination, its satellite coverage is small and its altitude too low. Problems with the Alert station come from a location latitude too high for the satellite overpasses, combined with the high elevation of Greenland and Ellesmere Island on its southern side, which prevents from averaging α around the site and at a comparable altitude. These geographical limitations are not encountered at the Zeppelin station. However, because it is located in the North Atlantic sector, the frequent cloud cover reduces the statistics and the marine aerosol has more influence on the calibration of α. Details of the comparison procedure are discussed in section 4.2.

A major difference in the way CALIPSO data were collected during the investigation period stems from the fact that the CALIOP instrument has been reoriented at an off-nadir angle (ONA) of 3.0° at the end of November 2007 (this angle was previously 0.3°). It is well-known that the depolarization ratio, used for identifying ice crystals (TIC-1), is sensitive to the off-nadir angle (Sassen, 1991). Indeed, in presence of plate-like horizontally oriented crystals, increasing ONA results in higher depolarization values (Vaughan, 2008). This causes further biases in cloud and sulphate detection, as discussed later.

2.3.3. In situ data

Because coarse aerosol particles like sea salt are less likely to exhibit small color ratio values than particles in the accumulation mode are, we correct sulphate concentrations observed at the station by removing the contribution of sea salt from the total measured value. Considering a mass concentration ratio $[SO_4] / [Na] = 0.252$ in the

sea water composition (Broeckner and Peng, 1982), the following formula is used for assessing the non-sea salt (nss) sulphate mass concentration:

$$[SO_4]_{nss} = [SO_4]_{tot} - 0.252[Na] \quad (2.6)$$

This correction may be important, as we found that average sea salt contribution in the sulphate concentrations measured at Zeppelin was 20 % during both winter-07 and winter-08. Sea salt has the potential to increase the mean diameter of sulphate aerosols by up to a factor of 2 over the marine boundary layer (Gong and Barrie, 2003). The color ratio signal may thus be affected, with a considerable fraction of the sulphate mass not detected. A priori, we did expect α to correlate better with $[SO_4]_{nss}$ than with $[SO_4]_{tot}$.

2.4. Main results

2.4.1. Lidar off-nadir angle effect

The algorithm applied to input data is the same for all investigated scenes, but a bias may result from the increase in the lidar off-nadir angle (ONA) performed between winter-07 and winter-08. An expected change from the modification of this instrumental variable is an increase of the depolarization ratio (δ) from ice crystals, since specular reflection on horizontally oriented plates is reduced by an ONA increase (Sassen, 1991).

Visualization of the 3143 scenes (cloud classification and the sulphate concentration proxy α) clearly shows that ONA increase has an impact on the TIC-1/aerosol separation in the upper troposphere. At these altitudes, the probability of finding a highly concentrated aerosol layer is low, and we can identify with a high level of confidence the high α features which should be classified as TIC-1, mainly by verifying the continuity in their spatial structure. Between 5 km and 12 km altitudes, we estimate that the AWAC4 algorithm misclassifies vast portions of TIC-1 in about 22 %, 13 % and 20 % of the scenes during Dec-06, Jan-07 and Feb-07, respectively. This percentage falls below 1 % for all months after ONA increase (with a comparable proportion of scenes containing TIC-1 at these altitudes for all months). Most affected TIC-1 have no TIC-2A

extension and generally consist of horizontally wide features (extending over hundreds of kilometres).

Lower in the troposphere, it is harder to quantify the impact of ONA increase, since aerosol layers are likely to be found juxtaposed to or in-between cloud systems. We could therefore find no clear evidence of a TIC-1 distribution change simply by visualizing the scenes. Figure 2.3a shows the normalized δ distributions for all bins satisfying $\beta_{532} \geq 0.0005 km^{-1} sr^{-1}$ and within the altitude range 1000–5000 m. Curves show that after ONA increase, there were fewer bins with δ ~ 0, but more in the range δ ~ 0.2-0.6, as expected. However, a change in the relative abundance of haze and clouds could potentially mimic the ONA change effect. It is not clear which effect dominates, but both could be important. The shift to the right in the radar-seen (TIC-2A + TIC-2B + TIC-2D) δ distribution (Figure 2.3b) can only be explained by the ONA change (unless we suppose that a change in the average vertical movement has caused a change in the proportion of horizontally oriented ice crystals, but results are similar if we consider only TIC-2B, which are expected to be associated with slower vertical movement). The peaks near δ ~ 0 in Figure 2.3b are most likely due to molecular or haze contribution just above TIC-2 tops. The δ distributions for aerosols (Figure 2.3d) and TIC-1 (Figure 2.3c) are also consistent with expected consequences from ONA increase. Indeed, in the first case we expect a shift to the right caused by the small amount of crystals present within these bins, whereas in the second case we expect the shift to be different from that for TIC-2, since bins which would have been classified as haze (had the lidar not been inclined) enter the TIC-1 δ distribution from the left side.

Therefore, it is reasonable to conclude that the lidar inclination has a real influence on the haze / TIC-1 partake, and consequently on the average sulphate index and the TIC-2A / TIC-2B partake (since TIC-2A are defined by the existence of an overlaying TIC-1 layer). For this reason, it is important to analyse both periods (before and after ONA increase) separately. Changes in the abundance ratios estimated with our algorithm could also partly come from changes in the 'true' abundances between winter-07 and the two subsequent winters, since the χ distributions for all bins (satisfying $\beta_{532} \geq 0.0005 km^{-1} sr^{-1}$) also change (not shown), whereas we found no mention in the

literature on how the lidar ONA could affect this variable (this issue remains unanswered by the scientific community).

2.4.2. Validation of the proxy

We have compared daily-averaged concentrations of sodium and sulphate (as well as their sum and nss-sulphate) from Zeppelin in situ data to the index α, within a geographical box centered on Zeppelin. For the index, three box sizes have been tested (250, 500 and 1000 km), as shown in Figure 2.4 (also shown for Alert, Canada). It appeared that for both winter-07 and winter-08, index series for 500 km better reproduce the in situ data than the index series for 1000 km do. For their part, index series for 250 km offer too few observation data to provide a reliable comparison. The validation exercise therefore focuses on the 500 km series. This represents a compromise between minimizing the footprint-to-station distance and having enough points to average for most days. For instance, borders for the 500-km box are determined by setting $lat_{\min}$ and $lat_{\max}$ at 250 km southward and northward of lat_{Zep}, and by setting $lon_{\min}$ and $lon_{\max}$ at 250 km westward and eastward of lon_{Zep} at the lat_{Zep} latitude. The index is averaged for each day by considering all values within the altitude interval from 224 m above ground level to 724 m asl. Certain of the daily point pairs have been ignored in the subsequent analysis, because either in situ data were flagged invalid by the data provider or there were less than $n_{\min}$ = 100 satellite index values to average.

Figure 2.5 shows three curves for each winter: $[SO_4]_{tot}$, $[Na]$ and $\alpha_{2/1}$ (with a 2/1 weight ratio in eq. 2.3). Comparison of the curves suggests that the index is sensitive to both the Arctic haze and the marine aerosol, since most $\alpha_{2/1}$ peaks correspond to either a $[SO_4]_{tot}$ or a $[Na]$ maximum. In particular, it seems clear that sea salt is involved in the $\alpha_{2/1}$ peaks of day 27 and day 58 during winter-07, whereas Arctic haze caused the marked increase in the index for days 44-49 of winter-07. Moreover, there are periods of low $[SO_4]_{tot}$ and $[Na]$ during which the index remains relatively low (first days of winter-07 and days 40-60 of winter-08). Conversely, peaks often mismatch by one or two days, and an important $[SO_4]_{tot}$ peak during the last days of winter-08 is not reflected by

a comparatively important $\alpha_{2/1}$ peak. Numerically, we may assess the correspondence between the curves by calculating the Pearson correlation coefficient ($r_{Pea} = \sqrt{R^2}$). Results are found in Table 2.2, first for all points shown in Figure 2.5. It appears that for all weight ratios tested, the sum ($[SO_4]_{tot}^{all}$ + $[Na]^{all}$) correlates best with the index, as compared with the components considered individually and with $[SO_4]_{nss}^{all}$. Series for $[SO_4]_{tot}^{all}$ and $[Na]^{all}$ correlate equally well with $g(\chi)$, but adding weight to $f(\beta_{532})$ improves the correlation for sodium whereas it worsens it for sulphates. Removing the sea salt portion of sulphates leads to lower r_{Pea} whatever the weight ratio. As it is clear from Figure 2.5 that sodium storms strongly modulate the index values, we also performed the r_{Pea} calculations for a subset of points, excluding those for which $[Na] > 2 \cdot \overline{[Na]^{all}}$ = 0.66 µg / m^3 (this concerned 14 out of 105 daily values over the two winters). Results (Table 2.2) show that ignoring sodium storms leads to higher r_{Pea} between total sulphate concentrations and the index if $w_\beta < w_\chi$. We ensured that 224 m above the surface was high enough to avoid possible contamination of the results from the surface reflection (which could be introduced via errors in the input topographic files or the mapping procedure of CALIPSO data on the CloudSat grid) by redoing the validation exercise with the altitude interval 474-724 m asl and achieving practically identical results for Figure 2.5 and Table 2.2. We also ensured that the mid-January peaks correspondence between $\alpha_{2/1}$ and $[SO_4]_{nss}^{all}$ was not an artifact from misclassified TIC (scoring high in $f(\beta_{532})$) by closely inspecting the color ratio in each of the 14 scenes involved. Certain high $\alpha_{2/1}$ bins are misclassified TIC in one scene of day 44 and one of day 45, whereas the high $\alpha_{2/1}$ features recorded on days 46 and 49 were clearly aerosol layers ($0.30 < \chi \leq 0.40$).

Although results from Table 2.2 should lead to the use of 0/1 ($\alpha_{0/1}$) as the working weight ratio for later applications of eq. 2.3, we rather adopted 2/1 ($\alpha_{2/1}$). This choice stems primarily from the low signal-to-noise ratio in the color ratio (especially when β_{532} remains low), and secondly from the design of $g(\chi)$, which for example has

the same value whether $\chi = 0.20$ or $\chi = 0.50$, whereas in principle the signal should be more dominated by smaller particles in the first case. The color term has been designed to roughly reveal objects in the range $0.15 < \chi \leq 0.55$, but the choice of a triangular function is admittedly arbitrary. For most subsequent results, we briefly refer to the effect of using $\alpha_{0/1}$ instead of $\alpha_{2/1}$. By visual inspection of the relevant fields (β_{532}, χ, δ, α and TIC-1) for several scenes, 2/1 appears as the best weight ratio for contrasting extended aerosol features against the background signal. Overall, both terms in eq. 2.3 are of importance.

The initial objective of comparing α with measured sulphate concentrations was to perform a calibration for the entire Arctic region. While Svalbard Islands are located in North Atlantic and exposed to sodium storms, this is not the case for most of the Arctic, since giant sea salt particles are not likely to be blown far from the sea ice / open waters edge. In this context, we think the best approach for calibrating the index on sulphate concentrations is to use $[SO_4]_{tot}^{sub}$, which correlates positively with α, and we obtain the following linear regression (bounded at a minimal value of zero):

$$[SO_4]_{tot}^{sub} = 7.7 \cdot \max(0, \alpha_{2/1} - 0.42) \qquad (2.7)$$

Although eq. 2.7 is based on a statistically significant correlation between daily-averaged values, we use this calibration equation only to estimate the sulphate concentrations. Of course, the results of its application over North Atlantic and Kara Sea must be interpreted carefully, since these sectors are often devoid of sea ice cover during winter, and therefore sea salt is expected to impact the $\alpha_{2/1}$ signal. Additionally, this calibration is unreliable for any single bin. One important reason for considering eq. 2.7 is that it offers a simple method for identifying Arctic haze. As far as we know, there exists in the literature no definition of an Arctic haze event in terms of a minimal sulphate concentration at the ground. These events are rather identified based on optical properties of the aerosol loading aloft. To obtain a reasonable $[SO_4]_{tot}$ threshold for Arctic haze, we use data from the ASTAR 2000 campaign (March 12th to April 25th), when Yamanouchi et al. (2005) observed a frequency of Arctic haze situations 40 % of the time in the

Svalbard area. Investigating the Zeppelin station $[SO_4]_{tot}$ for that period, we found that 40 % of the daily-averaged concentration values were above $[SO_4]_{haze\_min}$ = 0.96 μg / m^3, a threshold corresponding by eq. 2.7 to $\alpha_{haze\_min} = 0.54$. Because pollution layers may be vertically highly inhomogeneous (Quinn et al., 2007), the correspondence between an optically identified Arctic haze event and a sulphate concentration above $[SO_4]_{haze\_min}$ at the ground is likely to fail for any single day period. When applied over a longer period, however, we think the threshold may give a reasonable indication of the Arctic haze frequency (for non-cloudy conditions). This threshold has been used in Figure 2.1d as the minimal value for the 'high index' interval. The group of red bins in the middle indicates that the lidar likely encountered an Arctic haze event.

2.4.3. Circum-Arctic index distribution

The index ($\alpha_{2/1}$) derived from the CALIPSO data has been used to create an index map centered on the North Pole. All values compiled during the investigated period within each 1° x 5° (latitude x longitude) grid box have been averaged. Results are presented in Figure 2.6 for three different altitude layers and for the two periods separated by the ONA increase (a band of 500 m above ground level is ignored). The patterns here are more relevant to consider than exact numerical index values. Probably the most striking characteristic of Figure 2.6 is the marked difference between the pre- and post-ONA increase index values, due to better TIC-1 classification in the latter case. However, the general pattern is preserved. In both cases we see that the index generally decreases with height. In the lowest layer (500 – 1500 m), highest values occur over North Atlantic, Eastern Russia and Beaufort Sea (see Figure 2.2 for delimitations of the sectors we refer to), whereas above 1500 m North Atlantic becomes the sector with the lowest index values. The fact that the high $\alpha_{2/1}$ feature over North Atlantic has no extension above 1500 m renders us confident that it mostly corresponds to coarse sea salt particles, and that relatively high $\alpha_{2/1}$ values above 1500 m correspond to small sulphate and companion particles originating from Eurasian human activities. Using $\alpha_{0/1}$ instead of $\alpha_{2/1}$ produces similar patterns.

2.4.4. Circum-Arctic TIC-2B fraction

Using the same data grid as for $\alpha_{2/1}$, we have calculated the average F_{2B} during the investigation period (the division in eq. 2.1 is performed after the total numbers of TIC-2A, TIC-2D and TIC-2B bins are determined). Results are presented in Figure 2.7. Again, we see an important difference between the pre- and post-ONA increase, consistent with a better identification of TIC-1 and hence TIC-2A after ONA increase, which raises the denominator in eq. 2.1 and hence lowers F_{2B}. The adopted color scale reveals clearer patterns after ONA increase, when for all layers we have higher F_{2B} values over North Atlantic, Beaufort Sea and the eastern part of Eastern Russia. Before and after ONA increase, Kara Sea, Greenland and the western part of Eastern Russia generally had lower TIC-2A fractions relative to the other sectors. The situation differs for the Canadian Archipelago, since we find high values relative to other locations only before ONA increase. This may be due to a particular circulation pattern during winter-07.

2.4.5. Ice effective radius–index correlation

In GBM (2009), we reported calculation results of the linear correlation coefficients between CloudSat retrieved r_{ie} values at the top of TIC-2B (averaged over the 3 upper bins) and the aerosol index just above (averaged within the 6 closest bins, TIC-1 excluded). We had obtained $r_{Pea} \in [0.09,0.15]$ for the different Arctic sectors, and interpreted this result as an indication of a real SIFI effect. In the current study, we performed a similar calculation, considering all TIC-2B profiles within EBC sectors after ONA increase. Differences with the previous methodology were a) the consideration of only the second to the fourth bins above the cloud (rather than the first to the sixth), b) a modified index, c) the domain, d) the ONA and e) the segregation of the series by height intervals. The goal of ignoring the first bin was to avoid possible contribution of TIC-2B ice crystals to $\alpha_{2/1}$ in the bottom of the bin just above, whereas that of segregating calculations by height intervals was to avoid a false signal coming from the height dependence of $\overline{r_{ie}}$ and $\overline{\alpha_{2/1}}$. Pairs of points ($\overline{r_{ie}}$, $\overline{\alpha_{2/1}}$) were grouped according to the bin number of the highest TIC-2B bin in a profile, starting at ~ 1200 m and ending at ~ 6500

m (asl) with 240 meter-thick intervals. The number of points entering the correlation calculation varied between ~ 20 000 and ~ 30 000 for each bin interval. We did not find systematic positive and significant r_{Pea}. Instead, r_{Pea} remained confined within ~ ± 0.02, with statistically significant values at the 95 % level (through Fisher's z-transformation test) for a few height intervals only. Varying the methodology by considering a) the first bin above the TIC-2B top, b) $\alpha_{0/1}$, c) all Arctic sectors or d) only the period before ONA increase did not change the results qualitatively. However, merging all pairs of points in a single series (no matter the height of the TIC-2B top) led to positive and statistically significant results, i.e. $r_{Pea} = 0.167^{0.170}_{0.163}$ before ONA increase and $r_{Pea} = 0.158^{0.160}_{0.155}$ after (using $\alpha_{2/1}$; comparable results using $\alpha_{0/1}$). In sum, making a deeper analysis of the correlation between r_{ie} at the top of TIC-2B and $\alpha_{2/1}$ just above has provided no proof that sulphates favour cloud populations made of larger ice crystals. Moreover, the signal interpreted by GBM (2009) as supporting the SIFI effect was plausibly an artifact from not considering the height dependences of $\overline{r_{ie}}$ in the TIC-2B tops and $\overline{\alpha_{2/1}}$, which both decrease as altitude increases in the lower troposphere.

2.5. Discussion

2.5.1. Index validation

The index α is meant to be used only as an indicator of sulphate concentrations in the Arctic atmosphere. It is designed following theoretical considerations of how an Arctic haze mixture (not exclusively sulphates) is most likely to affect the lidar backscattering fields, and it is sensitive to unmasked clouds, sea salt and possibly other aerosol mixtures like the mineral dust particles that sulphate droplets are believed to coat and deactivate as IFN. These limitations must be kept in mind. On the other hand, in the absence of a pan-Arctic in situ sulphate concentration data set or of a better satellite-derived product, such an index is an appropriate sulphate concentration proxy and may be useful for locating Arctic haze, away from open waters.

As can be seen in Figure 2.5, the $\alpha_{2/1}$ signal averaged within a 500 km-wide box centered on the Zeppelin location may capture variations of measured sulphate

concentrations, particularly when sodium concentrations remain low. However, it is clear that some high values in $\alpha_{2/1}$ are better explained by a sodium storm, and determination coefficients (R^2) between the various index series (differing by their w_β / w_χ ratio) and the (total or non sea-salt) sulphate concentrations remain relatively low. These low values are due to both partial inadequacy of the indicator and inescapable limitations in the validation methodology adopted. Inadequacy of the sulphate concentration proxy is expected through potential sensitivity to other parameters. The marine aerosol is difficult to separate from Arctic haze based on the color ratio and we must also rely on previous knowledge of the geographical and vertical extensions of these two different mixtures when interpreting $\alpha_{2/1}$ distributions in Figure 2.6. Methodological limitations include the spatial mismatch between satellite trajectories and the station, the fact that overpasses are temporally concentrated within a few hours whereas the in situ instrument averages aerosol data over the whole day, and the exclusion of below-cloud aerosols from the satellite data, reducing statistics and possibly introducing a bias. Some pollution events may pass through the station one day and be crossed by the satellite trajectories the day after (or never), and vice versa. To strengthen the analysis, in situ sulphate and sodium particle number size distributions could be implemented, since the index may correlate better with the fine mode rather than the bulk mass. Such size distributions (e.g. from the EMEP project CREATE) were not available for winter-07 and winter-08 at the moment of the analysis. The weakening of the correlations when we replace $[SO_4]_{tot}^{all}$ with $[SO_4]_{nss}^{all}$ may result from underestimation of the sea salt fine-mode fraction.

We can also evaluate our thinking that $\alpha_{2/1}$ is indicative of the sulphate concentration by examining the patterns obtained in Figure 2.6 in light of information in the literature about the sulphate field. For example, the patterns we observe in the present study are in general agreement with numerical simulation results obtained by Christensen (1997). His results suggest that sulphur transits through the High Arctic (northward of 74.5°N) mostly within the Eastern Russia-Beaufort Sea-Canadian Archipelago (EBC) sectors during winter (1991-1994), with the most important positive flux within 45-135°E and the most important negative flux within 75-165°W, for the lowest 3 kilometers asl. However, the analysed $\alpha_{2/1}$ and modelled $[SO_4]_{tot}$ patterns do not match perfectly. Differences are partially due to a) not considering the same layers, b) the absence of in-

cloud and below-cloud sulphate contributions in $\alpha_{2/1}$, c) sulphate emissions having changed substantially since 1991-1994 (Quinn et al., 2007), d) the circulation variability strongly modulating sulphur injection fluxes from one year to the other (Eckhardt et al., 2003), e) limitations of the index and f) biases in the numerical simulation.

As a proxy for sulphate concentrations, α could certainly be improved. To achieve this, more aircraft-assisted field campaigns are needed to determine the bulk depolarization and color ratio for clouds and aerosol mixtures. For example, Liu et al. (2002) have computed that only a small proportion of clouds should exhibit a color ratio smaller than 0.54. However, we found that after ONA increase these proportions were 24 % for (TIC-2A + TIC-2B + TIC-2D) and 60 % for TIC-1 throughout the Arctic (18 and 52 % for winter-07). It would therefore seem that the separation criterion is not as sharp as what the calculations of Liu et al. (2002) indicate. Many misclassified TIC-1 bins can thus score high in $g(\chi)$ (although it is not fully understood why the overlap gets greater after ONA change). When plotting the χ distribution for all bins (not shown), we obtain two modes which separate at $\chi \approx 0.55$, therefore confirming the splitting criterion for ice clouds and aerosol layers obtained by Liu et al. (2002). However, the degree of overlap that we found between aerosol and cloud χ distributions is greater, since in the real atmosphere haze and ice crystals are mixed within the same volumes. The depolarization ratio, which is not used in the current version of the index (but previously used in the AWAC4 algorithm for segregating TIC-1 from non-cloudy bins) could be incorporated. However, as for the color ratio, a caveat is that the presence of ice crystals within haze-dominated volumes would bias the depolarization ratio (Bourdages et al., 2009). The relative humidity, which strongly influences the size of hygroscopic particles and consequently their contribution to β_{532} and χ (Sasano and Browell, 1989), could also be used. A-Train water vapour products (e.g.: AIRS) have unfortunately too low vertical and horizontal resolutions to be meaningfully incorporated in our algorithm, unless we further smooth CloudSat and CALIPSO signals, in which case we would miss many TIC-1 tops and hardly be able to separate TIC-2A from TIC-2B.

Prior to the validation/calibration of α, the feature classification algorithm may give results inconsistent with the reality due to a) uncertainties in the lidar fields used, b)

assumptions in the radar ice water content retrieval, c) attenuation of the lidar beam, d) spatial and temporal mismatch in satellites orbits, e) averaging processes, and f) feature classification algorithm assumptions and thresholds. GBM (2009) have discussed these sources of uncertainty in detail. Two modifications which could possibly improve the algorithm are a) a treatment of the Rayleigh scattering, for assessing the molecular contribution to the backscattering - see Haladay and Stephens (2009) for methodology, and b) a retrieval through the lidar equation, for having intrinsic (volume) instead of attenuated backscattering fields - see Sasano and Browell (1989). However, practical limitations could prevent these operations from leading to a significantly better classification in the end, because we would thus have to incorporate meteorological fields with a possibly high degree of uncertainty at the CloudSat resolution (like pressure and temperature for Rayleigh scattering) or make many assumptions to account for non-existent information (like the lidar extinction-to-backscatter ratio for the retrieval). The lidar ratio depends on the microphysical, chemical and morphological properties of the ensemble of particles in the probed volume. Ansmann and Müller (2005) report typical values of 20-35 for marine aerosol and 35-70 for urban-like particles (akin to Arctic haze). For a sky devoid of radar-seen water content, the decrease in the signal attributed to haze and TIC-1 which would result from removing the molecular contribution (C_{Ray}) and the increase that would occur following a retrieval procedure (C_{att}) should both grow in magnitude for decreasing altitudes, and partially cancel each other. Correcting for the Rayleigh scattering without correcting for the attenuation would exacerbate the situation if $|C_{Ray}| < 2 \cdot |C_{att}|$. Moreover, the retrieval within or below radar-seen clouds would often be performed on a depleted lidar signal, hence consisting of amplifying noise and leading to a divergent solution. Nevertheless, the effect (on α and F_{2B}) of performing these two operations needs to be investigated.

2.5.2. Implications for the SIFI effect

The AWAC4 algorithm allows for a spatial characterization of the features implied by the SIFI effect, namely ice clouds and aerosols. However, we face limitations when trying to interpret their spatial distributions in terms of the SIFI effect, and many assumptions are necessary. If we assume that $\alpha_{2/1}$ is a reasonable proxy for sulphate

concentrations in the EBC sectors, there are two approaches we can explore for possibly validating or rejecting the SIFI plausible consequence according to which high sulphate concentrations favour cloud populations made of bigger ice crystals. The first consists of analysing together the spatial distributions of $\alpha_{2/1}$ and F_{2B} (distributions test), and the second consists of correlating r_{ie} at the top of the TIC-2B with $\alpha_{2/1}$ just above (cloud top correlation test). For each test, we have developed an interpretation in terms of the SIFI effect, which we present here. Unless otherwise stated, we discuss the period after ONA increase.

By comparing the $\alpha_{2/1}$ and F_{2B} patterns, we may establish our first conclusion that that there is no evidence of a strong local impact of the SIFI effect in EBC sectors. Indeed in this case, we could reasonably expect $\alpha_{2/1}$ maxima (e.g.: over Laptev Sea and Norilsk area, in the South of the Taimyr Peninsula) to correspond to F_{2B} maxima in some altitude layer, and it is generally not the case. If the SIFI is effective around Norilsk, it could mean a) that other variables like supersaturation production rate and IFN availability influence F_{2B} more strongly, b) that cloud-free sulphate concentration patterns are not representative of the total sulphate concentration patterns, c) that the increase in CCN caused by sulphates masks the SIFI effect, and/or d) that winds combined to the TIC-2 development timescale cause patterns not to overlap. We have inspected the average vector field of winds at 700 mb over winter-08 and winter-09 (not shown), obtained from the NCEP/NCAR reanalysis (Kalnay et al., 1996). It appears that prevalent winds were mostly zonal along the Eurasian northern coast, had a higher northward component over the Laptev and Chukchi Seas, and exited the Arctic Ocean mostly over the western part of the Canadian Archipelago. Wind patterns at 1000 mb, 925 mb and 850 mb in the EBC sectors could roughly be described the same way. The high F_{2B} values found over the Beaufort Sea and the eastern part of the Eastern Russia sectors are then located downwind of the high $\alpha_{2/1}$ values found over Eastern Russia, in terms of the prevalent circulation during the period. At this stage, it would be premature to claim that this picture provides firm support for the SIFI effect. A numerical model simulating the development of TIC-1/2A and TIC-2B systems on the aerosol field would be needed to conclude whether the SIFI effect is required to explain the $\alpha_{2/1}$ and F_{2B} spatial

distributions. A second conclusion which may be drawn is that sulphates are not locally required in order to have a high TIC-2B fraction in the lower troposphere. Indeed, we find high F_{2B} values over North Atlantic, whereas high $\alpha_{2/1}$ values in the lowest layer are often due to the marine aerosol, with plausibly a small contribution from sea salt sulphates (the $\alpha_{2/1}$ pattern in the 1500-3000 m layer suggests that anthropogenic sulphates may relatively often reach the northern part of that sector, but that its southern part remains less polluted). Plausible explanations for North Atlantic high F_{2B} values are an important IFN deficiency in the marine aerosol (Pruppacher and Klett, 1997) and a sea salt-induced freezing inhibition effect.

GBM (2009) found a small but statistically significant correlation ($r_{Pea} \cong 0.10$) between the ice effective radius in TIC-2B tops and above-cloud α (using a different version of the index, but with a similar meaning) and argued it would have been higher had it been possible to use a proxy for in-cloud sulphate concentrations. That finding suggested that sulphates favour cloud populations made of larger ice crystals. However, the results we obtained in this study, by analysing the same correlation at a deeper level, show no evidence of a correspondence between above-cloud sulphate concentrations and cloud top r_{ie} in the EBC sectors. Moreover, they suggest that previous results were an artifact emerging from not considering the height dependence of $\overline{r_{ie}}$ and $\overline{\alpha_{2/1}}$. Without an indication that the above-TIC-2B sulphate concentrations are correlated with the in-TIC-2B concentrations, present results may not be clearly interpreted as evidence that high sulphate concentrations do not perceptibly favour cloud populations made of bigger ice crystals. In view of the limitations of interpreting the $\alpha_{2/1}$ signal in terms of sulphate concentrations when ice crystals are absent, it is unthinkable to retrieve any information about the in-cloud sulphate concentrations with the AWAC4 algorithm alone, and airborne measurements are needed for firmer conclusions. A first reason we could invoke to explain an eventual weak SIFI effect is an overestimation of the importance of the deposition mode for Arctic winter ice nucleation. The relative importance of the nucleation modes is temperature and RH_i dependent (Pruppacher and Klett, 1997), and the SIFI effect strength has likely the same dependences. Also, if the SIFI effect is important in one of the nucleation modes active at liquid saturation, it may conceivably be masked by the action of sulphates in the condensation process. Indeed, sulphate

particles contribute to increase the CCN concentration in Arctic haze, potentially counter-balancing the SIFI effect on the ice crystal number density.

An alteration of the cloud microphysical properties may have considerable climate effects. In the High Arctic, if a transfer from TIC-2A to TIC-2B occurrence is caused by the SIFI effect, it may possibly lead to the dehydration-greenhouse feedback (DGF) (Girard, Blanchet and Dubois, 2005). However, this mechanism has originally been schematized for understanding the radiative effects of (clear-sky) dehydrating diamond dust within the boundary layer (Blanchet and Girard, 1994). Because the SIFI effect is the DGF trigger, results from the present paper render unclear if the mechanism may be transposed to the free troposphere. If further research suggests it is the case, the DGF mechanism should be conceptually reformulated, notably concerning the cooling propagation, and its conditions of applicability should be specified. Even concerning the boundary layer, it has been argued by Lesins et al. (2009) that a DGF-like mechanism can hardly act in topographic sectors like the Canadian Archipelago. In such areas, clear-sky precipitating ice crystal events may occur after snow has been blown off from surrounding higher terrain tens of kilometres away, since these ice crystals may then moisten the layers they cross rather than dehydrating them (this objection does not apply over the ice-covered Arctic Ocean). Overall, it remains plausible that the SIFI effect triggers a DGF-like chain of causation involving a cooling anomaly throughout the Arctic. The strength of this perturbation must be assessed (even if this is difficult, considering that the mechanism cannot be disentangled from the myriad of other feedbacks in the Arctic climate system), because strong variations in the anthropogenic sulphate injections since the beginning of the industrial era may have implied strong surface temperature changes. If the DGF mechanism is strong, it could have caused a pan-Arctic cooling trend (the accentuation of a cooling anomaly) during most of the 20th century, as well as a warming trend since about 1990, after the European acid rain fight and Soviet industrial collapse have caused a decreasing trend in sulphate concentrations, as observed at eight monitoring Arctic stations (Quinn et al., 2007).

2.6. Conclusion

The sulphate-induced freezing inhibition (SIFI) effect, an hypothesis according to which sulphates contribute to inhibit the onset of ice crystal formation by deactivating ice

forming nuclei, has a potential consequence that may be investigated using the CloudSat and CALIPSO data sets, i.e. the idea that higher sulphate concentrations favour ice clouds made of larger ice crystals. Theoretical considerations have been used for designing a simple index (α) based on the backscattering at 532 nm (β_{532}) and the color ratio (χ) from the CALIPSO lidar measurements. After comparing winter-07 and winter-08 Zeppelin station sulphate concentrations with α averaged within a 500 km-wide and 500 m-thick box centered on the station, we believe that such an index is an appropriate proxy for the sulphate concentrations in non-cloudy probed volumes of the Arctic atmosphere, and useful for the study of the SIFI effect. Limitations include α sensitivity to misclassified clouds and other aerosol compounds, notably sea salt. We tested the SIFI hypothesis in two ways. From the distributions test, we found no evidence of a strong local SIFI effect, but argued that having higher TIC-2B (clouds supposedly favoured by the SIFI effect) fraction values downwind higher α values is consistent with a SIFI effect acting on a relatively long timescale. From the cloud top correlation test, we found practically no correlation between the ice effective radius at the top of TIC-2B and the sulphate index just above, suggesting a weak SIFI effect. However, an inescapable limitation inherent to the methodology of this test, i.e. the fact that we use an above-cloud instead of an in-cloud sulphate concentration proxy, renders the SIFI effect validation/refutation an unclosed subject. Airborne measurements of the ice effective radius and aerosol properties within ice clouds are definitively needed to obtain firmer conclusions.

Acknowledgements

PG acknowledges the Ouranos Consortium and the National Sciences and Engineering Research Council of Canada (NSERC) for financial support. The funding for this research was also supported by the NSERC through its International Polar Year 2007-2008 program. We also acknowledge the NASA Langley Research Center / Atmospheric Science Data Center from which CALIPSO data were obtained and the NASA CloudSat project. The Norwegian Pollution Control Agency (SFT) finances the monitoring program at Zeppelin, and NILU - Norwegian Institute for Air Research is acknowledged for additional support.

Figures

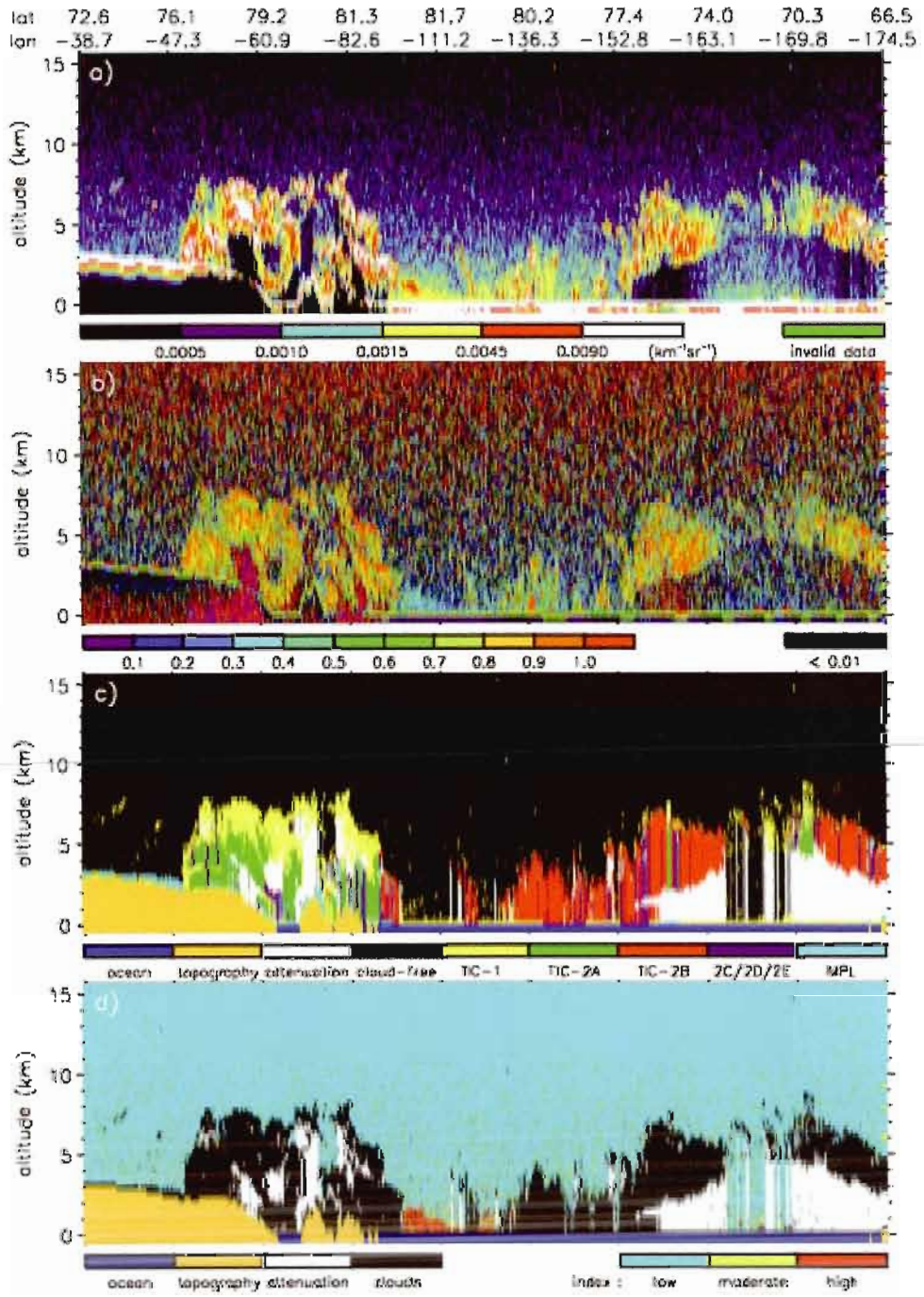

Figure 2.1: An Arctic example scene, including a) measured β_{532} (CAL-LID-L1-Prov-V2-02.2009-01-05T14-33-12ZN), b) color ratio, c) cloud classification (Cloudsat data in first kilometre above the surface are invalid, so the TIC-2 flags have been filled by extrapolating the above feature for presentation purpose only), d) aerosol index (weight ratio 2/1).

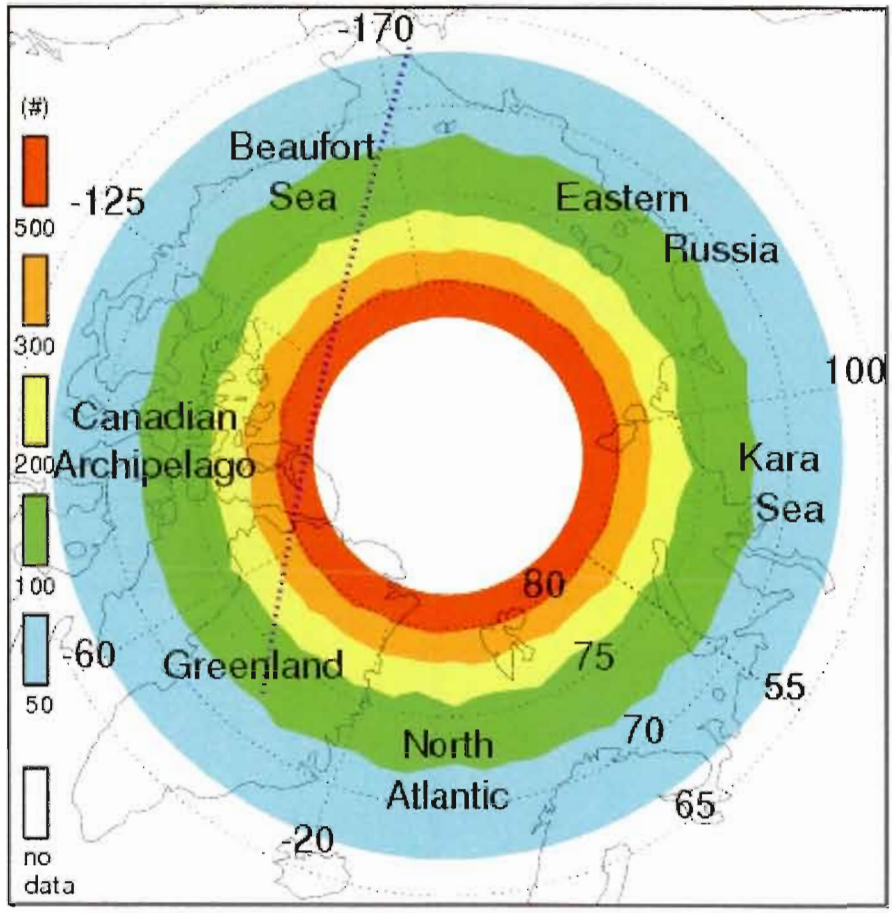

Figure 2.2: Number of trajectories crossing each 1° x 5° (lat x lon) grid box during winter-08 and winter-09. Delimitations for inner sectors referred to in the text are also shown, as well as the trajectory of the scene presented in Figure 2.1 (from Greenland to Chukotski Peninsula).

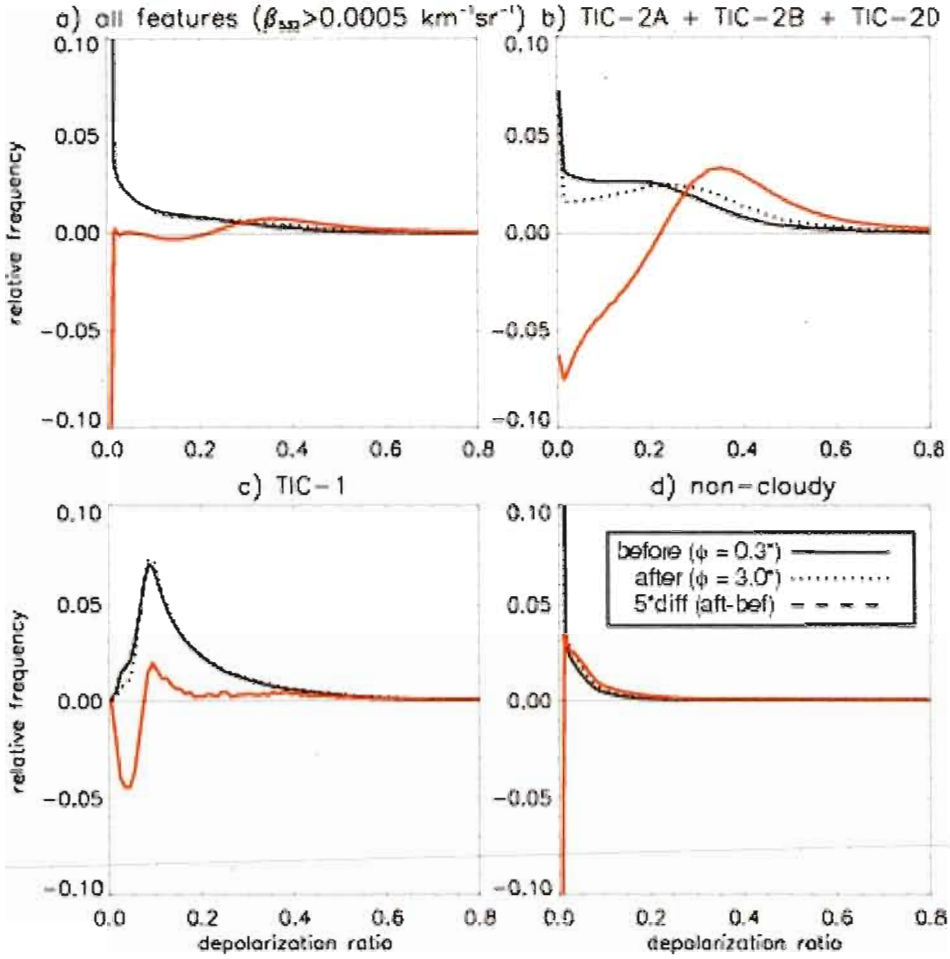

Figure 2.3: Normalized δ-distributions for a) all bins, b) TIC-2A + TIC-2B + TIC-2D, c) TIC-1 and d) haze. Thickness of the bins is $\Delta\delta = 0.01$. Differences are magnified by a factor 5, for better visual appreciation.

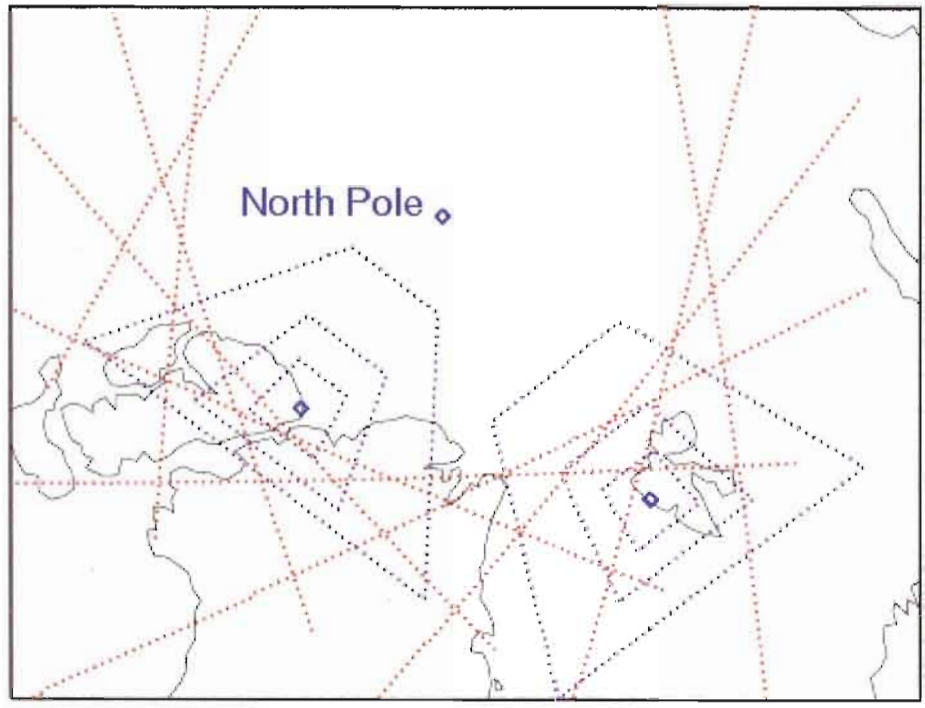

Figure 2.4: Night-time coverage around Zeppelin (left) and Alert (right) stations location, for a 24 h period (January 27th, 2007). Box sizes are 250 km, 500 km and 1000 km (side).

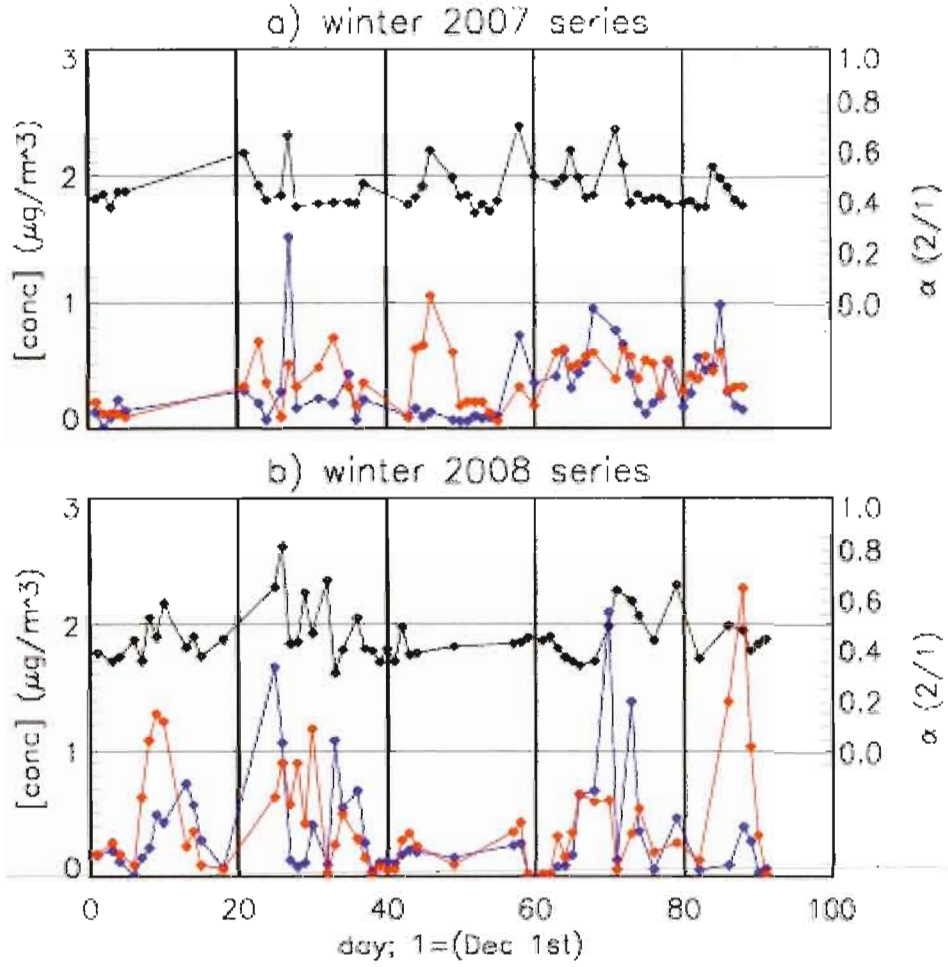

Figure 2.5: Comparison of the sulphate concentration proxy ($\alpha_{2/1}$, in black) averaged in the 500 km-wide box around Zeppelin station with in situ $[SO_4]_{tot}$ (in red) and $[Na]$ (in blue) for a) winter-07 and b) winter-08.

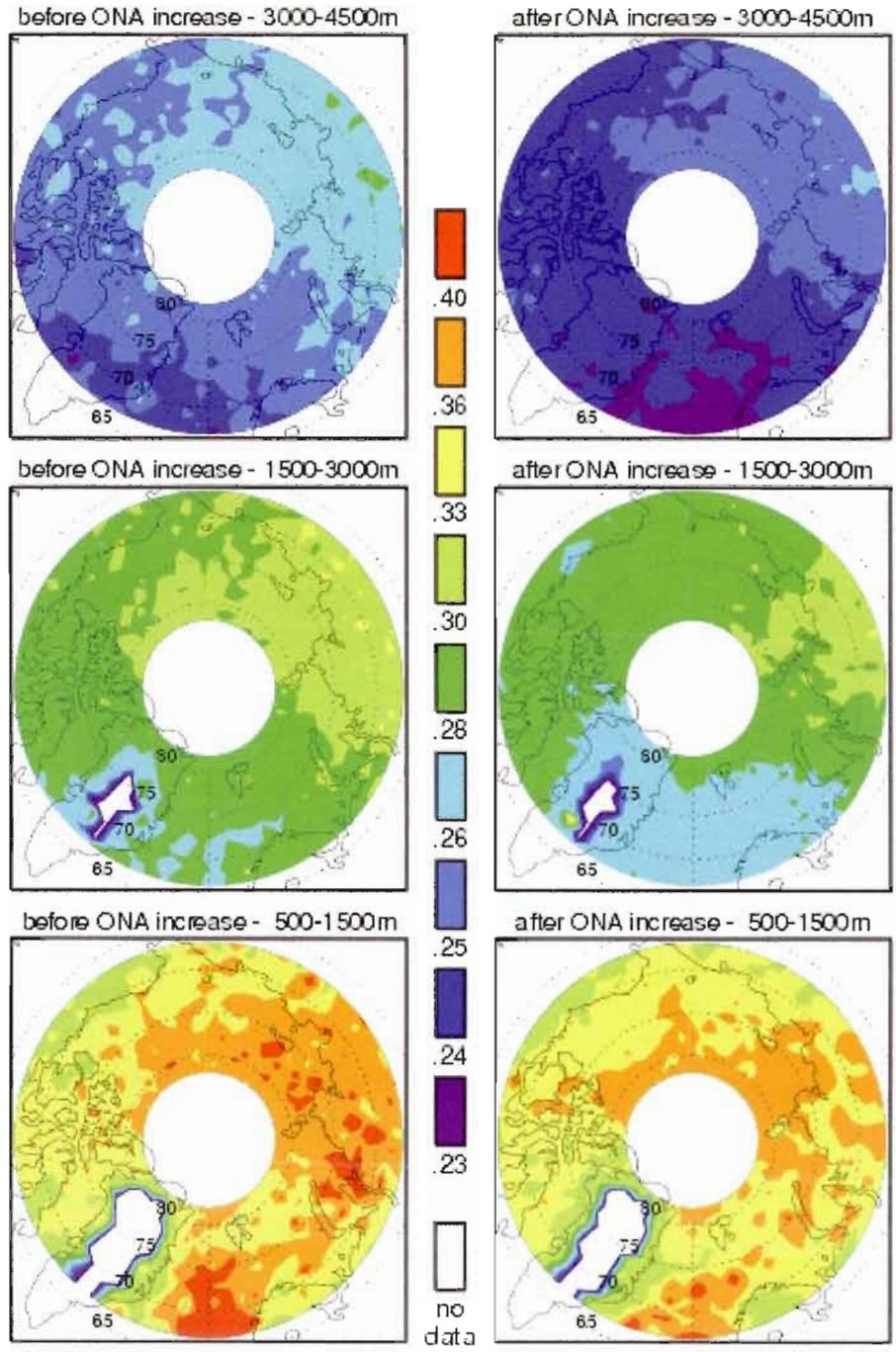

Figure 2.6: Average index ($\alpha_{2/1}$) before (left) and after (right) the ONA increase, for different layers.

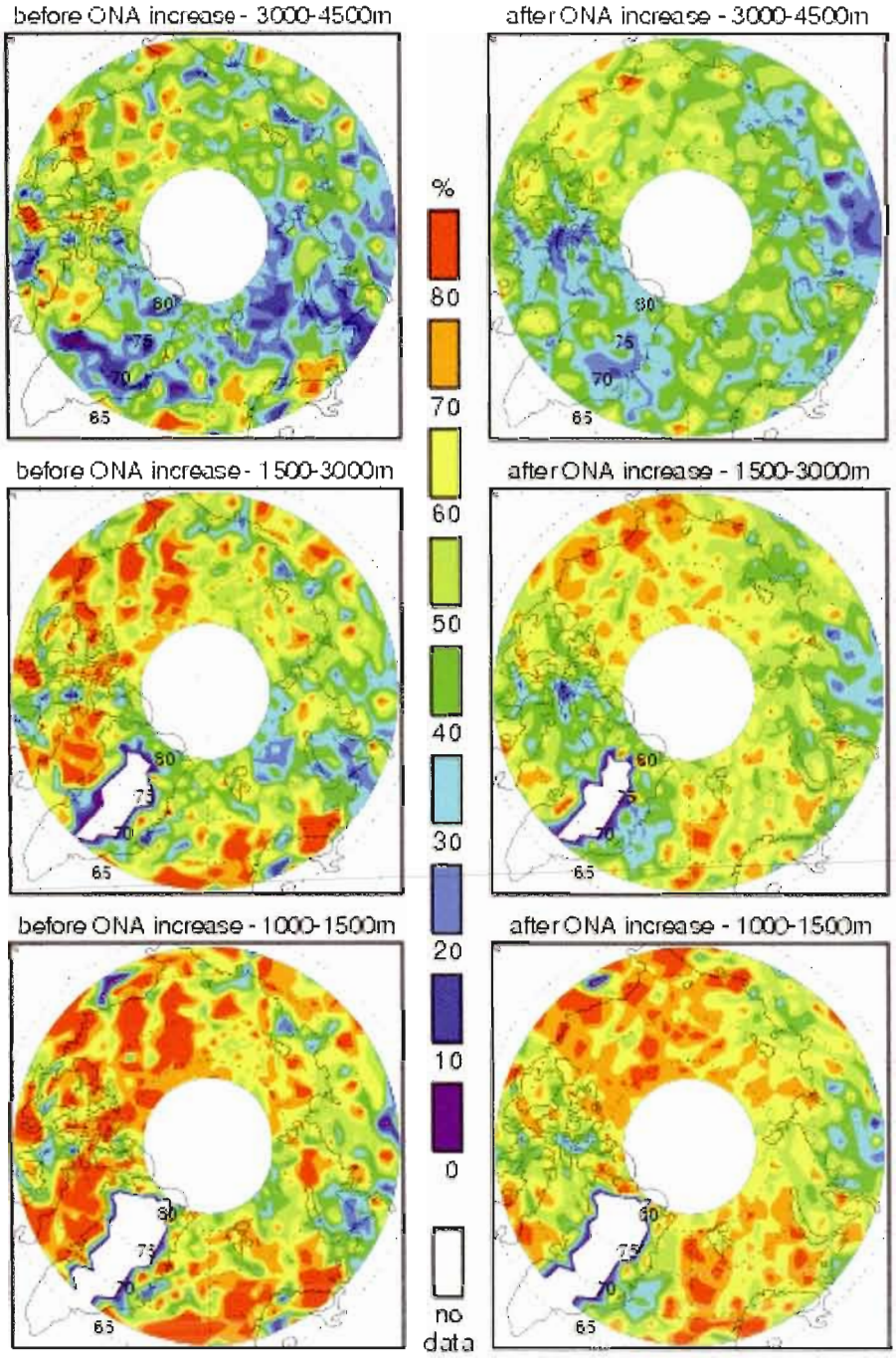

Figure 2.7: Average TIC-2B fraction (F_{2B}) before (left) and after (right) the ONA increase, for different layers.

Tables

Table 2.1: Summary of the cloud classification method.

Cloud type	Description and physical characteristics	Identification method
Mixed-phase	- Clouds with a significant liquid-to-ice ratio, possibly including liquid-only clouds. - Flat top. - Optically thick. - Small vertical extent. - Low altitude. - Temperature above homogeneous freezing point. - High color ratio ($\chi \approx 1$).	-Sharp vertical β_{532} gradient at top. - $T > -39^{o}C$ - Thickness not exceeding 1250 m.
TIC-1	- Ice clouds with small size particles, seen by the lidar only. - Small ice crystal effective radius ($r_{ie} \leq 30$ μm). - Temperature below melting point. - High color ratio ($\chi \approx 1$).	- Unseen by radar. - $T < 0^{o}C$ - Not previously identified as mixed-phase or TIC-2. - $\beta_{532} \geq \beta_{532\_min} = 0.0009$ $km^{-1}sr^{-1}$ - $\delta \geq \delta_{min} = a_0 + a_1 / \beta_{532}$ - Bin surrounded by at least one other TIC-1 bin.
TIC-2	- Ice clouds with large size particles, seen by the lidar and the radar. - High ice crystal effective radius ($r_{ie} \leq 30$ μm). - Temperature below melting point. - High color ratio ($\chi \approx 1$).	- Seen by radar. - $T < 0^{o}C$ - Not previously identified as mixed-phase.
2A	- TIC-2 under a radar-unseen cloud layer. - Covered by a TIC-1 layer.	- Important TIC-1 cover ($\Delta h \geq 800$ m).
2B	- TIC-2 whose top is seen by the radar. - Uncovered by a TIC-1 layer.	- No or small TIC-1 cover ($\Delta h \leq 320$ m).
2C	- Ice crystals precipitating below a mixed-phase layer.	- Immediately below mixed-phase.
2D	- Ambiguous thickness case.	- TIC-1 cover of intermediary thickness (320 m $\leq \Delta h \leq$ 800 m).
2E	- Ambiguous gap case.	- Less than 70 % of the minimal TIC-1 cover for having TIC-2A lay within 1200 m above the cloud top.

Table 2.2: Pearson correlation coefficient ($r_{Pea} = \sqrt{R^2}$) between in situ concentrations and proxy (α) series, with 95 % confidence intervals as obtained through Fisher's z-transformation test. The ratio above each column corresponds to the ratio of the weights given to $f(\beta_{532})$ and $g(\chi)$ in eq. 2.3, with full weight given to one term on the first and last columns. Label "all" means the whole series (105 points) are used, whereas label "sub" means sodium storms have been ignored (91 points left).

	$f(\beta_{532})$	5/1	2/1	1/1	1/2	1/5	$g(\chi)$
$[SO_4]_{tot}^{all}$	$0.20_{0.01}^{0.38}$	$0.22_{0.03}^{0.39}$	$0.23_{0.04}^{0.41}$	$0.25_{0.06}^{0.42}$	$0.27_{0.08}^{0.44}$	$0.29_{0.10}^{0.46}$	$0.30_{0.12}^{0.47}$
$[SO_4]_{nss}^{all}$	$0.10_{-0.09}^{0.29}$	$0.11_{-0.08}^{0.30}$	$0.13_{-0.06}^{0.31}$	$0.15_{-0.04}^{0.33}$	$0.18_{-0.01}^{0.36}$	$0.20_{0.01}^{0.38}$	$0.23_{0.04}^{0.40}$
$[Na]^{all}$	$0.40_{0.23}^{0.55}$	$0.40_{0.23}^{0.55}$	$0.40_{0.23}^{0.55}$	$0.39_{0.22}^{0.54}$	$0.38_{0.20}^{0.53}$	$0.35_{0.17}^{0.51}$	$0.30_{0.12}^{0.47}$
$[SO_4]_{tot}^{all}$ + $[Na]^{all}$	$0.42_{0.24}^{0.56}$	$0.42_{0.25}^{0.57}$	$0.42_{0.25}^{0.57}$	$0.42_{0.25}^{0.57}$	$0.41_{0.24}^{0.56}$	$0.39_{0.22}^{0.54}$	$0.35_{0.17}^{0.51}$
$[SO_4]_{tot}^{sub}$	$0.17_{-0.03}^{0.37}$	$0.19_{-0.01}^{0.39}$	$0.22_{0.01}^{0.41}$	$0.25_{0.05}^{0.43}$	$0.28_{0.08}^{0.46}$	$0.31_{0.11}^{0.49}$	$0.34_{0.14}^{0.51}$
$[SO_4]_{nss}^{sub}$	$0.17_{-0.04}^{0.36}$	$0.19_{-0.02}^{0.38}$	$0.21_{0.01}^{0.40}$	$0.24_{0.04}^{0.43}$	$0.27_{0.07}^{0.45}$	$0.30_{0.10}^{0.48}$	$0.32_{0.12}^{0.49}$
$[Na]^{sub}$	$0.08_{-0.12}^{0.29}$	$0.10_{-0.10}^{0.30}$	$0.13_{-0.08}^{0.33}$	$0.16_{-0.05}^{0.35}$	$0.19_{-0.01}^{0.38}$	$0.23_{0.03}^{0.42}$	$0.26_{0.06}^{0.45}$
$[SO_4]_{tot}^{sub}$ + $[Na]^{sub}$	$0.15_{-0.06}^{0.34}$	$0.17_{-0.04}^{0.36}$	$0.20_{-0.01}^{0.39}$	$0.23_{0.03}^{0.42}$	$0.27_{0.07}^{0.45}$	$0.32_{0.12}^{0.49}$	$0.35_{0.16}^{0.52}$

CHAPITRE III

MACROPHYSICAL CHARACTERIZATION OF ARCTIC WINTER MIXED-PHASE STRATIFORM CLOUDS FROM CALIPSO SATELLITE DATA

Patrick Grenier* and Jean-Pierre Blanchet

Institut des Sciences de l'Environnement, Université du Québec à Montréal

*corresponding author: grenier@sca.uqam.ca

Revised for publication in *Journal of Geophysical Review*.
Hereinafter: Grenier and Blanchet (2010b).

Abstract

The CALIPSO lidar data set is used for characterizing the macrophysical properties of Arctic winter mixed-phase stratiform (MPS) clouds. It is inferred from the backscattering at 532 nm, the depolarization ratio and the color ratio that there may exist MPS clouds consisting of a liquid top generating ice crystals which precipitate below, in agreement with other recent related studies. After investigation of data from 2108 overpasses during the winters of 2008 and 2009, we found at least one MPS layer in 39 % of the profiles and multiple layers in 6.3 % of the profiles. The minimal average thickness of the liquid layer at the top is about 100-150 meters and depends on the depolarization ratio threshold used for separating liquid from frozen cloud parcels. It is also found that the lateral extent of the MPS layers obeys a power-law distribution. MPS parcels are found up to an altitude of 8000 meters, but 95 % of the MPS parcels are located below 4500 m. All Arctic regions within the investigated domain (60°N to 82°N) may be covered by MPS clouds. Highest frequencies of occurrence are found southwest of the Svalbard Islands and west of Novaya Zemlya (> 80 %), whereas lowest values occur over Greenland and Siberia (10 to 20 %).

3.1. Introduction

Air parcels containing both liquid and frozen suspended water particles are termed mixed-phase clouds. For water devoid of soluble particles, this situation is possible between the melting point (0°C at standard pressure) and the homogeneous freezing temperature (about -39°C). Mixed-phase clouds are likely to occur at any location over the globe, and may be embedded within larger cloud systems, like for example a deeply convective cumulonimbus, in which an exclusively liquid suspended part lays beneath the mixed-phase part. In the Arctic, mixed-phase clouds often occur as a wide and relatively long-lived low-level stratiform structure generating ice crystal precipitation (Shupe et al., 2008a). These are generally thought to be advective rather than convective clouds, formed by radiative cooling of the stable air flow with a relative insensitivity to the synoptic situation (Curry et al., 1996). Frequent temperature inversions allowing for air stability (Serreze, Kahl and Schnell, 1992), along with weak or absent solar heating, render Arctic mixed-phase stratiform (MPS) clouds distinct from those at lower latitudes (Verlinde et al., 2007).

Due to the scarcity of observational sites, the macrophysical properties of MPS clouds, like geographical frequency of occurrence, seasonality, base and top heights, thickness, temperature, life duration and horizontal extent, are well documented only for a few locations and over short periods in the Arctic. During the 1997-98 SHEBA campaign in the Beaufort Sea, Shupe, Matrosov and Uttal (2006) have observed mixed-phase clouds 41 % of the time, with the highest percentage of occurrence during the spring and fall transitional seasons, and the lowest during winter (~ 5, 25 and 35 % for December, January and February, respectively). More recently, de Boer, Eloranta and Shupe (2009) have observed much lower year-round MPS frequencies of occurrence at Eureka, with 5% during winter (DJF, for December-January-February) 2006, 12 % during winter 2007, and seasonal minima during spring. Typical values for base height and thickness during DJF at Eureka are 1500-2500 m and 100-400 m, respectively, whereas the average minimal temperature is about -28°C (de Boer, Eloranta and Shupe, 2009). Concerning cloud lifetime at one site, Shupe, Matrosov and Uttal (2006) observed an average persistence of more than 12 hours during the SHEBA campaign, with one MPS cover having lasted for as long as 6.4 days.

It has often been stated that mixed-phase clouds are short-lived, due to a rapid glaciation once the ice phase is initiated (Hobbs and Rangno, 1990). One microphysical process from which this is thought to stem is the Bergeron-Findeisen mechanism, by which ice crystals grow at the expense of water droplets when relative humidity (RH) is between the saturation values with respect to ice ($> RH_i = 100$ %) and to liquid water ($< RH_w = 100$ %). Other well-known processes, like riming of droplets on falling ice crystals and ice fragmentation, should also favour a rapid glaciation and sedimentation (Pinto, 1998). However, since the two phases are often observed to co-exist for many days, other microphysical and dynamical processes must be included in water budget models of MPS clouds. Shupe et al. (2008b) have proposed a conceptual mechanism which, along with the cloud-scale convective vertical motion, could explain the maintenance of the liquid layer. In their model, the sublimation of the ice crystals (having formed during an updraft) when they fall through the sub-cloud atmosphere brings a source of moisture, which becomes usable for droplet formation in a subsequent updraft.

In addition to being oversimplified in numerical model representations, microphysical processes in MPS clouds are poorly understood (Fan et al., 2009). At the opposite of warm clouds, MPS clouds have two RH thresholds for particle formation mechanisms to act, i.e. $RH_i = 100$ % and $RH_w = 100$ %, and ice nucleation may occur via four different modes: deposition (water vapour solidifies directly on an insoluble aerosol particle known as ice-forming nuclei - IFN), contact (an external IFN touches the surface of a supercooled droplet), immersion/freezing (an external IFN gets through the droplet surface and eventually initiates freezing from inside), and condensation/freezing (the particle having initiated the condensation, or having been mixed from the beginning with the soluble material which initiated it, later acts as IFN). This traditional list of the ice nucleation modes could be extended. For example, Durant and Shaw (2005) have argued that the contact mode should be generalized to the inside-out nucleation. Also, principles behind these modes may be amalgamated, like in the deliquescent-heterogeneous freezing mode proposed by Khvorostyanov and Curry (2004), by which an insoluble particle catalyzes the freezing of a deliquescent solution before a liquid droplet could have been activated. Generally speaking, insoluble aerosol particles like clay (montmorillonite, kaolinite, illite, etc.) and soot act as ice-forming nuclei (IFN), if they contain at least one active site with a crystalline structure compatible with that of ice, whereas soluble material like sulphuric acid or sea salt consists of good cloud condensation nuclei (CCN).

The virtually infinite number of different aerosol particles (by size, shape and soluble/insoluble mixed composition) renders extremely difficult to develop a proper model for MPS formation and maintenance, since this evolution strongly depends on the number density of all IFN and CCN types. Interestingly, Prenni et al. (2007) have shown that the liquid water mass in mixed-phase clouds is very sensitive to IFN concentrations. Moreover, some soluble substances, in particular sulphates, have the potential to deactivate IFN over some temperature interval, but it is for the moment not clear in which of the nucleation modes that may occur. Laboratory experiments by Eastwood et al. (2009) have established that the deposition mode, the first which may act when an air mass cools (since $RH_i > RH_w$ for any temperature), is most certainly significantly affected. It has also been argued by de Boer, Hashino and Tripoli (2009) that the immersion mode could be impacted. Since sulphates represent the major soluble aerosol species during the Arctic winter away from the open waters (Sirois and Barrie, 1999), Grenier, Blanchet and Muñoz-Alpizar (2009) (hereinafter: GBM, 2009) refer to this phenomenon as the sulfate-induced freezing inhibition (SIFI) effect.

The aim of this study is to characterize the macrophysical properties of winter MPS clouds on the Arctic scale. For achieving this, a satellite data set must be used. The use of satellite data for gaining information about MPS clouds is not new. After analysis of the Multispectral Thermal Imager data set, Chylek and Borel (2004) have argued that the ratio of the $0.8-0.9\mu m$ and $1.5-1.8\mu m$ band radiances provides a reasonable proxy for the phase (liquid, ice, mixed) of a cloud top, based on the different refractive indices of frozen and liquid water in the second band. Data from another passive instrument, MODIS, have also been used for investigating the cloud phase, based on the brightness temperature differences among infrared bands (Spangenberg et al., 2006). These passive instruments, however, do not allow for knowing the altitude of the cloud top, for investigating the vertical cloud structure, and for detecting MPS clouds below another cloud layer. With the advent of active satellite instruments onboard CALIPSO and CloudSat, that situation is palliated to some extent. Moreover, other differences in the optical properties of water droplets and ice crystals, like the light depolarization ability, may be used. These data sets have already been used for detailed MPS cloud case studies near the Svalbard Archipelago (Gayet et al., 2009) and around Eureka, Canada (de Boer, Tripoli and Eloranta, 2008), but it is not clear if these results may be extrapolated to the

whole Arctic. The present study complements their findings about macrophysical MPS cloud properties.

3.2. Data sets

The CALIPSO satellite platform carries the Cloud-Aerosol Lidar with Orthogonal Polarization (CALIOP) instrument on the A-Train sun-synchronous orbit since spring 2006. The Nd:YAG laser is sampling the atmosphere along the satellite trajectory with 532 nm (green) and 1064 nm (near infrared) pulses at every ~ 333 meters (705 km orbit altitude, 7.5 km•sec^{-1} tangential speed, 20.16 Hz pulse repetition rate). The beam divergence of 100 μrad causes a footprint of ~ 70 meters. The horizontal resolution of the input data (V2-01 and V2-02) is 1 km, due to averaging with the 2 neighbouring profiles, whereas the vertical resolution is 30 meters for altitudes between -0.5 and 8.2 km and 60 meters between 8.2 km and 20.2 km. Hunt et al. (2009) provide more technical details about the CALIPSO mission and an assessment of the CALIOP performance.

Three channels provide information about the atmospheric features encountered by the laser beam: the total (β_{532}) and perpendicular (β_{per}) attenuated backscattering fields at 532 nm, and the total attenuated backscattering field at 1064 nm (β_{1064}). The depolarization ratio:

$$\delta \equiv \beta_{per} / (\beta_{532} - \beta_{per}) \tag{3.1}$$

corresponding to the ratio between the signal that returned to the receiver with a switched polarization and the signal which kept its initial linear polarization, consists of a proxy for the non-sphericity of the targets, and may be used to distinguish between quasi-spherical liquid droplets and irregularly shaped ice crystals (Sassen, 1991). Cloud and haze droplets, as well as gases, generally cause no or low depolarization ($\delta \approx 0$), whereas ice crystals generally show higher values. The color ratio:

$$\chi \equiv \beta_{1064} / \beta_{532} \tag{3.2}$$

corresponding to the ratio of the backscattering at two different wavelengths, is on its side generally considered as a reasonable proxy for particle size when the target has a cross section comparable to or smaller than the wavelengths (Wandinger, 2005). For larger targets, $\chi \approx 1$ or show slightly higher values. In virtue of the λ^{-4} dependance for Rayleigh scatterers (Wandinger, 2005), pure gaseous air volumes should exhibit $\chi_{molecular} \cong 1/16$ in absence of noise, whereas aerosol particles have a color ratio ranging between values for gases (low) and cloud-size particles (high) (Liu et al., 2002). These properties allow for the depolarization ratio to be used for distinguishing probed atmospheric volumes (bins) optically dominated by ice crystals, whereas the color ratio may be used for contrasting cloudy from non-cloudy bins.

An obviously important variable for cloud characterization is temperature. For this study, we use the ECMWF data interpolated on the data set grid of CloudSat, a radar-carrying platform preceding CALIPSO by 10-15 seconds on its orbit. The CloudSat radar grid is ~ 1.1 km x 240 m (horizontal x vertical). The CloudSat-retrieved cloud microphysical properties (Austin, Heymsfield and Stephens, 2009) themselves are not used here. In the latter data set, the water content is linearly split between ice and liquid water based on temperature alone, with 100 % liquid water for T > 0°C and 100 % ice water for T < -20°C. Shupe, Matrosov and Uttal (2006) have shown that this splitting method does not allow for appropriately capturing the Arctic mixed-phase clouds structure. Average values for MPS layer thickness and extent are both higher than their corresponding CALIPSO downgraded resolutions, as presented in the results section.

Before identifying and characterizing MPS layers, CALIPSO input data are submitted to a pre-treatment. The vertical and horizontal spacings are downgraded from 30 m to 60 m and from 333 m to 1.1 km, respectively, for homogeneity with data above 8.2 km in the first case and compatibility with the ECMWF data in the second case. These operations contribute to increase the signal-to-noise ratio, but the noise remains important enough for unphysical negative values to remain. To avoid dealing with such values, we set β_{532}, β_{per} and β_{1064} minimal threshold values at $\beta_{thres} = 10^{-5} km^{-1} sr^{-1}$, $0.03 \cdot \beta_{thres}$ and $\chi_{molecular} \cdot \beta_{thres}$, respectively. This operation may bias backscattering values, but since the thresholds for MPS detection and characterization are chosen by visual appreciation of the results in a trial-and-error process, this is not critical.

So far, the CALIPSO mission has provided data for three Arctic winters, with an important change in the instrumental set-up introduced in November 2007. This modification concerns the off-nadir angle (ONA) along the satellite path, which has been increased from 0.3° to 3.0° in order to improve the detection of ice crystals based on the depolarization ratio. Indeed, ice crystals tend to fall with their major axis in the horizontal (Cho, Iribarne and Richards, 1981), which causes specular non-depolarizing reflection. An ONA of at least ~ 2.5° is required for having a significant increase in δ from ice crystals (Sassen, 1991). Because δ is a central variable to the MPS clouds characterization, we only use measurements taken after the ONA increase, so that our study is limited to the winters of 2008 and 2009 (DJF – the year is that for January and February). The domain investigated is the latitude band between 60°N and ~ 82°N (the northern limit of the satellite orbit). Over that period, the data set contains 2108 Arctic overpassess, with 8 942 685 profiles into the domain (after the pre-treatment).

As the CALIPSO orbit is sun-synchronous, overpasses occur at two distinct moments during a day for a site, and these moments are not the same for two different locations. In principle, this could introduce a bias linked to the diurnal cycle. However, as we only consider polar night orbits and that the region is experiencing predominantly circumpolar circulation, it is expected that the diurnal cycle bias be weak. Polar day orbits are not investigated in this study, mainly because the threshold-based algorithm gives a different (poorer) cloud identification performance in presence of solar light.

3.3. Methodology

There exists no unique method for identifying mixed-phase stratiform (MPS) clouds using a lidar data set, since these targets contrast in many ways from their immediate environment in the β_{532}, δ and χ fields. In Figure 3.1a, we see a feature presenting a flat and highly reflective top in β_{532} imagery, between longitude tick marks -80.7°E and -98.2°E (altitude of ~ 3-4 km), and another smaller one around 164.6°E (altitude of ~ 2-3 km). The large-scale top flatness comes from the formation mechanism of these clouds which exclude strong turbulent convection, and from the top being composed of a rather long-lived population of suspended particles. The high reflectivity

of the tops, as compared to those of ice clouds, is consistent with particles being mostly small liquid droplets. Indeed, the β_{532} backscattering is proportional to the total cross-section of the particles encountered by the lidar beam, a quantity which is optimized when the water content is partaken between smaller rather than larger particles (Hogan et al., 2003). A decrease in β_{532} as the beam penetrates the cloud cannot readily be interpreted as decreases in the droplet number concentration and optical depth, since it is also known to be caused by the beam becoming more depleted. However, the two other available optical signals (δ and χ) support a vertical transition in the composition of these clouds. The color ratio (Figure 3.1b) shows a gradient spatially correlated with that of β_{532}, whereas the depolarization ratio (Figure 3.1c) starts to increase a few bins lower than β_{532} and χ do. In the case of the color ratio, we found in the literature no firm principle on which to base a separation of liquid-dominated from ice-dominated layers of a MPS cloud. However, it is known that clouds exhibit $\chi \approx 1$ (Wandinger, 2005) or even higher values, whereas smaller aerosol particles and molecules present much lower values (Liu et al., 2002). Hence, an important χ increase from a value much below 1 to a value near or above 1 is expected to accompany a sudden β_{532} increase as we run from a non-cloudy to a MPS bin, and it is generally the case for the present overpass. On its side, the depolarization ratio is known to become relatively high in presence of (non-spherical) ice crystals (Sassen, 1991), so in principle having the δ signal reaching its peak value a few bins below the strong β_{532} gradient is consistent with an ice-to-liquid ratio increase as the beam penetrates the cloud from above.

Overall, the previous qualitative analysis of the three optical signals indicates that the concerned features could be a thin liquid layer from which ice crystals form and reach precipitating size. We observe the same relationship within the three optical signals when analysing other Arctic winter overpasses. Based on the principles evoked above, we have developed the following method for detecting MPS clouds. Running downward a profile, a potential MPS cloud top bin is first detected by requiring a gradient $\Delta\beta_{532} \geq \Delta\beta_{top\_min} = 0.0060 km^{-1} sr^{-1}$ from the signal averaged within the three bins just above to its own signal averaged with that of the bin just below. Averaging before calculating the gradient decreases the probability of having a false MPS cloud top

detection, due to noise in the β_{532} field. The potential MPS cloud top bin is upgraded to the category "unsure MPS" if it satisfies $\beta_{532} \geq \beta_{\min} = 0.0060 km^{-1} sr^{-1}$ and $T \geq T_{homog} = -39^{o}C$, otherwise it is definitively downgraded to the category "no MPS". Finally, for the MPS cloud top bin to be categorized as "liquid-dominated MPS", the algorithm further requires that $\chi \geq \chi_{\min} = 0.9$ and $\delta \leq \delta_{ice\_\min} = 0.2$. Once a MPS cloud top is identified, successive bins may enter different categories: "unsure MPS" (with the $\beta_{\min}$ and T_{homog} requirements), "liquid-dominated MPS" ($\beta_{\min}$, T_{homog}, $\chi_{\min}$ and $\delta_{ice\_\min}$ requirements) or "ice-dominated MPS" (simply if $\delta \geq \delta_{ice\_\min}$). As soon as one of the successive bins cannot be classified as MPS (this sometimes happens when the attenuation of the lidar beam becomes too strong to allow for the δ signal to correctly reveal ice crystals), the algorithm continues running down the profile looking for another MPS cloud top.

Results from the application of this method to the example lidar overpass are shown in Figure 3.1d. We see that the liquid top of the MPS cloud often extends over only one bin, but sometimes over a much thicker layer. Values of the different thresholds are guided by the literature and have been chosen after application of the algorithm on various overpasses. Sensitivity of some of the final results to the depolarization ratio threshold is investigated and later discussed.

Figure 3.2 shows the average depolarization and color ratios for the MPS clouds detected by the algorithm within the 2108 Arctic overpasses. Once a liquid-dominated MPS top bin is identified, its δ and χ values are counted in the layer # -1 (whatever the altitude), and successive MPS values are registered in the appropriate layer, so that for example layer # -4 reflects the average properties of the MPS cloud between 180 m and 240 m below the top. Concerning layers # 1 and # 2, they correspond to the two non-cloudy layers just above the top. The depolarization ratio increases downward monotonically, from a top value similar to the non-cloudy ones up to values ~ 0.37 at depths of 540-600 meters. Statistics get less significant and are based on more strongly attenuated signals as we run down the clouds. The δ increase with depth has two main causes: the increase in the ice-to-liquid ratio, and the augmentation of the multiple

scattering effects (Hu et al., 2006). It is clear that the δ_{ice_min} requirement for having liquid-dominated MPS helps keeping the top bin depolarization ratio low, but this does not act on the increase at lower levels since all MPS cloud bins are then considered. The situation is similar for the color ratio, whose value for the top bin is kept higher by the χ_{min} requirement, but whose monotonic decrease down to a ~ 0.73-0.77 plateau is clear within the lower layers (depths of 420-600 meters). The χ decrease with depth is consistent with a change in the nature of the reflectors, but it is no doubt also partly due to a bias in the color ratio itself coming from a faster depletion of the β_{1064} signal than of the β_{532} one (when $\chi > 1$). Gradual δ and χ transitions render clear that the thickness of the liquid layer depends on the threshold chosen for the liquid / ice boundary. In fact, there may be ice crystals produced up to the upper boundary of the MPS cloud, as observed notably by McFarquhar et al. (2007), so that the pure liquid layer is an idealization.

After CALIPSO probed bins are attributed a MPS flag (no, unsure, liquid-dominated, ice-dominated), different statistics on macrophysical properties are calculated. Methodological details are presented together with the results. These results focus on the liquid layer, and only take into account the liquid-dominated MPS cases.

3.4. Main results

Manual inspection of the 2108 investigated Arctic overpasses shows that the algorithm allows for a reasonable characterization of the mixed-phase clouds. Some of the MPS clouds may be missed because of overlaying cloud layers depleting the lidar beam, but many cases of multi-layered mixed-phase clouds are seen. It also happens that the beam gets depleted before the precipitating ice crystals (whose existence is revealed by the CloudSat radar signal) can be detected. In these situations, the algorithm detects a predominantly liquid layer with a thickness sometimes greater than 1 km. The absence of detection of some liquid-dominated layer lower boundaries introduces a negative bias in the calculation of the thickness, which is dependent upon the different thresholds used in the algorithm.

All over the domain, the algorithm identifies at least one MPS layer in 39 % of the profiles, and a single layer in 32.3 % of the profiles. Multi-layered MPS clouds exist, being found 5.7 % (2), 0.8 % (3), 0.1 % (4) and < 0.01 % (5 layers and more) of the time. Up to 7 superposed layers have been found. These percentages are probably lower limits, since the lidar depletion constrain the detection of multiple layers. There is a slightly higher occurrence of MPS layers during December (at least one MPS layer 42 % of the time), whereas the situation is about the same for January and February (36 to 38 %). The average thickness for the liquid layer of the MPS clouds is 134 meters (2.24 bins), with a monthly minimal value of 132 m (Jan-09) and a monthly maximal value of 139 m (Feb-09). The thickest liquid layer found has a vertical extent of 1980 meters. Again, these numbers may be lower limits (for the set of parameters and thresholds chosen), since the base of the liquid layer is not found for 8.1 % of the cases for which a MPS layer top is detected (the algorithm then identifies no ice-dominated bin just below the liquid-dominated layer). This result varies within $\pm$ 1.5 % from one month to another. Another bias may come from the bin thickness (60 m) being comparable with the average thickness. The average thickness of the liquid-dominated layer depends on the δ_{ice_min} threshold, as shown in Table 1. The value obtained by setting $\delta_{ice\_min} \rightarrow \infty$ is 184 meters. This means that the algorithm produces no shift from liquid-domination to ice-domination based on the depolarization ratio. The algorithm may then stop identifying liquid-dominated bins only if β_{532}, the temperature and/or the color ratio becomes lower than its/their threshold value. Because of the depletion of the backscattering signals, 184 meters corresponds to a minimal average thickness of the (liquid-dominated + ice-dominated) MPS layer.

We also investigated the lateral extent (L) of the MPS layers. For each layer, L is determined by counting the number of successive profiles having at least one liquid-dominated MPS bin, and by filling "holes" with an extent of only one profile. The lateral extent reached in the record case 2160 km (layers that include the first or the last profile of one overpass have been ignored for this calculation). The arithmetic average is L_{avg} = 11 km, whereas the geometric average is L_{geo} = 2.8 km. The distribution, in terms of the number of counts (C) per lateral extent interval of 1.1 km, follows a power-law function,

as shown in Figure 3.3. The linear correlation between $\log(C)$ and $\log(L)$ has a Pearson coefficient $r_{Pea} = 0.976^{+0.003}_{-0.004}$ (the 95 % confidence interval is obtained through the Fischer's z-transformation test for a distribution of 827 points), for a coefficient of determination $R^2 = r_{Pea}^2 = 0.95$. From the power-law function (see Figure 3.3), we interpret that once a layer is found, the probability for it to have an extent L (relative to that of having any reference extent L_0) is:

$$P(L) = (L / L_0)^{-a} \tag{3.3}$$

with the scaling exponent a = 1.791. Ignoring layers extended over only a few profiles (which have a higher probability of spurious detection do the noise in the backscattering signals) affects only the third digit of the scaling exponent mantissa, but changes L_{avg} substantially. For example, ignoring MPS with an extent smaller than or equal to one, two and three profiles results in L_{avg} (L_{geo}) increasing to 18 (5.8) km, 25 (9.1) km and 33 (13) km, respectively.

The distribution of the liquid-dominated layers in the temperature-altitude space is presented in Figure 3.4. Colors represent the occurrence of the liquid bins for 1°C x 100 meters intervals, relative to the total number of liquid bins detected. The chiselled contours are due to the 240 meters vertical resolution of the ECMWF temperature field. Data within a band of 120 meters above ground level (agl) have been ignored, for avoiding potential surface contamination of the signal. The algorithm detects MPS clouds up to about 8000 m. These cases are however rare, 95 % of the MPS cloud bins being found below 4500 meters (this characteristic height would be lowered by considering clouds below 120 m agl). In terms of temperature, the liquid-dominated bins distribution extends above the melting point (0.4 % of all bins), for some layers below ~ 3000 meters. The three curves represent the distributions of the liquid bins within the altitude intervals 1900-2100 m, 3900-4100 m and 5900-6100 m (1°C intervals). Each curve is normalized by the total number of liquid bins in its own altitude interval, and it must be kept in mind that the algorithm detects 2 and 30 times less liquid bins at 4000 m and 6000 m, respectively, than at 2000 m. The temperature cut-off at T_{homog} = -39°C corresponds well with the end of the distribution at 2000 meters. However, at higher altitudes, the sharp

decrease from -38°C to T_{homog} suggests that the algorithm may miss some MPS clouds beyond this threshold. This could correspond to a real situation, if we consider the homogeneous freezing temperature depression due to the acidic fraction in the droplets (Bertram, Patterson and Sloan, 1996). On the other side, it could be due to the erroneous identification of liquid bins at cold temperatures due to the assumptions and the set of parameters in the algorithm. Bins below -35°C represent 1.5 % of all bins detected by the algorithm (all altitudes considered). Arithmetic average temperatures (unbiased standard deviations) of the liquid bins at 2000 m, 4000 m and 6000 m are -17.7°C (6.3°C), -26.8°C (5.4°C) and -30.5°C (4.6°C), respectively. Temperatures used for obtaining these values come from a re-analysis field (ECMWF) based on only a few measurement records in the Arctic, so we cannot exclude potential biases. However, re-analysis fields remain perhaps the best tool for a study of MPS cloud temperatures on the Arctic scale.

We present in Figure 3.5a the geographical distribution of MPS clouds occurrence. The map has been created by counting the proportion of profiles for which at least one layer was detected by the algorithm. The resolution of the grid cell is 2° x 5° (latitude x longitude), and the signal has been smoothed for better visual appreciation. Again, a band of 120 meters agl has been ignored, for avoiding potential surface contamination. Varying the height of this band between 60 and 500 meters leads to a change in the MPS cover average by only a few percents, and does not lead to a noticeable modification of the patterns. Highest occurrence values are found over North Atlantic, reaching > 80 % southwest of the Svalbard Islands and west of Novaya Zemlya. The lowest occurrences, mainly over Greenland and Siberia, are between 10 and 20 %, suggesting that MPS clouds may be found anywhere in the Arctic (from 60°N to 82°N). The high gradient in the signal found along some marine/land frontiers (e.g.: around Greenland and Ellesmere Island) could be related to the higher moisture availability over open waters, and to the fact that orographic lifting of air masses may favour the formation of other cloud types, restraining the detection of the low-level MPS clouds. On the larger scale, the pattern corresponds to the circulation "centers of action", i.e. the Icelandic and Aleutian Lows, and the Siberian and North American Highs (Serreze and Barry, 2005). This relation is likely due to higher moisture availability over open waters or to colder temperatures over Greenland and Siberia. It appears plausible that the synoptic situation plays a greater role in their formation than it has previously been thought (Curry et al., 1996), but more research is needed to deeply address this question. Patterns on the

"centers of action" scale are fairly recurrent in each of the six winter months investigated. Notably, the high MPS occurrences southwest of the Svalbard Islands and west of Novaya Zemlya are very robust features. Monthly average MPS occurrences may get under 10 % over, notably, Greenland and Siberia. Figure 3.5b shows the unbiased standard deviation among the 2^{o} x 5^{o} monthly averages. Six arrays of values are used, but for some grid cells, mainly over Siberia, there were no average value for February 2009 (no data after February 15th). The field has been smoothed, for presentation purpose. The variability is lowest notably over the Laptev Sea, North Atlantic and Greenland, whereas it is highest notably over the Baffin Bay and the Chukchi Sea. Grid cells having a better satellite coverage (this variable increases northward) generally present a lower standard deviation, so we expect that the consideration of further winter months would decrease the signal variability.

3.5. Concluding remarks

The present macrophysical characterization of the Arctic mixed-phase stratiform (MPS) clouds reinforces the traditional description according to which they consist of a vertically thin liquid layer generating ice crystal precipitation. The top β_{532} sharp gradient and flatness are consistent with the upper part of these clouds being made of rather small suspended particles, i.e. droplets. Moreover, the marked changes in the color and depolarization ratios with depth (from the top) are consistent with a change in the nature of the reflectors, especially with an increase in the non-sphericity, hence in the ice-to-liquid ratio. However, it must be kept in mind that an increase in the multiple scattering with depth may mimic this effect. The decrease in the color ratio with depth is harder to explain, since for scatterers much larger than the size of the lidar wavelengths, the size dependency of the color ratio no longer holds. This is the case for both droplets and ice crystals, which as water particles can be discriminated from aerosol particles and gaseous reflectors, but not one from the other. The thickness of the liquid layer at the top consists of a heuristic concept in the characterization of the MPS clouds, since it depends on the liquid/ice splitting threshold (δ_{ice_min}) and ice crystals may be produced throughout the whole MPS cloud. However, speaking of a liquid-dominated layer with an average thickness of at least 100-150 meters seems a reasonable assertion. Because of the lidar beam depletion throughout the MPS clouds, we have limited information on the

precipitating ice crystals. Otherwise, an interesting finding would have been the percentage of these ice crystal populations which fall but sublimate before reaching the ground (virga). According to Fan et al. (2009), the sublimation of ice particles could provide a significant source of IFN and be needed for explaining the persistence of MPS clouds.

With an average of 39 % all over the domain, the MPS cloud occurrences that we find may seem high as compared with previous results obtained at Eureka (de Boer, Eloranta and Shupe, 2009) or over the Beaufort Sea (Shupe, Matrosov and Uttal, 2006). However, on Figure 3.5, the top panel shows there is substantial spatial heterogeneity over the investigated domain (with smaller values notably over the Canadian Archipelago, where local effects due to the topography may also be important), whereas the bottom panel suggests that differences from one year to the other at some locations may be quite substantial (notably off the Alaskan coast).

The information gained by this study may eventually guide the investigation of the sulfate-induced freezing inhibition (SIFI) effect, defined in the introduction section. For the SIFI impact on MPS clouds to have a climatic importance, we expect both the MPS clouds occurrence and the average sulfate concentrations to be high. From the present study and that of Grenier and Blanchet (submitted to JGR), who investigated the geographical distribution of a sulphate concentration proxy within the Arctic lower troposphere, the Kara Sea appears as a region satisfying these two conditions. Over North America, we note a higher MPS clouds occurrence over Barrow, Alaska than over Eureka, Canada, which renders the former site more attractive for aircraft campaigns dedicated to the study of the SIFI effect. One motivation for studying Arctic MPS clouds microphysical alterations stems from their significant influence on the surface climate, the sea ice thickness and the dynamics (Harrington and Olsson, 2001), among others.

Acknowledgements

The funding for this research was supported by the NSERC through its International Polar Year 2007-2008 program. We also acknowledge the NASA Langley Research Center / Atmospheric Science Data Center, from which CALIPSO data were obtained, and the NASA CloudSat project.

Figures

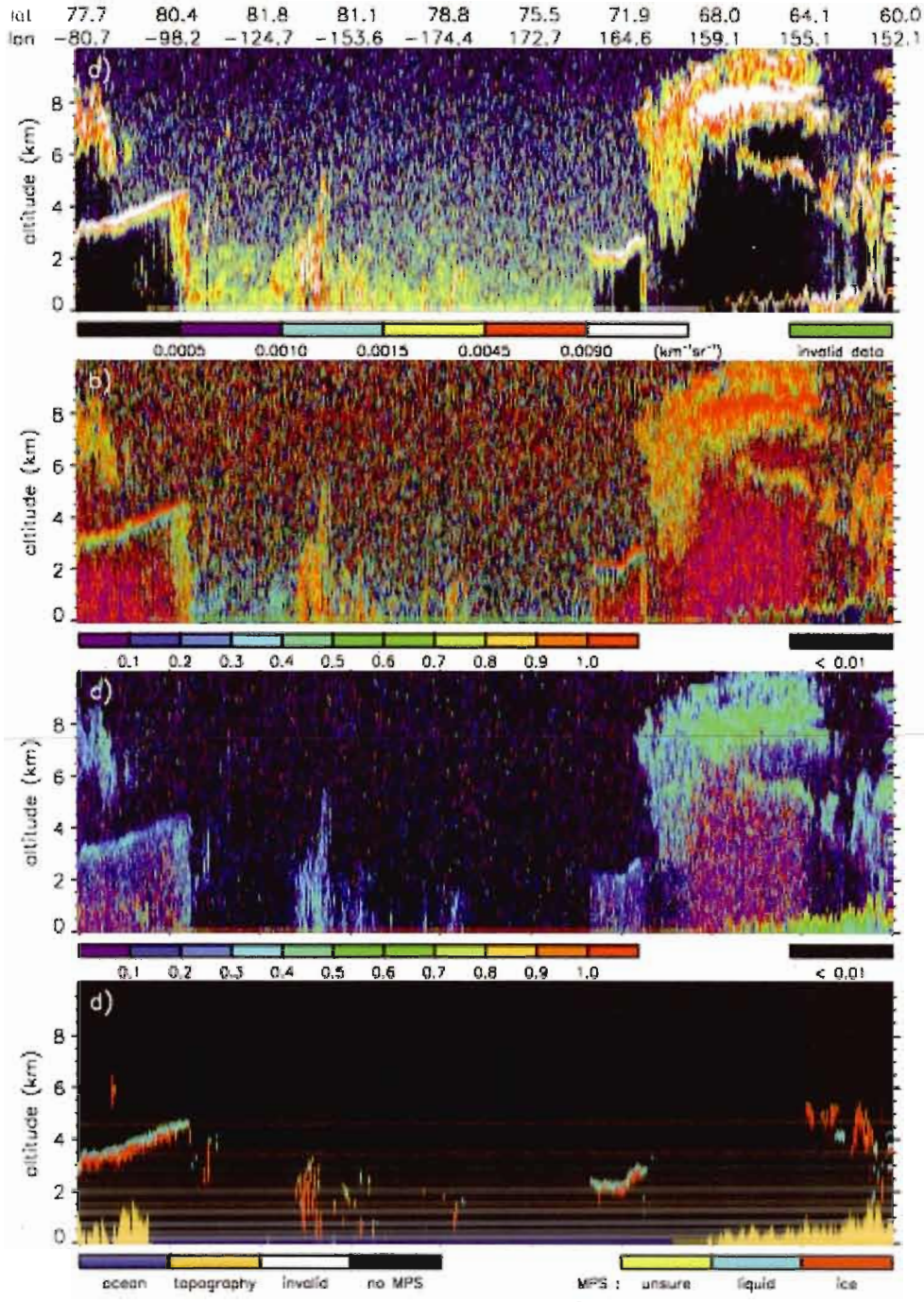

Figure 3.1: An Arctic example overpass, including a) measured β_{532} (CAL-LID-L1-Prov-V2-01.2008-02-02T16-22-26ZN), b) color ratio, c) depolarization ratio, and d) MPS classification.

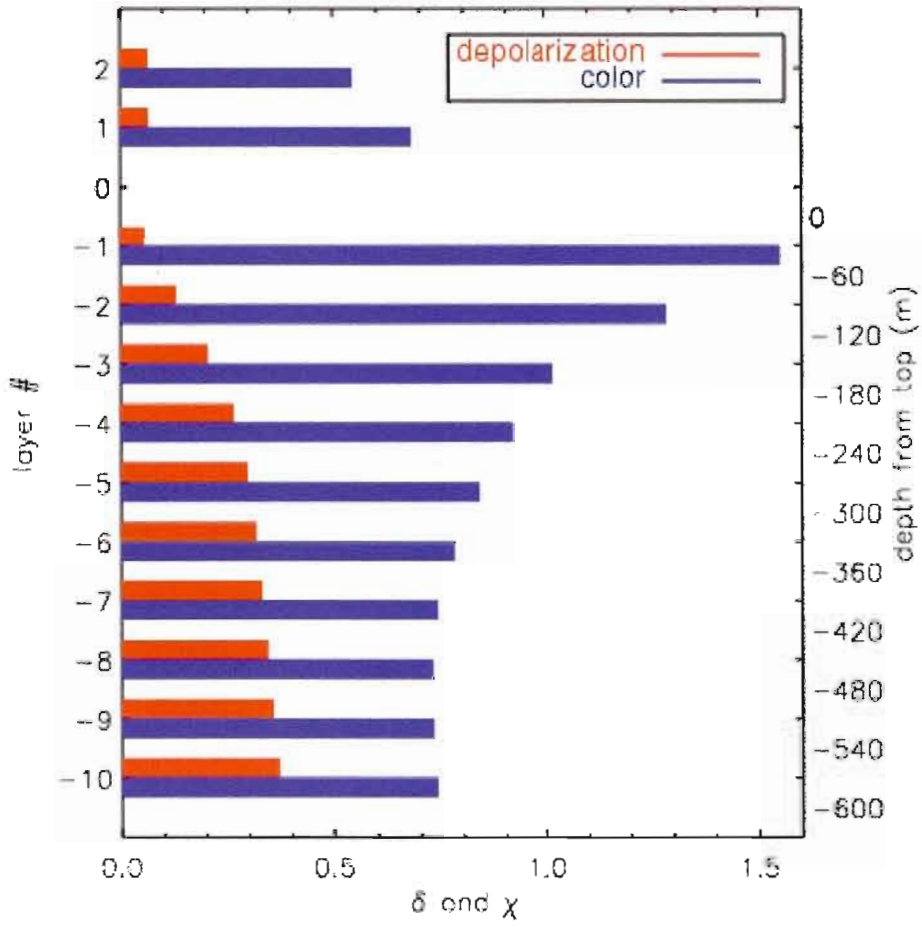

Figure 3.2: Average depolarization (red) and color (blue) ratios for 60 m-thick layers. Layer # -1 is the top layer, whereas layers # 1 and # 2 correspond to the non-cloudy zone just above the top.

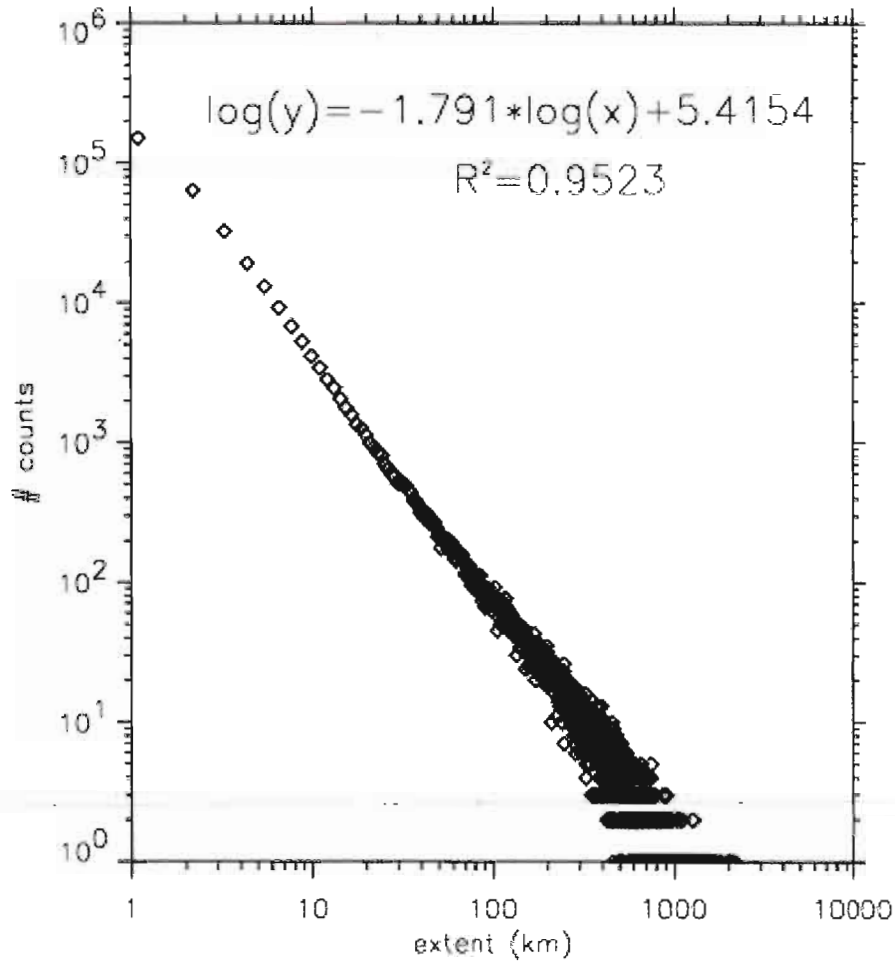

Figure 3.3: Number of counts per 1.1 km interval for MPS cloud extent, with the related power-law function and coefficient of determination.

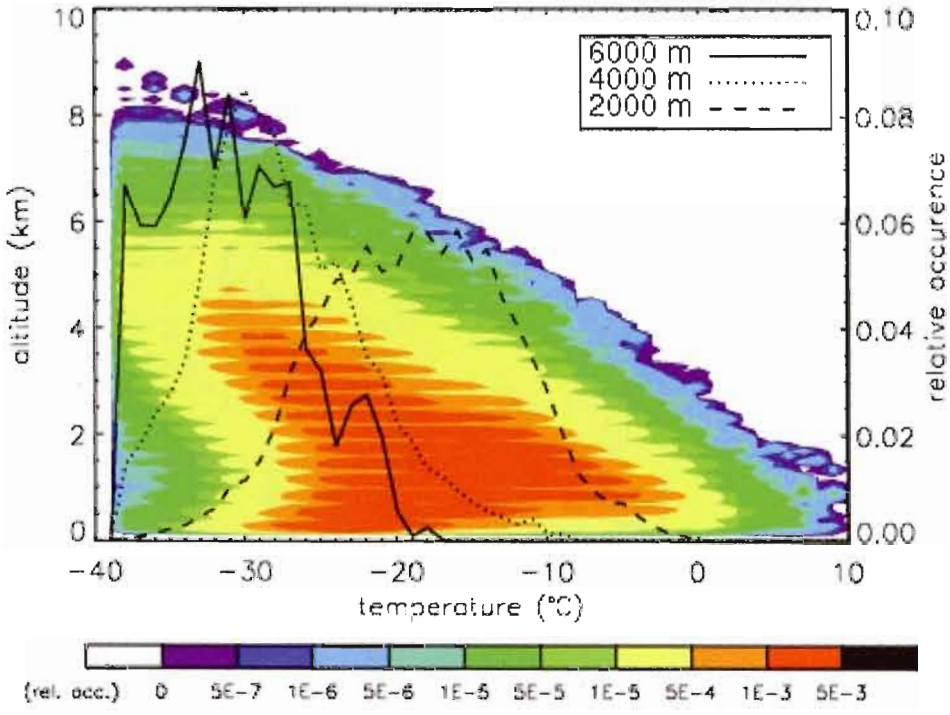

Figure 3.4: Distribution of the liquid bins in the temperature (1°C intervals) versus altitude (100 meters intervals) space, with temperature distributions for three specific altitudes. A band of 120 m agl is ignored.

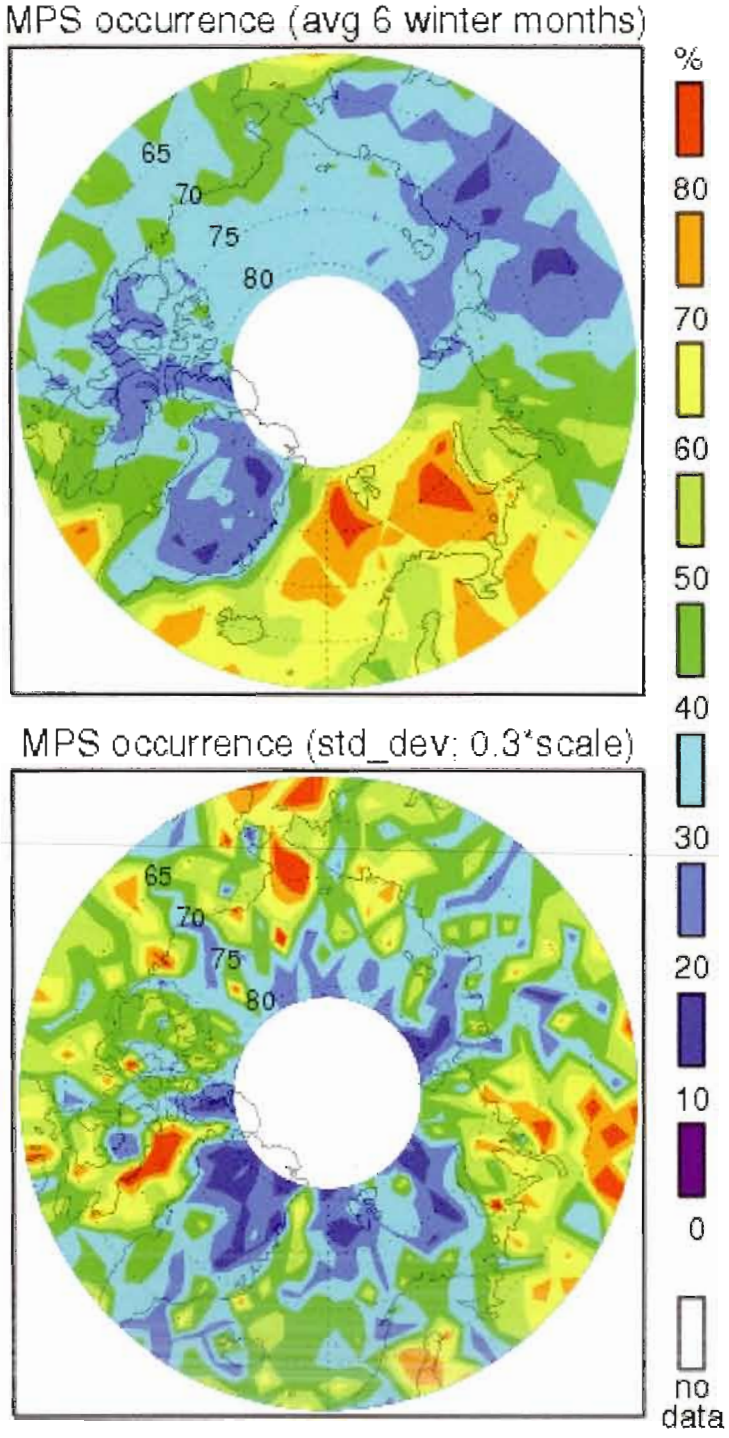

Figure 3.5: Geographical distribution of MPS clouds occurrence (2° latitude x 5° longitude grid cells), with a) the average from all profiles over six winter months, and b) standard deviation among the monthly averaged values (the scale on the right must be multiplied by 0.3 for reading standard deviations values). A band of 120 m agl is ignored.

Tables

Table 3.1: Average thickness (Δh) of the MPS top liquid layer as a function of the depolarization ratio threshold (δ_{ice_min}).

δ_{ice_min}	Δh (meters)
0.05	87
0.10	110
0.15	125
0.20	134
0.25	141
0.30	148
0.35	156
0.40	164
0.45	171
0.50	176
$\rightarrow \infty$	184

CONCLUSION GÉNÉRALE

Justification des orientations de recherche

Cette section traite de comment nos motivations et nos découvertes nous ont conduits à effectuer nos recherches selon l'ordre correspondant aux trois articles (chapitres). Des commentaires ainsi que certaines conclusions qui n'ont pas été intégrées aux articles sont aussi présentés.

Suite à une analyse préliminaire des premières données de CloudSat et CALIPSO, trois constats nous ont conduits à réorienter le projet, qui consistait initialement à étudier le mécanisme RDES dans les nuages en phase mixte de la couche limite, soit environ dans le premier kilomètre agl (*above ground level*). Le premier constat vient de ce que Kahn et al. (2007) ont estimé que la sensibilité du radar est grandement affectée dans le premier kilomètre agl, due à une contamination de surface liée à la grande longueur du pulse du radar, soit 1000 mètres. Ainsi, chaque fois que le faisceau du lidar est atténué avant d'atteindre 1000 m agl, il est impossible de déterminer s'il y a des particules dans la zone concernée. Les produits d'inversion de CloudSat (contenus massiques, rayons effectifs et concentrations en nombre des phases liquide et glacée) sont donc disponibles sans données pour la couche limite. Le second constat pour lequel nous avons réorienté le projet vient de ce qu'il nous a semblé, suite à la visualisation de nombreuses scènes produites par CALIPSO, que les systèmes nuageux au sommet à la fois vu par le radar (à rayon effectif élevé) et en dents-de-scie (indice d'une précipitation) se développaient préférentiellement dans des zones dont les volumes apparemment non nuageux présentaient une rétro-diffusion lidar plus élevée. Cela rendait ces systèmes nuageux intéressants pour l'étude de l'effet IGIS. Enfin, compte tenu de la nature des différents champs physiques mis à notre disposition, il s'est avéré plus difficile que prévu, voire impossible, de développer une méthodologie appropriée pour tester le mécanisme RDES dans son ensemble, du moins sans l'utilisation d'un modèle

numérique. Pour toutes ces raisons, nous avons décidé de concentrer le projet sur la recherche d'une signature de l'effet IGIS seulement, et ce dans la troposphère libre.

L'effet IGIS implique principalement deux entités, soient un champ de sulfates qui affecte un couvert nuageux. La première étape de notre travail a donc consisté à élaborer une méthode de détection des nuages, et à cerner ceux pour lesquels nous avions des raisons de croire qu'ils pourraient être les plus affectés par l'effet IGIS. La seconde étape a consisté, naturellement, à proposer un indice (proxy) pour les sulfates. Enfin, comme troisième étape, les deux entités ont pu être mises en lien via des calculs de corrélation. Les trois paragraphes qui suivent complémentent l'information présentée par Grenier, Blanchet et Muñoz-Alpizar (2009) (ci-après: GMB, 2009), pour chacune des trois étapes énumérées.

La classification des nuages utilisée par (GBM, 2009) ne correspond en rien à la classification traditionnelle proposée par le pionnier de l'étude des nuages Luke Howard (Howard, 1865). La raison en est que les types de nuage que nous souhaitions mettre en évidence diffèrent selon un critère qui ne participe pas de cette classification traditionnelle, soit la taille des cristaux de glace du sommet des nuages. L'effet IGIS ne pouvant être testé directement par l'utilisation de mesures satellitaires ayant des résolutions de l'ordre de $(\sim 100\ m)^3$, nous avons décidé de tester son corollaire (dans le mécanisme RDES) selon lequel les plus grandes concentrations en sulfates favorisent les couverts nuageux faits de cristaux à plus grand rayon effectif et augmentent ainsi la proportion de nuages glacés de type TIC-2B, dont le sommet présente un rayon effectif supérieur à ~ 28-30 μm. Cette valeur correspond à la limite de détection du radar et s'impose donc de façon arbitraire dans notre méthodologie. Cependant, il nous apparaît fort probable qu'un changement de cette valeur pour une autre dans l'intervalle ~ 10-100 μm aurait procuré des résultats dont l'interprétation en termes de l'effet IGIS aurait été similaire, puisque c'est l'existence du seuil dans l'intervalle de rayons effectifs des particules de nuage qui importe. La principale raison pour laquelle nous avons séparé les TIC-2B des systèmes TIC-1/2A réside dans ce que les plus fortes valeurs de sursaturation atteintes dans ces derniers systèmes (selon notre conception de leurs mécanismes de formation) permettent d'activer une tranche supplémentaire de NG (dû à l'effet de dépendance à la taille de la nucléation), ce qui peut contribuer à masquer l'effet IGIS. De façon pratique aussi, l'absence d'une valeur de rayon effectif pour les TIC-1 (non

détectés par le radar) empêche de procéder aux calculs de corrélations entre cette variable au sommet du nuage et l'indice d'aérosol juste au-dessus. Il est cependant important de comprendre que l'effet IGIS affecte potentiellement tous les types de nuage comportant des cristaux. Enfin, concernant la séparation entre les TIC-1 et les couches d'aérosol denses, nous présentons sur la Figure C-1 la fonction de séparation (δ_{min}) dans l'espace δ versus β_{532}. La distribution exclut les TIC-2, les nuages en phase mixte et les zones dites de saturation (sous les nuages), laissant ainsi deux maxima d'occurrence, correspondant l'un aux TIC-1 et l'autre aux aérosols, et qui se superposent partiellement.

Il est inconcevable, à partir des bases de données de CloudSat et de CALIPSO, de déduire par des principes physiques la concentration en un type précis d'aérosols dans une parcelle d'air sondée, à plus forte raison si celle-ci contient des particules de nuages, ces dernières contrôlant les signaux de rétro-diffusion et de réflectivité. Nous concevions donc, avant même de penser à la fonction de notre indice d'aérosol (α), que celui-ci représenterait au mieux un proxy de la concentration en sulfates, c'est-à-dire une quantité qui varie seulement de façon générale avec $[SO_4]$, sujette au bruit et sensible de surcroît à d'autres particules atmosphériques. Cet indice est basé sur les principes généraux selon lesquels les aérosols du mode d'accumulation font d'une part augmenter β_{532} par rapport aux molécules et d'autre part diminuer χ par rapport aux nuages. Malgré les limites (bien décrites dans les deux premiers articles) de ce proxy, il s'avère heuristique dans le sens où nous ne disposons pas d'alternative pour cerner les sulfates dans les champs de CALIPSO. Après la publication du premier article, nous avons été questionnés concernant la signification physique de cette variable. À ce moment, nous n'avions procédé à aucun exercice de calibration de α sur des mesures de concentration en sulfates, et nous interprétions sa valeur (bornée par 0 et 1) comme une probabilité qu'il y ait présence significative de sulfates dans la parcelle d'air sondée. Malgré le caractère imprécis de ce proxy, nous avons de bonnes raisons de croire que cette interprétation est raisonnable. D'abord, comme en témoigne la Figure C-2, la distribution des parcelles non-nuageuses, à l'allure gaussienne à 6000 m d'altitude, se scinde en deux de façon de plus en plus nette à mesure que l'altitude décroît, en accord avec la propagation, dans la basse troposphère, de brume arctique dans un *background* à plus faibles concentrations en aérosols. Par ailleurs, les valeurs moyennes de α plus faibles au-dessus de l'Antarctique que de l'Arctique, plus faibles au-dessus des secteurs Groenland-Atlantique Nord-Mer de Kara (GNK) qu'au-dessus des secteurs Russie Orientale-Mer de Beaufort-Archipel

Canadien (EBC) et décroissantes avec l'altitude sont cohérentes avec la distribution des sulfates aux pôles telle que décrite dans la littérature en général.

Deux types de corrélations concernant les TIC-2B et l'indice d'aérosols ont été explorés par GBM (2009). Dans un premier temps, nous voulions savoir si les secteurs contenant les plus fortes proportions de TIC-2B (en pourcentage du couvert nuageux total) correspondaient à ceux contenant les plus hautes valeurs moyennes de α. La Figure C-3 suggère que c'est en général le cas, autant à 1500 m qu'à 4500 m d'altitude. Considérant les 11 secteurs de l'étude, les coefficients de détermination (R^2) de la corrélation linéaire sont en effet positifs aux deux niveaux d'altitude, avec des valeurs respectives de $R^2 = 0.54^{0.86}_{0.06}$ et $R^2 = 0.61^{0.88}_{0.12}$ (intervalles de confiance à 95 %). Considérant les seuls 6 secteurs arctiques, les coefficients demeurent élevés, soient $R^2 = 0.72^{0.97}_{0.01}$ et $R^2 = 0.54^{0.94}_{-0.04}$, respectivement. Cependant, la corrélation ne tient pas lorsque seuls les 5 secteurs de l'Antarctique sont considérés ($R^2 = 0.01^{0.81}_{-0.73}$ aux deux niveaux). Une raison évocable pour expliquer ces faibles valeurs est l'absence d'événements de brume sèche en Antarctique, qui confine les valeurs moyennes de α à un petit intervalle correspondant au *background* d'aérosols. Dans ce cas (des secteurs antarctiques pris isolément), le calcul de R^2 peut donc plus difficilement être interprété comme un test du corollaire de l'effet IGIS selon lequel les plus fortes valeurs de concentrations en sulfates favorisent les couverts nuageux à plus larges cristaux, puisque l'on n'observe pas ces fortes valeurs. Dans un second temps, nous avons calculé la corrélation entre le rayon effectif des cristaux au sommet des TIC-2B (en moyennant sur les 720 mètres supérieurs) et l'indice d'aérosols au-dessus (moyenne sur 1440 mètres juste au-dessus du sommet du TIC-2B). Les coefficients de corrélation linéaire (coefficients de Pearson) obtenus sont de l'ordre de $r_{Pea} \approx 0.10$, pour un coefficient de détermination linéaire $R^2 \approx 0.01$.

Les conclusions auxquelles GBM (2009) sont parvenus commandaient d'une part un approfondissement de l'étude de l'effet IGIS, puisque les deux types de corrélations obtenues entre les valeurs de l'indice d'aérosols et certaines propriétés des TIC-2B apparaissaient cohérentes avec cet effet, et d'autre part un examen plus rigoureux de celui-ci, puisque beaucoup de suppositions et de simplifications avaient dû être introduites dans la méthodologie. Nous avons donc, pour le second article, a) concentré nos recherches sur l'Arctique, b) redéfini l'indice d'aérosol, c) acquis des données in situ

pour valider cet indice en tant que proxy de la concentration en sulfates, d) basé le seuil pour la détection de brume arctique sur des données in situ, e) ajouté des catégories de TIC-2 « ambiguës », f) introduit la variable F_{2B}, g) redéfini certains paramètres de l'algorithme, h) augmenté les statistiques en élargissant la base de données satellitaires à 9 mois, i) étudié l'effet du changement de l'angle de visée du lidar avant le second hiver, et j) augmenté la résolution spatiale de notre étude à 1° x 5° (latitude x longitude) au lieu d'étudier les champs par secteurs. Dans les paragraphes suivants, nous commentons ces différentes modifications, qui ont permis de pousser l'analyse de l'effet IGIS à un niveau plus satisfaisant que celui atteint par GBM (2009).

Point a). Un des résultats importants de GBM (2009) est celui qui montre qu'il n'y a pas dans l'Antarctique de secteurs qui se démarquent, soit par de plus hautes valeurs de l'indice d'aérosol dans la troposphère ou de fréquence de brume arctique, soit par une plus grande fraction de TIC-2B dans le couvert nuageux, alors que dans l'Arctique les secteurs Russie orientale / Mer de Beaufort / Archipel Canadien (EBC) se démarquent des autres par rapport à ces variables. Ainsi, il apparaissait clairement que si l'effet IGIS avait un impact notable quelque part, ce serait dans les secteurs EBC de l'Arctique. Nous avons donc décidé de concentrer nos efforts suivants sur l'Arctique, et même sur les seuls secteurs EBC pour les nouveaux calculs de corrélation.

Point b). La première version de l'indice d'aérosols, basée sur des principes généraux qui devaient faire correspondre les plus hautes valeurs de α à des petits objets hautement rétro-diffusants, révèle des particules polaires se retrouvant préférentiellement dans les secteurs EBC de l'Arctique. Puisque nous savions par d'autres sources (AMAP, 1998) que les sulfates se retrouvent préférentiellement dans ces secteurs, nous considérions que malgré son design primitif cet indice était lié aux sulfates. Cependant, un défaut majeur, qui aurait pu être corrigé avant la publication par GBM (2009), venait de ce que le terme de ratio de couleur dans l'équation 1.2 permettait aux molécules, qui présentent en principe une valeur de ratio de couleur centrée sur $\chi_{molecular} \approx 1/16$ (Wandinger, 2005), de biaiser considérablement le sens de α en l'absence d'autres particules pour dominer le signal. Ce biais était limité par le bruit élevé dans les signaux β_{532} et β_{1064}, et a été corrigé dans la seconde version de l'indice (voir équation 2.3). La Figure C-4 montre bien que le second terme n'y est plus sensible à la valeur $\chi_{molecular} \approx 1/16$. Il a aussi été décidé que le seuil β_{532} serait une constante plutôt qu'une fonction de

l'altitude. Par ailleurs, l'étude de la sensibilité de l'indice au ratio de poids w_β / w_χ constitue une voie d'approfondissement de notre analyse.

Points c) et d). L'indice α constituant une variable non conventionnelle en climatologie, nous nous devions de tenter de le valider. Malheureusement, aucun appareil pouvant fournir une information directe sur la concentration en sulfates ne sonde une parcelle d'air au même moment que le lidar de CALIPSO ne le fait. Ainsi, nous nous retrouvions contraints d'utiliser les données de stations au sol dont l'emplacement est rarement compris dans l'empreinte (*footprit*) du faisceau lidar, et les données sont fournies après avoir été moyennées sur des périodes relativement longues, par exemple 24 heures dans le cas de Zeppelin. Nous savions donc que la variabilité spatio-temporelle du champ de sulfates peut conduire à de fausses conclusions sur la validité ou non de l'indice. De plus, la seule des quatre stations arctiques dont nous avons pu en bout de ligne utiliser les données (Zeppelin Mountain, dans l'Archipel des Svalbard) est la plus exposée aux embruns, dont les particules de sel de mer peuvent aussi faire augmenter la valeur de l'indice. Néanmoins, l'exercice de validation a montré d'une part que les substances solubles sur lesquelles peuvent se développer des solutions à volume sphérique (sulfates et sels de mer) peuvent expliquer une bonne partie de la variation de α, et d'autre part qu'en conditions de faibles concentrations en sel de mer, un pic de concentration en sulfates à Zeppelin Mountain peut se refléter dans un pic de α moyenné dans une zone de 500 km de côté centrée sur cette station. La méthodologie employée pour valider α permet aussi de déterminer un seuil pour détecter les événements de brume arctique. Nous croyons enfin que s'il était possible de mesurer les concentrations moyennes en sulfates dans toutes les parcelles d'air sondées par le lidar, l'exercice de validation démontrerait que α est un excellent proxy pour cette quantité, loin de l'influence des aérosols marins.

Points e), f) et g). La prise en compte de cas ambigus de TIC-2 dans la classification des nuages permet de sélectionner les TIC-2B et TIC-2A qui correspondent le mieux aux deux mécanismes de formation que nous mettons en opposition. Quant à la variable F_{2B}, correspondant à la fraction de TIC-2B parmi l'ensemble (TIC-2B + TIC-2D + TIC-2A), elle est plus pertinente que la proportion de TIC-2B (parmi tous les nuages) que nous avons utilisé pour le premier article. En effet, l'effet IGIS tel que nous le concevons et le décrivons est censé causer un transfert des TIC-2A vers les TIC-2D (cas

ambigu par l'épaisseur intermédiaire du sommet TIC-1) et de ceux-ci vers les TIC-2B, tous des nuages convectifs. Cependant, il est peu probable que l'effet IGIS transforme des nuages en phase mixte / TIC-2C, surtout formés de façon advective (Curry et al., 1996), en TIC-2B, même s'il les affecte potentiellement aussi. Les nuages TIC-2E n'ont pas été considérés dans la variable F_{2B}, parce qu'il est généralement difficile d'interpréter, d'après les configurations nuageuses qui les incluent, s'ils sont de nature convectives ou pas. Cet élargissement de la classification des nuages, ainsi que la modification de l'angle de visée du lidar de CALIPSO, ont conduit à modifier de nombreux seuils et paramètres de l'algorithme. Le choix de ceux-ci a été fait, tout comme dans la première version de l'algorithme, par essai et erreur sur de multiples scènes, en évaluant entre autres leur capacité à cerner des structures établies visuellement dans les coupes des champs β_{532} , δ, χ, et r_{ie}.

Points h), i) et j). En basant notre première étude de l'effet IGIS dans l'Arctique sur les données d'observation satellitaire du seul mois de janvier 2007 (386 scènes), la force de nos conclusions était limitée d'une part par la difficulté à identifier les TIC-1 dû à l'orientation du lidar vers le nadir (déviation du nadir de 0.3° avant la fin de novembre 2007, comparativement à 3.0° après cette date), et d'autre part par l'ignorance du degré auquel ce mois représente l'hiver arctique. En accumulant les statistiques sur 9 mois (3143 scènes), nous parvenons à des conclusions plus fermes.

Le dernier article constituant cette thèse (Grenier et Blanchet, 2010b) ne rapporte pas un test de l'effet IGIS, mais plutôt une caractérisation des nuages stratiformes en phase mixte (NSPM), aussi potentiellement affectés par cet effet. La motivation pour effectuer cette caractérisation vient d'une part de ce que nous avions atteint une certaine limite dans l'approfondissement de l'étude de l'effet IGIS dans les nuages glacés à partir des seules données de CloudSat et CALIPSO, et d'autre part d'une publication récente par de Boer, Hashino et Tripoli (2009), qui ont argumenté que le mode d'immersion/gel fournit une contribution significative à la formation de cristaux dans les NSPM et que ce mode est sujet à l'effet de solution des sulfates. L'effet IGIS pourrait ainsi expliquer la persistance des nuages en phase mixte, surprenante compte tenu de l'effet Bergeron-Findeisen, en réfreinant leur glaciation. Nous souhaitions donc améliorer la caractérisation de ces nuages dans notre algorithme, en prévision entre autres d'études futures de cas spécifiques. Les produits de CloudSat ont été écartés de cette étude, à cause

de leur trop faible résolution verticale (relativement à l'épaisseur de la couche liquide au sommet des NSPM) et de l'absence de données dans le premier kilomètre au-dessus de la surface. La Figure C-5 présente les fréquences d'occurrence des NSPM pour chacun des mois d'hiver investigués à cet égard.

Remarques finales

L'originalité du travail réside à la fois dans l'ensemble de la thèse (objectif, méthodologie, résultats et conclusions reliés à l'effet IGIS) et dans les résultats intermédiaires obtenus dans chacun des trois articles. En effet, l'objectif de dépister une signature de l'effet IGIS à l'échelle de l'Arctique pouvait difficilement être poursuivi avant l'avènement des instruments actifs de CloudSat et CALIPSO. La méthodologie, qui inclut une nouvelle classification des nuages arctiques, un nouveau proxy de la concentration en sulfates, une nouvelle procédure de validation associée au proxy, ainsi que des calculs forcément inédits de corrélation entre ce proxy et certaines propriétés des nuages, n'est à ma connaissance le reflet d'aucune autre méthodologie concernant l'étude des interactions nuages-aérosols. Conséquemment, les résultats et conclusions reliés à l'exploration de l'effet IGIS ne peuvent qu'être uniques. Au niveau des résultats intermédiaires, les apports étant à ma connaissance originaux sont les suivants (numéro de l'article entre parenthèses):

- les fractions nuageuses par secteur pour janvier 2007 (Arctique) et juillet 2007 (Antarctique). (1)
- la distributions des différents objets atmosphériques dans les espaces β_{532} - δ et β_{532} - χ . (1)
- l'effet du changement d'inclinaison du lidar sur l'identification des nuages minces (TIC-1) et des aérosols. (2)
- le comportement de δ et χ au voisinage du sommet des NSPM. (3)
- la loi de puissance pour décrire l'extension horizontale des NSPM. (3)
- la distribution de la couche liquide au sommet des NSPM dans l'espace température - altitude. (3)
- la carte à l'échelle arctique de la fréquence d'occurrence des NSPM. (3)

La présente thèse comporte des limites, la principale étant liée au fait que l'effet IGIS se manifeste à l'intérieur des nuages, alors que les mesures effectuées par les instruments de CloudSat et CALIPSO ne permettent pas de développer un indice relié à $[SO_4]$ dans ces objets atmosphériques, puisque le contenu en eau y domine les signaux de rétro-diffusion et de réflectivité. Il nous a donc fallu travailler en supposant, dans l'interprétation de certains résultats, que les concentrations au-dessus du nuage étaient corrélées à celles à l'intérieur, ou en supposant que $[SO_4]$ estimée en moyenne en ciel clair était représentatif de ce que l'on retrouverait en moyenne dans les nuages du même secteur. Ceci constitue une limitation méthodologique, et m'a empêché de rendre des conclusions définitives à propos de cet effet (les conclusions sont conditionnelles). Des mesures prises directement dans les nuages seront nécessaires pour éventuellement détecter une signature de l'effet IGIS. Par ailleurs, l'exercice de validation du proxy de $[SO_4]$ devrait éventuellement reposer sur une base de données élargie. En particulier, la station à Eureka (Nunavut) devrait être mise à contribution. Enfin, la détection des nuages et des événements de brume arctique, basée sur une méthode dite « de seuils », pourrait être améliorée en utilisant une méthode de reconnaissance de structures. Une telle méthode comporterait aussi ses difficultés et ses limites. Les autres limites de l'algorithme sont abondamment détaillées dans le premier article.

Malgré les limites méthodologiques de notre recherche, il est possible et important de se prononcer sur l'importance de l'effet IGIS dans le fonctionnement de l'atmosphère arctique. Pour répondre à cette question, j'invite le lecteur à considérer le premier article de cette thèse comme une exploration ayant conduit à des conclusions plus raffinées et mieux supportées dans la section 2.5.2. Mes conclusions conditionnelles sont:

- l'absence d'une signature perceptible de l'effet IGIS à l'échelle locale (~ 1000 km), c'est-à-dire que les régions où le proxy de $[SO_4]$ (α) exhibe des valeurs relativement hautes ne présente pas nécessairement de hautes valeurs de la fraction de TIC-2B (F_{2B}). Ceci vaut en particulier pour Norilsk.
- la cohérence d'un effet IGIS fort à l'échelle de l'Arctique avec les résultats montrant que les hautes valeurs de F_{2B} se retrouvent en aval des hautes valeurs de α, en termes de la circulation prévalente dans la basse troposphère.

Ces deux conclusions supposent, entre autres, que les variables autres que α qui influencent F_{2B}, telles le taux de production de sursaturation ainsi que la disponibilité des NG, sont constantes sur le domaine d'étude (de fortes valeurs de chacune de ces deux variables devraient favoriser les TIC-1/2A aux dépends des TIC-2B, donc une diminution de F_{2B}). En effet, il est possible que les disparités spatiales de ces variables masquent un effet IGIS local fort dans certaines zones, ou produisent l'artéfact d'un effet IGIS pan-arctique fort. Des simulations numériques seront nécessaires pour déterminer si cela est le cas ou non. Poursuivant avec mes conclusions:

- les tests de corrélation entre $\overline{r_{ie}}$ au sommet des TIC-2B et $\overline{\alpha_{2/1}}$ juste au-dessus n'apportent pas d'évidence d'un effet IGIS fort.
- le sel de mer occasionne potentiellement un effet similaire à l'effet IGIS au-dessus de l'Atlantique Nord.
- si l'effet IGIS affecte les NSPM, la région la plus affectée pourrait être la Mer de Kara, puisqu'autant α que la fréquence d'occurrence des NSPM y sont élevées.
- en Amérique du Nord, la région de Barrow (Alaska) semble plus propice que la région d'Eureka (Nunavut) pour effectuer des campagnes de mesures aériennes reliées à l'effet IGIS, puisqu'autant F_{2B} que la fréquence d'occurrence des NSPM sont plus élevées dans le premier cas, alors que les valeurs de α sont comparables.

Des expériences en laboratoire devraient être conduites pour déterminer si les modes de nucléation autres que le mode de déposition sont affectés par les sulfates. Enfin, je mentionne quant à l'importance de l'effet IGIS la découverte de Chylek et al. (2006) selon laquelle le rayon effectif des cristaux de glace dans les cirrus croît durant les épisodes de pollution au-dessus de l'Océan Indien. Des changements dans les conditions météorologiques entre la saison polluée et la saison plus propre sont évoquées pour expliquer leur observation, ainsi qu'un « effet indirect inverse » des aérosols, qui pourrait correspondre à ce que nous nommons l'effet IGIS.

Nous pouvons ensuite nous demander si le mécanisme RDES est un processus dominant durant l'hiver arctique. Le mécanisme RDES a le mérite d'unifier en un cadre

conceptuel relativement simple de multiples observations et considérations théoriques touchant plusieurs échelles temporelles et spatiales. Un désavantage évident avec une théorie d'une telle ampleur est la difficulté à la valider ou à l'infirmer, comme dans le cas de la célèbre hypothèse CLAW. L'état actuel des connaissances commande, si l'on veut croire que le mécanisme RDES est dominant, que plus de poids soit apporté à la preuve de l'importance de chacun des liens qui le définissent. En particulier, en tant que déclencheur du mécanisme, l'effet IGIS doit être mieux supporté. De plus, la description du mécanisme RDES exclut tout potentiel mécanisme de rétroaction négative du système plus large dans lequel il s'inscrit, si bien qu'une certaine évidence de chacun des liens ne signifierait pas nécessairement que le mécanisme dans son ensemble marque réellement et significativement le climat arctique. Par exemple, une intensification de la circulation (des tempêtes) due à l'accroissement du gradient de température entre le Haut Arctique et les latitudes moyennes pourrait occasionner un accroissement du phénomène de re-suspension de la neige, qui peut dans certaines conditions mener à l'augmentation de l'HR dans les bas niveaux de la troposphère (Lesins et al., 2009). Cette rétroaction négative pourrait être importante dans l'Archipel Canadien (terrains montagneux), mais insignifiante au-dessus de l'Océan Arctique (surface relativement plane). Il peut exister des conditions dans lesquelles le mécanisme RDES s'applique, et d'autres dans lesquelles il ne s'applique pas. Par exemple, lorsque les cristaux de glace précipitant sous les NSPM se subliment avant de toucher le sol (Shupe et al., 2008b), fournissant ainsi une nouvelle source d'humidité et de NG, le maillon « sédimentation » de la RDES est brisé. Enfin, il est en mon sens peu probable que le mécanisme RDES explique la tendance au refroidissement de surface observé durant l'hiver arctique pour la période 1982-1999 par Wang et Key (2005). En effet, l'ampleur de l'anomalie de refroidissement résultant de la RDES devrait à première approximation augmenter avec les concentrations en sulfates dans la troposphère arctique. Or, après être demeurées stables durant les années 1980, les concentrations en sulfates ont significativement décru entre 1990 et 2003 (Sirois et Barrie, 1999; Quinn et al., 2007). Toutes autres variables demeurant égales, la décroissance dans le temps d'une anomalie de refroidissement va de pair avec une tendance au réchauffement.

L'algorithme développé dans le cadre de cette thèse pourrait être amélioré et avoir d'autres utilités. Parmi les travaux envisageables, il y a:

- l'extension de la détection des nuages et des aérosols à l'échelle globale (les performances de l'algorithme sont passablement réduites en situation diurne, dû à la contamination du signal de rétro-diffusion du lidar par le rayonnement solaire).
- des études de cas précis de développement de TIC-2B.
- le test de sensibilité à l'intégration d'une procédure d'inversion pour la rétro-diffusion intrinsèque à partir de la rétro-diffusion atténuée (déjà implantée dans l'algorithme).
- l'ajout d'autres mesures provenant des satellites du A-Train (déjà fait pour AIRS).
- l'utilisation de CO (produit de l'instrument MLS, sur le satellite Aura) comme proxy de la pollution urbaine dans les nuages, comme le suggèrent Jiang et al. (2009) pour d'autres régions.
- la comparaison de la performance de détection des événements de brume arctique de AWAC4 à celle des algorithmes « officiels » de CALIPSO.

Toutes ces recherches pourraient mener à une réduction de l'incertitude qui demeure quant à l'importance de l'effet IGIS et du mécanisme RDES pour le climat hivernal arctique.

Figures

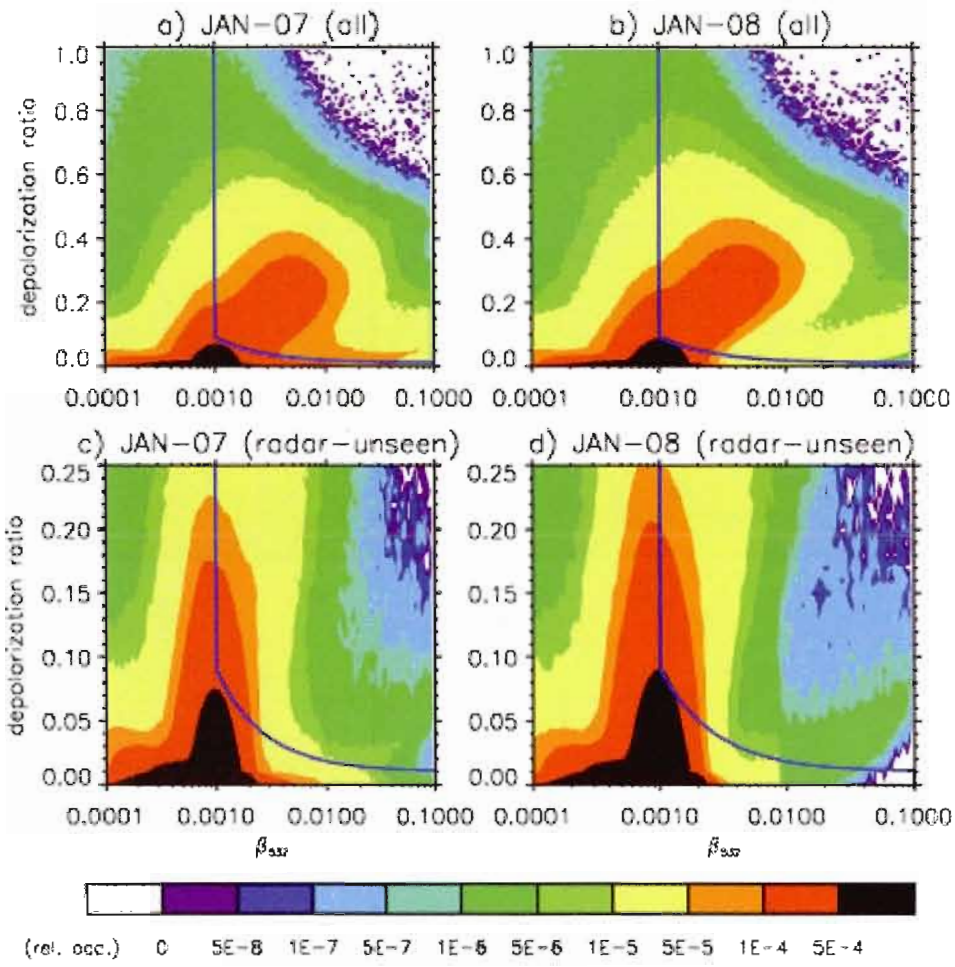

Figure C-1: Fonction de séparation entre TEC-1 et aérosols.

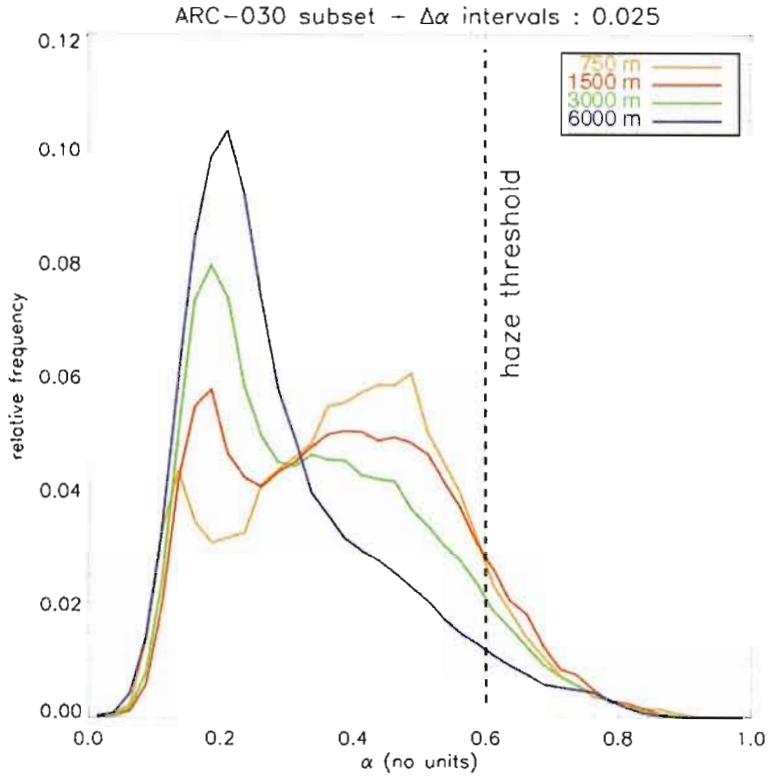

Figure C-2: Distributions de l'indice d'aérosols (intervalles de 0.025) à différentes hauteurs pour le sous-ensemble de scènes ARC-030, avec le seuil pour la brume arctique (article 1).

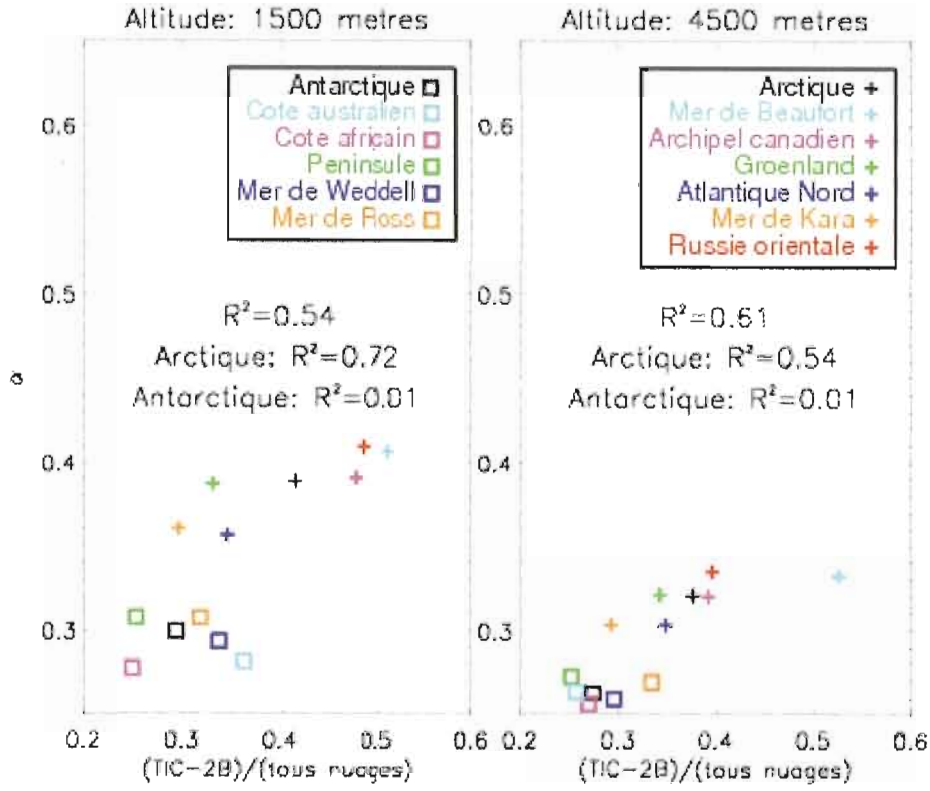

Figure C-3: Corrélations entre l'indice d'aérosols et la proportion de TIC-2B à 1500 mètres (droite) et à 4500 mètres (gauche) d'altitude (article 1).

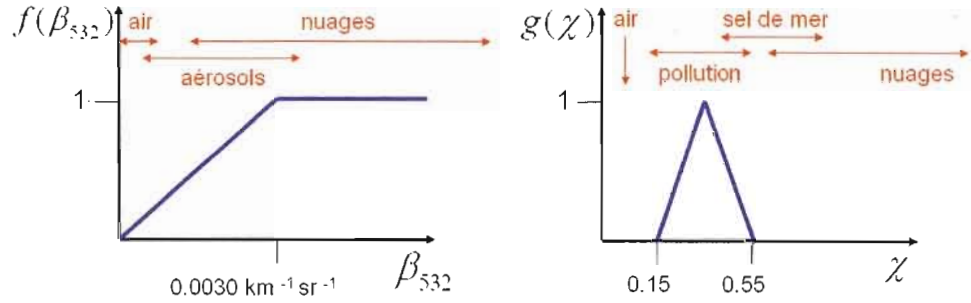

Figure C-4: Termes du proxy de la concentration en sulfates (dans l'équation 2.3).

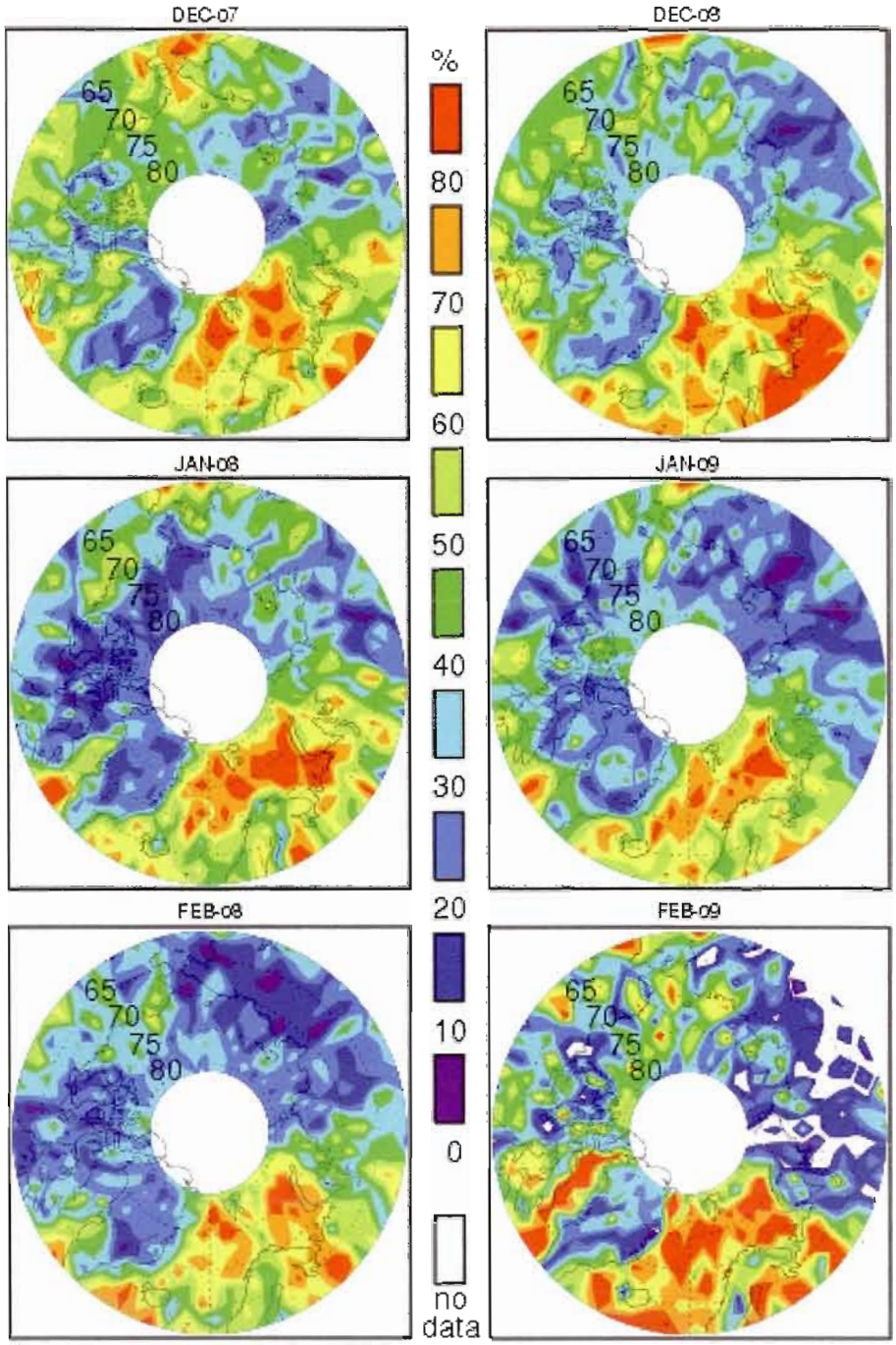

Figure C-5: Cartes de la fréquence mensuelle d'occurrence des nuages stratiformes en phase mixte dans l'Arctique.

BIBLIOGRAPHIE

Aas, W., S. Solberg, S. Manø, and K.E. Yttri. 2008. «Monitoring of long-range transported air pollutants, 2007». In Norwegian. Kjeller. Norwegian Institute for Air Research, OR 29/2008 (SFT rapport nr 1033/2008).

Albrecht, B. 1989. «Aerosols, cloud microphysics, and fractional cloudiness». *Science*, vol. 245, p. 1227-1230.

AMAP – Arctic Monitoring and Assessment Programme. 1998. *AMAP Assessment Report: Arctic Pollution Issues*. Oslo, Norway, 859 p.

Andreae, M.O., D.A. Hegg, and U. Baltensperger. 2008. «Sources and Nature of Atmospheric Aerosols». In *Aerosol Pollution Impact on Precipitation. A Scientific Review*, p. 45-90, Zev Levin and William R. Cotton Editors.

Ansmann, A., and D. Müller. 2005. «Lidar and Atmospheric Aerosol Particles». In *Lidar: Range-Resolved Optical Remote Sensing of the Atmosphere*, p. 105-141, Claus Weitkamp Editor.

Archuleta, C.M., P.J. DeMott and S.M. Kreidenweis. 2005. «Ice nucleation by surrogates for atmospheric mineral dust and mineral dust/sulfate particles at cirrus temperatures». *Atmos. Chem. Phys.*, vol. 5, p. 2617-2634.

Austin, R.T. and G.L. Stephens. 2001. «Retrieval of stratus cloud microphysical parameters using millimeter-wave radar and visible optical depth in preparation for CloudSat. 1.Algorithm formulation». *J. Geophys. Res.*, vol. 106, no. D22, p. 28,233-28,242.

Austin, R.T., A.J. Heymsfield and G.L. Stephens. 2009. «Retrieval of ice cloud microphysical parameters using the CloudSat millimeter-wave radar and temperature». *J. Geophys. Res.*, vol. 114, D00A23, doi:10.1029/2008JD010049.

Benkovitz, C.M., M.T. Scholtz, J. Pacyna, L. Tarrason, J. Dignon, E.C. Voldner, P.A. Spiro, J.A. Logan and T.E. Graedel. 1996. «Global gridded inventories of anthropogenic emissions of sulfur and nitrogen». *J. Geoph. Res.*, vol. 101, no. D22, p. 29,239-29,253.

Berresheim, H., P.H. Wine and D.D. Davis. 1995. «Sulfur in the atmosphere». In *Composition, chemistry and climate of the atmosphere*, p. 251-307, H.B. Singh. Van Nostrand Reinhold Editor.

Bertram, A.K., D.D. Patterson and J.J. Sloan. 1996. «Mechanisms and Temperatures for the Freezing of Sulfuric Acid Aerosols Measured by FTIR Extinction Spectroscopy». *J. Phys. Chem.*, vol. 100, no. 6, p. 2376-2383.

Bigg, E.K. 1980. «Comparison of Aerosol at Four Baseline Atmospheric Monitoring Stations». *J. Appl. Meteor.*, vol. 19, p. 521-533.

Blanchet, J.-P. and R. List. 1983. «Estimation of Optical Properties of Arctic Haze Using a Numerical Model». *Atmosphere-Ocean*, vol. 21, no.4, p. 444-465.

Blanchet, J.-P. and E. Girard. 1994. «Arctic greenhouse effect». *Nature*, vol. 371, p. 383.

Blanchet, J.-P. 1995. «Mechanisms of Direct and Indirect Climate Forcing by Aerosols in the Arctic Region». In *Aerosol Forcing of Climate*, p. 109-121, R.J. Charlson and J. Heintzenberg Editors.

Borys, R.D. 1989. «Studies of ice nucleation by Arctic aerosols on AGASP-II». *J. Atmos. Chem.*, vol. 9, p. 169-185.

Bourdages, L., T.J. Duck, G. Lesins, J.R. Drummond and E.W. Eloranta. 2009. «Physical properties of High Arctic tropospheric particles during winter». *Atmos. Chem. Phys. Discuss.*, vol. 9, p. 7781-7823.

Broeckner, W.S. and T.-H. Peng. 1982. *Tracers in the Sea*, p.26-27. Lamont-Doherty Geological Observatory, Columbia University: Eldigio Press.

Carlson, T.N. 1981. «Speculations on the movement of polluted air to the Arctic». *Atmospheric Environment*, vol. 15, p. 1473-1477.

Cho, H.-R., J.V. Iribarne and W.G. Richards 1981. «On the Orientation of Ice Crystals in a Cumulonimbus Cloud». *J. Atmos. Sc. - Notes and Correspondence*, vol. 38, p. 1111-1114.

Christensen, J.H. 1997. «The Danish Eulerian hemispheric model – a three-dimensional air pollution model used for the Arctic». *Atmospheric Environment*, vol. 31, no. 24, p. 4169-4191.

Chylek, P. and C. Borel. 2004. «Mixed phase cloud water/ice structure from high spatial resolution satellite data». *Geophys. Res. Lett.*, vol. 31, L14104, doi:10.1029/2004GL020428.

Chylek, P., M.K. Dubey, U. Lohmann, V. Ramanathan, Y.J. Kaufman, G. Lesins, J. Hudson, G. Altmann and S. Olsen. 2006. «Aerosol indirect effect over the Indian Ocean». *Geophys. Res. Lett.*, vol. 33, L06806, doi: 10.1029/2005GL025397.

Clarke, A. 1989. «In-situ measurements of the aerosol size distributions, physicochemistry and light absorption properties of Arctic haze». *J. Atmos. Chem.*, vol. 9, p.255-266.

Curry, J.A., W.B. Rossow, D. Randall and J.L. Schramm. 1996. «Overview of Arctic Cloud and radiation Characteristics». *Journal of Climate*. vol. 9, p. 1731-1764.

Dastoor, A.P. and J. Pudykiewicz. 1996. «A numerical global meteorological sulfur transport model and its application to Arctic air pollution». *Atmospheric Environment*, vol. 30, no. 9, p. 1501-1522.

de Boer, G., G.J. Tripoli and E.W. Eloranta. 2008. «Preliminary comparison of CloudSat-derived microphysical quantities with ground-based measurements for mixed-phase cloud research in the Arctic». *J. Geophys. Res.*, vol. 113, D00A06, doi:10.1029/2008JD010029.

de Boer, G., E.W. Eloranta and M.D. Shupe. 2009. «Arctic Mixed-Phase Stratiform Cloud Properties from Multiple Years of Surface-Based Measurements at Two High-Latitude Locations». *J. Atmos. Sc.*, doi:10.1175/2009JAS3029.1.

de Boer, G., T. Hashino and G.J. Tripoli. 2009. «Ice nucleation through immersion freezing in mixed-phase stratiform clouds: Theory and numerical simulations». *Atmos. Res.*, doi:10.1016/j.atmosres.2009.09.012. In press.

DeMott, P.J., Y. Chen, S.M. Kreidenweis, D.C. Rogers and D.E. Sherman. 1999. «Ice formation by black carbon particles». *J. Geophys. Res.*, vol. 26, no. 16, p. 2429-2432.

Durant, A.J. and R.A. Shaw. 2005. «Evaporation freezing by contact nucleation inside-out». *Geophys. Res. Lett.*, vol. 32, L20814, doi:10.1029/2005GL024175.

Eastwood, M.L., S. Cremel, M. Wheeler, B.J. Murray, E. Girard and A.K. Bertram. 2009. «Effects of sulfuric acid and ammonium sulfate coatings on the ice nucleation properties of kaolinite particles». *Geophys. Res. Lett.*, vol. 36, L02811, doi:10.1029/2008GL035997.

Eckhardt, S., A. Stohl, S. Beirle, N. Spichtinger, P. James, C. Forster, C. Junker, T. Wagner, U. Platt and S.G. Jennings. 2003. «The North Atlantic Oscillation controls air pollution transport to the Arctic». *Atmos. Chem. Phys. Discuss.*, vol. 3, p. 3222-3240.

EMEP - European Monitoring and Evaluation Programme. 1996. *Manual for sampling and chemical analysis*. Kjeller (EMEP/CCC-report 1/95) Revised 2001.

Fan, J., M. Ovtchinnikov, J.M. Comstock, S.A. McFarlane and A. Khain. 2009. «Ice formation in Arctic mixed-phase clouds: Insights from a 3-D cloud-resolving model with size-resolved aerosol and cloud microphysics». *J. Geophys. Res.*, vol. 114, D04205, doi:10.1029/2008JD010782.

Garrett, T.J. and C. Zhao. 2006. «Increased Arctic cloud longwave emissivity associated with pollution from mid-latitudes». *Nature*, vol. 440, p. 787-789

Garrett, T.J. and L.L. Verzella. 2008. «LOOKING BACK: An Evolving History of Arctic Aerosols». *Bull. Amer. Meteor. Soc.*, vol. 89, p. 299–302.

Gayet J.-F., G. Mioche, A. Dörnbrack, A. Ehrlich, A. Lampert and M. Wendisch. 2009. «Microphysical and optical properties of Arctic mixed-phase clouds. The 9 April 2007 case study». *Atmos. Chem. Phys.*, vol. 9, p. 6581-6595.

Girard E., J.-P. Blanchet and Y. Dubois. 2005. «Effects of arctic sulphuric acid aerosols on wintertime low-level atmospheric ice crystals, humidity and temperature at Alert, Nunavut». *Atmospheric Research*, vol. 73, p. 131-148.

Girard, E. and A. Stefanof. 2007. «Assessment of the dehydration-greenhouse feedback over the Arctic during February 1990». *Int. J. Climatol.*, vol. 27, p. 1047-1058.

Gong, S.L., L.A. Barrie, J.-P. Blanchet, K. von Salzen, U. Lohmann, G. Lesins, L. Spacek, L.M. Zhang, E. Girard, H. Lin, R. Leaitch, H. Leighton, P. Chylek and P. Huang. 2003. «Canadian Aerosol Module: A size-segregated simulation of atmospheric aerosol processes for climate and air quality models 1. Module development», *J. Geophys. Res.*, vol. 108, no. D1, doi:10.1029/2001JD002002.

Gong, S. L. and L.A. Barrie. 2003. «Simulating the impact of sea salt on global nss sulphate aerosols». *J. Geophys. Res.*, vol. 108, no. D16, doi:10.1029/2002JD003181.

Grenier, P., J.-P. Blanchet and R. Muñoz-Alpizar. 2009. «Study of Polar Thin Ice Clouds and Aerosols Seen By CLOUDSAT and CALIPSO During Mid-Winter 2007». *J. Geophys. Res.*, vol. 114, D09201, doi:10.1029/2008JD010927.

Hahn, C.J., S.G. Warren and J. London. 1995. «The effect of Moonlight on Observation of Cloud Cover at Night, and Application to Cloud Climatology». *J. of Climate*, vol. 8, p. 1429-1446.

Haladay, T., and G. Stephens. 2009. «Characteristics of tropical thin cirrus clouds deduced from joint CloudSat and CALIPSO observations». *J. Geophys. Res.*, vol. 114, D00A25, doi:10.1029/2008JD010675.

Hara, K., S. Yamagata, T. Yamanouchi, K. Sato, A. Herber, Y. Iwasaka, M. Nagatani and H. Nakata. 2003. «Mixing states of individual aerosol particles in spring Arctic troposphere during ASTAR 2000 campaign». *J. Geophys. Res.*, vol. 108, no D7, doi:10.1029/2002JD002513.

Harrington, J.Y. and P.Q. Olsson. 2001. «A method for the parameterization of cloud optical properties in bulk and bin microphysical models. Implications for arctic cloudy boundary layers». *Atmos. Res.*, vol. 57, p. 51-80.

Hobbs, P.V. and A.L. Rangno. 1990. «Rapid Development of High Ice Particle Concentrations in Small Polar Maritime Cumuliform Clouds». *J. Atmos. Sc.*, vol. 47, no. 22, p. 2710-2722.

Hoff, R.M., W.R. Leaitch, P. Fellin and L.A. Barrie. 1983. «Mass Size Distributions of the Winter Arctic Aerosol». *J. Geophys. Res.*, vol. 88, no. C15. p. 10,947-10,956.

Hogan, R.J., P.N. Francis, H. Flentje, A.J. Illingworth, M. Quante and J. Pelon. 2003. «Characteristics of mixed-phase clouds. I: Lidar, radar and aircraft observations from CLARE '98». *Quart. J. Roy. Meteor. Soc.*, vol. 129, p. 2089-2116.

Hostetler, C.A., Z. Liu, J. Reagan, M. Vaughan, D. Winker, M. Osborn, W.H. Hunt, K.A. Powell and C. Trepte. 2006. «CALIOP Algorithm Theoretical Basis Document: Calibration and Level 1 Data Products». Available at: www-calipso.larc.nasa.gov/resources/project_documentation.php

Howard L. 1865. *Essay on the Modification of Clouds*. 37 p., London: John Churchill and Sons, Editor. Third Edition (first published 1803).

Hu, Y., Z. Liu, D. Winker, M. Vaughan and V. Noel. 2006. «Simple relation between lidar multiple scattering and depolarization for water clouds». *Opt. Lett.*, vol. 31, p. 1809-1811.

Hu, Y. 2007. «Depolarization ratio-effective lidar ratio relation: Theoretical basis for space lidar cloud phase discrimination». *Geophys. Res. Lett.*, vol. 34, L11812, doi:10.1029/2007GL029584.

Hunt, W.H., D.M. Winker, M.A. Vaughan, K.A. Powell, P.L. Lucker and C. Weimer. 2009. «CALIPSO Lidar Description and Performance Assessment». *J. of Atmos. And Oceanic Tech.*, vol. 26, p. 1214-1228, doi: 10.1175/2009JTECHA1223.1.

Intrieri, J.M., M.D. Shupe, T. Uttal and B.J. McCarty. 2002. «An annual cycle of Arctic cloud characteristics observed by radar and lidar at SHEBA», *J. Geophys. Res.*, vol. 107, no. C10, doi:10.1029/2000JC000423.

IPCC - Intergovernmental Panel of Climate Change. 2001. *Climate Change 2001. The Scientific Basis.* Cambridge Univ. Press, 944 p.

IPCC - Intergovernmental Panel of Climate Change. 2007. *Climate Change 2007. The Physical Science Basis.* Cambridge Univ. Press, 996 p.

Ishii, S., T. Shibata, T. Nagai, K. Mizutani, T. Itabe, M. Hirota, T. Fujimoto and O. Uchino. 1999. «Arctic haze and clouds observed by lidar during four winter seasons of 1993-1997, at Eureka, Canada». *Atm. Environment*, vol. 33, p. 2459-2470.

Jaffe, D.A. 1991. «Local Sources of Pollution in the Arctic: From Prudhoe Bay to the Taz Peninsula». In *Pollution of the Arctic atmosphere*, p. 255-288, W.T. Sturges Editor.

Jiang, J.H., H. Su, S.T. Massie, P.R. Colarco, M.R. Schoeberl and S. Platnick. 2009. «Aerosol-CO relationship and aerosol effect on ice cloud particle size: Analyses from Aura Microwave Limb Sounder and Aqua Moderate Resolution Imaging Spectrometer observations». *J. Geophys. Res.*, vol. 114, D20207, doi:10.1029/2009JD012421.

Kahn, B.H., M.T. Chahine, G.L. Stephens, G.G. Mace, R.T. Marchand, Z. Wang, C.D. Barnet, A. Eldering, R.E. Holz, R.E. Kuehn and D.G. Vane. 2007. «Cloud type comparisons of AIRS, CloudSat, and CALIPSO cloud height and amount». *Atmos. Chem. Phys. Discuss.*, vol. 7, p. 13,915-13,958.

Kalnay, E. and coauthors. 1996. «The NCEP/NCAR Reanalysis 40-year Project». *Bull. Amer. Meteor. Soc.*, vol. 77, p. 437-471.

Khvorostyanov, V.I. and J.A. Curry. 2004. «The Theory of Ice Nucleation by Heterogeneous Freezing of Deliquescent Mixed CCN. Part I: Critical Radius, Energy, and Nucleation Rate». *J. Atmos. Sc.*, vol. 61, p. 2676-2691.

Knopf, D.A. and T. Koop. 2006. «Heterogeneous nucleation of ice on surrogates of mineral dust». *J. Geophys. Res.*, vol. 111, D12201, doi:10.1029/2005JD006894.

Law, K.S. and A. Stohl. 2007. «Arctic Air Pollution: Origins and Impacts». *Science*, vol. 315, p.1537-1540.

Lesins, G., L. Bourdages, T.J. Duck, J.R. Drummond, E.W. Eloranta and V.P. Walden. 2009. «Large surface radiative forcing from topographic blowing snow residuals measured in the High Arctic at Eureka». *Atmos. Chem. Phys.*, vol. 9, p. 1847-1862.

Liu, Z., M. Vaughan, L. Poole, C. Hostetler and D. Winker. 2002. «Scene Classification for the CALIPSO Lidar». *Conference paper for ILRC 2002*, Quebec City, Quebec.

Liu, Z., W. Hunt, M. Vaughan, C. Hostetler, K.P. McGill, D. Winker and Y. Hu. 2006. «Estimating random errors due to shot noise in backscatter lidar observations». *Appl. Opt.*, vol. 45, no. 18, p. 4437-4447.

Liu, Y., J.R. Key and X. Wang. 2008. «The Influence of Changes in Cloud Cover on Recent Surface Temperature Trends in the Arctic». *J. of Climate*, vol. 21, p. 705-715.

Lohmann, U. and E. Roeckner. 1996. «Design and performance of a new cloud microphysics scheme developed for the ECHAM general circulation model». *Clim. Dyn.*, vol. 12, p. 557-572.

Lowenthal, D.H., R.D. Borys, T.W. Choularton, K.N. Bower, M.J. Flynn and M.W. Gallagher. 2004. «Parameterization of the cloud droplet-sulfate relationship». *Atmospheric Environment*, vol. 38, p. 287-292.

Lubin, D. and A.M. Vogelmann. 2006. «A climatologically significant aerosol longwave indirect effect in the Arctic». *Nature*, vol. 439, p. 453-456.

Mace, G. 2007. *Level 2 GEOPROF Product Process Description and Interface Control Document Algorithm version 5.3*. Available at: www.cloudsat.cira.colostate.edu/dataICDlist.php?go=list&path=/2B-GEOPROF

Marcolli, C., S. Gedamke, T. Peter and B. Zobrist. 2007. «Efficiency of immersion mode ice nucleation on surrogates of mineral dust». *Atmos. Chem. Phys.*, vol. 7, p. 5081-5091.

McFarquhar, G.M., G. Zhang, M.R. Poellot, G.L. Kok, R. McCoy, T. Tooman, A. Fridlind and A.J. Heymsfield. 2007. «Ice properties of single-layer stratocumulus during the Mixed-Phase Arctic Cloud Experiment: 1. Observations». *J. Geophys. Res.*, vol. 112, D24201, doi:10.1029/2007JD008633.

Meyers, M.P., P.J. DeMott and W.R. Cotton. 1992. «New Primary Ice-Nucleation Parameterizations in an Explicit Cloud Model». *J. Appl. Met.*, vol. 31, p. 708-721.

Mitchell, J.M. Jr. 1957. «Visual range in the polar regions with particular reference to the Alaskan Arctic». *J. Atmos. Terr. Phys.*, Special Suppl., p. 195-211.

Muñoz-Alpizar, R., P. Grenier, J.-P. Blanchet, E. Girard and H.J. Jiang. «The Role of Arctic Cold Lows in Generating Thin Ice Clouds: A Comparison between CloudSat-CALIPSO and NARCM Simulations». In preparation for *J. Geophys. Res*.

Omar, A.H. and T. Babakaeva. 2004. «Aerosol Optical Properties Derived from Lidar Observations Using Cluster Analysis». *IEEE Xplore*, vol. 3, p. 2212-2215.

Onasch, T.B., R.L. Siefert, S.D. Brooks, A.J. Prenni, B. Murray, M.A. Wilson and M.A. Tolbert. 1999. «Infrared spectroscopic study of the deliquescence and efflorescence of ammonium sulfate aerosol as a function of temperature». *J. Geophys. Res.*, vol. 104, no D17, p. 21,317-21,326.

Peixoto J.P. and A.H. Oort. 1996. «The Climatology of Relative Humidity in the Atmosphere». *J. of Climate*, vol. 9, p.3443-3463.

Pinto, J.O. 1998. «Autumnal Mixed-Phase Cloudy Boundary Layers in the Arctic». *J. Atmos. Sc.*, vol. 55, p. 2016-2038.

Prenni, A.J., J.Y. Harrington, M. Tjernström, P.J. DeMott, A. Avramov, C.N. Long, S.M. Kreidenweis, P.Q. Olsson and J. Verlinde. 2007. «Can ice-nucleating aerosols affect Arctic seasonal climate ?». *Bull. Amer. Met. Soc.*, p. 541-550.

Pruppacher, H.R. and J.D. Klett. 1997. *Microphysics of Clouds and Precipitation (Second Edition)*. Kluwer Academics Publishers, 954 p.

Quinn, P.K., G. Shaw, E. Andrews, E.G. Dutton, T. Ruoho-Airola and S.L. Gong. 2007. «Arctic Haze: current trends and knowledge gaps». *Tellus*, vol. 59B, p. 99-114.

Raatz, W.E. 1991. «The Climatology and Meteorology of Arctic Air Pollution». In *Pollution of the Arctic atmosphere*, p. 13-42, W.T. Sturges Editor.

Rahn, K.A. 1981. «Relative importances of North America and Eurasia as sources of Arctic aerosol». *Atmospheric Environment*, vol. 15, no 8, p.1447-1455.

Sasano, Y. and E.V. Browell. 1989. «Light scattering characteristics of various aerosol types derived from multiple wavelength lidar observations». *Applied Optics*, vol. 28, no. 9, p.1670-1679.

Sassen, K. 1991. «The Polarization Lidar Technique for Cloud Research: A Review and Current Assessment». *Bull. Amer. Met. Soc.*, vol. 72, no. 12, p. 1848-1866.

Schutgens, N. and D.P. Donovan. 2004. «Retrieval of atmospheric reflectivity profiles in case of long radar pulses». *Atm. Res.*, vol. 72, p. 187-196.

Seinfeld, J.H. and S.N. Pandis. 1998. *Atmospheric Chemistry and Physics: From Air Pollution to Climate Change*. John Wiley and Sons Editor, 1326 p.

Serreze, M.C., J.D. Kahl and R.C. Schnell. 1992. «Low-Level Temperature Inversions of the Eurasian Arctic and comparisons with Soviet Drifting Station Data». *J. of Climate*, vol. 5, p. 615-629.

Serreze, M.C. and R.G. Barry. 2005. *The Arctic Climate System*. Coll. «Cambridge Atmospheric and Space Science Series», Cambridge University Press, 385 p.

Sharma, S., D. Lavoué, H. Cachier, L.A. Barrie and S.L. Gong. 2004. «Long-term trend of the black carbon concentrations in the Canadian Arctic». *J. Geophys. Res.*, vol. 109, D15203, doi:10.1029/2003JD004331.

Shaw, G.E. 1988. «Antarctic aerosols: a review». *Rev. Geophys.*, vol. 26, no. 1, p. 89-112.

Shaw, G.E., K. Stamnes and Y.X. Hu. 1993. «Arctic Haze: Perturbation to the Radiation Field». *Meteorol. Atmos. Phys.*, vol. 51, p. 227-235.

Sirois, A. and L.A. Barrie. 1999. «Arctic lower tropospheric aerosol trends and composition at Alert, Canada: 1980-1995». *J. Geoph. Res.*, vol. 104, no. D9, p. 11,599-11,618.

Shupe, M.D., S.Y. Matrosov and T. Uttal. 2006. «Arctic Mixed-Phase Cloud Properties Derived from Surface-Based Sensors at SHEBA». *J. Atmos. Sc.*, vol. 63, p. 697-711.

Shupe, M.D., J.S. Daniel, G. de Boer, E.W. Eloranta, P. Kollias, C.N. Long, E.P. Luke, D.D. Turner and J. Verlinde. 2008a. «A Focus on Mixed-Phase Clouds». *Bull. Amer. Met. Soc.*, doi:10.1175/2008BAMS2378.1.

Shupe, M.D., P. Kollias, P.O.G. Persson and G.M. McFarquhar. 2008b. «Vertical Motions in Arctic Mixed-Phase Stratiform Clouds«. *J. Atmos. Sc.*, vol. 65, doi:10.1175/2007JAS2479.1.

Spangenberg, D.A., P. Minnis, S. Sun-Mack, M.D. Shupe and M.R. Poellot. 2006. «Characterization of Mixed-Phase Clouds During Mixed-Phase Arctic Cloud Experiment from Satellite, Ground-Based, and In-Situ Data». *Sixteenth ARM Science Team Meeting Proceedings*, Albuquerque, NM, March 27-31.

Stephens, G.L., D.G. Vane, R.J. Boain, G.G. Mace, K. Sassen, Z. Wang, A.J. Illingworth, E.J. O'Connor, W.B. Rossow, S.L. Durden, S.D. Miller, R.T Austin, A. Benedetti, C. Mitrescu and the CloudSat Science Team. 2002. «The CloudSat Mission and the A-Train: A New Dimension of Space-Based Observations of Clouds and Precipitation». *Bull. Amer. Met. Soc.*, p. 1771-1790.

Stern, D.I. 2005. «Global sulfur emissions from 1850 to 2000». *Chemosphere*, vol. 58, p.163-175.

Tang, I.N. and H.R. Munkelwitz. 1994. «Water activities, densities, and refractive indices of aqueous sulfates and sodium nitrate droplets of atmospheric importance». *J. Geophys. Res.*, vol. 99, no. D9, p. 18,801–18,808.

Twomey, S. 1977. «The influence of pollution on the shortwave albedo of clouds». *J. of atmos. sci.*, vol. 34, no. 7, p. 1149-1152.

Vaughan, M.A., D.M. Winker and K.A. Powell. 2005. *CALIOP Algorithm Theoretical Basis Document: Part 2: Feature Detection and Layer Properties Algorithms*. Available at: www-calipso.larc.nasa.gov/resources/pdfs/PC-SCI-202_Part2_rev1x01.pdf

Vaughan, M. 2008. *Lidar Pointing Angle Change*. NASA Langley Res. Cent., Langley, Va. Available at: http://eosweb.larc.nasa.gov/PRODOCS/calipso/pdf/TiltModeGeometry.pdf

Verlinde, J. and co-authors. 2007. «The mixed-phase Arctic cloud experiment». *Bull. Amer. Met. Soc.*, doi:10.1175/BAMS-88-2-205.

Waggoner, A.P. and R.E. Weiss. 1980. «Comparison of fine particle mass concentration and light scattering extinction in ambient aerosol». *Atmospheric Environment*, vol. 14, p. 623-626.

Walden, V.P., S.G. Warren and E. Tuttle. 2003. «Atmospheric Ice Crystals over the Antarctic Plateau in Winter». *J. Appl. Met.*, vol. 42, p. 1391-1405.

Wandinger, U. 2005. «Introduction to Lidar». In *Lidar: Range-Resolved Optical Remote Sensing of the Atmosphere*, p. 1-18, Claus Weitkamp Editor.

Wang, X. and J.R. Key. 2005. «Arctic Surface, Cloud, and Radiation Properties Based on the AVHRR Polar Pathfinder Dataset. Part II: Recent Trends». *J. of Climate*, vol. 18, p. 2575-2593.

Welti, A., F. Lüönd, O. Stetzer and U. Lohmann. 2009. «Influence of particle size on the ice nucleating ability of mineral dusts». *Atmos. Chem. Phys. Discuss.*, vol. 9, p. 6929-6955.

Winker, D.M., W.H. Hunt and M.J. McGill. 2007. «Initial performance assessment of CALIOP». *Geophys. Res. Lett.*, vol. 34, L19803, doi:10.1029/2007GL030135.

Yamanouchi, T. and 15 co-authors. 2005. «Arctic Study of Tropospheric Aerosol and Radiation (ASTAR) 2000: Arctic haze case study». *Tellus*, vol. 57B, p. 141-152.

Yu, H., M. Chin, L.A. Remer, R.G. Kleidman, N. Bellouin, H. Bian and T. Diehl. 2009. «Variability of marine aerosol fine-mode fraction and estimates of anthropogenic aerosol component over cloud-free oceans from the Moderate Resolution Imaging Spectroradiometer (MODIS)», *J. Geophys. Res.*, vol. 114, D10206, doi:10.1029/2008JD010648.

Zuberi, B., A.K. Bertram, C.A. Cassa, L.T. Molina and M.J. Molina. 2002. «Heterogeneous nucleation of ice on $(NH_4)_2SO_4$-H_2O particles with mineral dust immersions». *Geophys. Res. Lett.*, vol. 29, no. 10, doi:10.1029/2001GL014289.